University of Bath

PHD

Ionospheric Imaging and Scintillation Monitoring in the Antarctic and Arctic

Kinrade, Joe

Award date:
2014

Awarding institution:
University of Bath

Link to publication

Ionospheric Imaging and Scintillation Monitoring in the Antarctic and Arctic
Joe Kinrade
A thesis submitted for the degree of Doctor of Philosophy
University of Bath
Department of Electronic & Electrical Engineering
December 2013

Abstract

Electron density irregularities influence Global Navigation Satellite System (GNSS) signals, manifesting as ionospheric scintillation. Scintillation poses a service risk to safety-critical GNSS applications at high latitudes. It is difficult to predict, as ionospheric instability processes are not yet fully characterised. This research combines the fields of ionospheric imaging and scintillation monitoring, to investigate the causes of scintillation in the Antarctic and Arctic.

Results revealed a plasma patch structure above Antarctica, in response to the impact of a solar wind shock front. Measurements from a network of Global Positioning System scintillation receivers across the continent revealed moderate levels of phase scintillation associated with Total Electron Content (TEC) gradients at the patch break-off point. Scintillation was also driven by solar particle precipitation at E and F region altitudes, verified with in situ spectrometers on polar-orbiting satellites. The current receiver coverage in the region provided the Multi-Instrument Data Analysis Software (MIDAS) tomography tool with sufficient data to track the lifetime of the plasma patch without a convection model.

A second experiment was performed at the South Pole, using a collocated GPS scintillation receiver and auroral imager. This allowed simultaneous line-of-sight tracking of GPS signals through the optical auroral emissions. Results showed the first statistical evidence that auroral emissions can be used a proxy for ionospheric irregularities causing GPS scintillation. The relationship was strongest during the presence of discrete auroral arcs. Correlation levels of up to 74% were found over periods of 2-3 hours. The use of multiple emission wavelengths provided basic altitude discrimination.

Current capability of ionospheric TEC mapping in the Arctic was tested, where GPS receiver distribution is extensive compared to present Antarctic coverage. Analysis of the ionosphere's response to a storm event revealed a sequential picture of polar cap patch activity, without the aid of plasma convection modelling. The electron density enhancements of the auroral oval were imaged in completeness for the first time using GPS tomography. Reconstructions were verified using ultraviolet auroral imagery from polar-orbit satellites, and vertical profiles from an incoherent scatter radar.

Acknowledgements

Thank you to Mum, Dad and Sam for their love and support. I don't know what I'd do without them.

My biggest thank you is to Cathryn Mitchell. Her complete faith in ability, endless patience, and provision of freedom have made for a pretty extraordinary PhD. I am very lucky to have been one of Cathryn's students.

I have learnt a lot from Nathan Smith, Biagio Forte, Mark Greco and Gary Bust, who always find the time to help. A huge thank you to my friends and colleagues in the Invert group, past and present, for making it a pleasure to come to work.

I would like to thank the Engineering and Physical Sciences Research Council (EPSRC) and the Isle of Man Government for supporting this work. I also appreciate the incredible fieldwork trip I had to Antarctica, supported by the Natural Environment Research Council (NERC), the British Antarctic Survey (BAS), the National Science Foundation (NSF) and the United States Antarctic Program (USAP). Thanks to Allan Weatherwax at Siena College and Yusuke Ebihara at Kyoto University for their collaboration with the all-sky imager at South Pole, and to the laboratory technicians at Rothera, Halley and Amundsen-Scott stations for keeping equipment running.

This work makes use of data sets provided by the International Global Navigation Satellite System Service (IGS), the United Navstar Corporation (UNAVCO), the Advanced Composition Explorer (ACE) Science Center, the Kyoto Centre for Geomagnetism, and the SPIDR and OMNIWeb services. Poker Flat Incoherent Scatter Radar (PFISR) data were kindly provided by Michael Nicolls at SRI International. Dave Hardy of AFRL designed the DMSP particle detectors, with data obtained from JHU APL. Larry Paxton at JHU APL kindly provided SSUSI data. The M-Map plotting package, developed by Rich Pawlowicz, is used throughout this thesis. I gratefully acknowledge the use of the University of Bath's tomographic imaging software, Multi-Instrument Data Analysis Software (MIDAS).

CONTENTS

List of Figures

List of Tables

List of Abbreviations

AACGM	Altitude-Adjusted Corrected Geomagnetic coordinates
ACE	Advanced Composition Explorer
ASI	All-Sky Imager
C/A	Coarse-acquisition
CCD	Charge Coupled Device
CGLAT	Corrected Geomagnetic Latitude
CHAMP	Challenging Mini-satellite Payload
CME	Coronal Mass Ejection
CNO	Carrier-to-Noise Ratio
COSMIC	Constellation Observing System for Meteorology, Ionosphere, and Climate
CPU	Control Processing Unit
DLL	Delay-Locked Loop
DMSP	Defense Meteorological Satellite Program
DORIS	Doppler Orbitography and Radio positioning Integrated by Satellite
EISCAT	European Incoherent Scatter Scientific Association
EOF	Empirical Orthogonal Function
EUV	Extreme Ultra Violet
FOV	Field Of View
GNSS	Global Navigation Satellite System
GPS	Global Positioning System
GRACE	Gravity Recovery and Climate Experiment
IDA4D	Ionospheric Data Assimilation Four Dimensional
IMF	Interplanetary Magnetic Field
ISR	Incoherent Scatter Radar
LEO	Low Earth Orbit
MIDAS	Multi-Instrument Data Analysis Software
MLAT	Magnetic Latitude
MLT	Magnetic Local Time
OCXO	Oven-Controlled Crystal Oscillator
OI	atomic oxygen
PFISR	Poker Flat Incoherent Scatter Radar
PLL	Phase Locked Loop
POES	Polar-orbiting Operational Environmental Satellites
R_E	Earth radius (~6371 km)
RINEX	Receiver Independent Exchange Format

SAC-C	Satellite de Aplicaciones Cientifico-B
SNR	Signal-to-Noise Ratio
SPIDR	Space Physics Interactive Data Resource
SSUSI	Special Sensor Ultraviolet Spectrographic Imager
TEC	Total Electron Content
TECU	Total Electron Content Unit (10^{16} electrons m^{-2})
TOI	Tongue Of Ionization
UT	Universal Time
UV	Ultra Violet
WWII	World War II

1 Introduction

Our planet has a delicate relationship with the Sun. Violent explosions on the Sun's surface expel a supersonic stream of radiation, charged particles and magnetic flux into the solar system. Earth exists as a small entity in a much larger system, sitting in the relentless flow of the solar wind. Life on Earth is only possible under the protection of its magnetic field, deflecting solar particles around the planet that would otherwise bombard the atmosphere and surface. The shielded region, the magnetosphere, is not impenetrable. Dynamic magnetic interactions in the near-Earth space environment lead to the injection of solar particles into the atmosphere at high latitudes, delivering significant energy input via the vertical field lines that exist there. Interaction between the solar wind and Earth's magnetic field leads to magnetic flux convection over the polar regions, driving wide-area circulatory current systems. The final component and energy sink in this solar-terrestrial system is the ionosphere.

Linkage to the magnetosphere at high latitudes leads to the existence of an ionosphere that is considerably more complex than that elsewhere at mid and low latitudes. The ethereal lights of the aurora have been observed throughout human history, but are only one of a number of interesting ionospheric phenomena specific to the Arctic and Antarctic latitudes. Sporadic periods of space weather can lead to irregular and unpredictable plasma behaviour, such as high velocity flow patterns and sudden localised enhancement of electron density. The Earth's ionosphere has an intrinsic relationship with radio communication, as the free electrons in the plasma have an influence on the propagation of electromagnetic waves. This research is concerned with the effects of the high latitude ionosphere on signals from Global Navigation Satellite Systems (GNSS), which are delayed and distorted as they pass from satellite to ground through the ionosphere. The most problematic of these effects for navigation and timing applications is ionospheric scintillation, which is a propagation effect caused by irregularities and gradients in the electron density. Refractive and diffractive processes cause interference on the travelling wave front of a signal as it passes through highly structured regions of electron density. From a GNSS user perspective, severe scintillation activity can lead to interruption or degradation of service when individual satellite links are lost due to deep signal power fading and loss of receiver tracking.

Conversely, the effects of the ionosphere on GNSS signals allow their usage as a remote sensing tool. The physical processes causing scintillation at high latitudes are not fully understood, because they are difficult to predict and exist on multiple scales of space and time. There is also a historical lack of observations from high latitude sites, as the extreme environments of the Arctic and Antarctic make it a challenge to operate equipment. Over the last decade however, the coverage of ground-based GNSS receivers has improved in the polar regions. Specialised Global Positioning System (GPS) scintillation receivers have been deployed to remote sites across the Antarctic, the measurements of which are used in this research to assess the severity of scintillation activity and detect the presence of ionospheric irregularities.

A multi-instrument approach is required to investigate the ionospheric behaviour leading to scintillation activity. The second major tool used throughout this research is GNSS tomography, which has emerged as a useful technique for imaging the global and regional structuring of the ionosphere. This is important for diagnosing the ionosphere's response to geomagnetic disturbances, when dynamic and moving large-scale structures are likely to exhibit strong plasma gradients or break down to smaller scales as irregularities causing scintillation. Computed Tomography (CT) techniques were originally developed for medical scanning of the human body using X-rays. GNSS tomography ingests integral measurements of the electron density from multiple, spaced receivers on the ground, and performs a time-dependent inversion to reconstruct the three-dimensional electron density. Achieving this at high latitudes is a challenge however, because receiver coverage is typically poor, and the inherent fast-moving plasma structures are difficult to reconstruct reliably. This research builds on recent advancements in GNSS tomography at high latitudes, combining images with the study of GPS scintillation.

To place the research in a wider context, Chapter 2 presents an overview of the Sun-Earth weather system, followed by a description of the ionosphere's general formation, global morphology and high latitude features.

Chapter 3 reviews the high latitude ionosphere from a radio observation perspective. Recent work in the fields of GNSS tomographic imaging and scintillation monitoring are discussed, from both the Antarctic and Arctic regions. Efforts in wide-area imaging of the auroral oval are also considered, as it is an area associated with electron density enhancements. The chapter concludes with the main aims of the research.

Chapter 4 is dedicated to describing propagation theory and the methods of ionospheric observation used throughout this research. Scintillation measurement requires the use of specialised GNSS receivers and careful data treatment. For context the effects of severe scintillation activity on GPS performance are summarized. The basic workings of the tomographic imaging tool Multi-Instrument Data Analysis Software (MIDAS) are described, with a note on its adaption for high latitude usage. Several supporting observation techniques have also been used throughout the research for verification, including geomagnetic indices, Incoherent Scatter Radar (ISR), an auroral All-Sky Imager (ASI), and polar-orbiting satellite instruments.

Chapter 5 reports on the first experiment conducted in the research. Antarctica is a challenging place to deploy measurement equipment, and a historical lack of observations has hindered efforts to image and quantify features of the ionosphere that cause scintillation. Knowledge of these processes has developed mostly in the Arctic latitudes, but the past decade has seen an increase in the number of Antarctic ground-based GPS receivers. This imaging experiment uses this improved data coverage to profile the ionosphere's response to a geomagnetic storm, combining MIDAS tomographic images and measurements from a new network of remote scintillation monitoring stations across the continent.

Chapter 6 investigates the relationship between the visible emissions of the aurora, and GPS signal phase scintillation. GPS tomography cannot directly resolve the irregularity structures that cause scintillation, but the lights of the aurora may be a reasonable proxy for small-scale electron density structuring. A unique experiment uses collocated instrumentation at the Amundsen-Scott South Pole station to directly compare the brightness of emissions with the amount of signal phase fluctuations. A new method is detailed, which superimposes GPS scintillation measurements directly onto images from an All-Sky Imager (ASI), allowing the extraction of spatial and temporal correlation statistics.

Chapter 7 shifts focus to tomographic imaging of the Arctic ionosphere. The GPS receiver coverage is denser and more evenly distributed here than in the Antarctic, having also improved over the last decade in the fringes of North America, Canada and Greenland. The current capabilities of the MIDAS algorithm at Arctic latitudes are demonstrated, using tomographic imagery of an ionospheric storm at equinox. A hemispheric comparison is also made, analyzing simultaneous images from the Arctic and Antarctica.

Finally in Chapter 8 the results of this research are summarized and conclusions are made with respect to the original aims set out in Chapter 3. Suggested future work is also discussed.

2 The ionosphere

This Chapter describes the known morphology and processes that define the high latitude ionosphere. Firstly an overview of the Sun-Earth system establishes a wide perspective of the processes that influence the ionosphere, and the geophysical features of the Earth's magnetic field. This is followed by some essential background information on the ionosphere's general formation and vertical structure. Finally attention is focused on characteristics of the high latitude ionosphere as the main subject of this research. These include large-scale plasma convection, solar particle precipitation, and the occurrence of geomagnetic storms.

2.1 The Sun-Earth system

Solar wind interaction with the magnetosphere greatly influences the high-latitude ionosphere, and it is useful to consider this wider geophysical perspective in approach to understanding ionospheric activity. It is often a cascade of events in the Sun-Earth system that ultimately leads to a change or irregular response in the ionosphere's behaviour, for example following magnetic storms or solar flare emissions. The Earth's magnetosphere is largely shaped and distorted by the constant energy outflow of the Sun, which exists in the form of the solar wind and a strongly coupled 'frozen-in' interplanetary magnetic field (IMF). The 'frozen-in' theorem [*Alfvén*, 1942; 1943], using a combination of Maxwell's equations and magneto-hydrodynamic theory, states that the IMF is bound to the solar plasma because of its high conductivity and essentially collisionless nature [e.g. *Kamide & Chian*, 2007] (fundamentally, movement of a magnetic field line within a conductive medium is difficult because of induced current flows, whose magnetic fields oppose the initial movement). The Sun continuously 'boils off' its own mass and magnetic field in hugely energetic reactions, releasing dynamic flows of protons and electrons in a radial direction as it rotates in the ecliptic plane. Average particle density is about 5/cm^3, however this can fluctuate within regions of compression and rarefaction following coronal mass ejections (CME). Since the ends of the open field lines are embedded in the surface of the rotating Sun, the IMF subsequently forms a series of splayed spirals. The effect is similar to a rotating garden sprinkler, which forms a spiral water jet of droplets that are travelling radially outwards. At Earth's distance away, the radial velocity of the solar wind is normally between 300-

400 km/sec, but this can increase to over 700 km/sec within fast streams led by CME shock fronts [e.g. *Feldman et al.*, 2005].

The IMF has three-dimensional vector components that describe its orientation and magnitude in space. The IMF tends to lie in the solar-ecliptic plane, but importantly it also has an undulating north-south component, given the notation B_z. In general it is the polarity of the B_z and B_y components that determines whether the solar wind is deflected past or connected to the magnetosphere, through a process called magnetic reconnection [e.g. *Sandholt et al.*, 1998; 2004]. This is a breakdown of the frozen-in flux approximation, when two opposing magnetic field lines break and merge together. This is an important process in the magnetosphere, as it allows plasmas of different origin (the solar wind and the magnetosphere in this case) to interact and exchange mass, momentum and energy; magnetic energy is converted to kinetic energy. A description of the magnetic reconnection process in the frame of the Earth-Space environment is given as a chapter in the textbook by *Kamide & Chian* [2007].

Negative polarity of the IMF B_z component (also referred to as Southward IMF in literature) leads to magnetic reconnection on the sunward side of the magnetosphere, when solar wind field lines connect directly to the geomagnetic field [e.g. *Crooker*, 1975]. Significant solar particle energy can be delivered to ionospheric altitudes in the cusp regions (see Figure 2.1), particularly during the impact of solar wind shock fronts that carry dense plasma. Following reconnection on the dayside, solar wind flow and magnetospheric convection drive effectively open field lines over the poles to the night side and beyond to the elongated plasma tail region [e.g. *Dungey*, 1961]. An accumulation of magnetic flux leads to concentration of field lines near the plasma tail current sheet at a point approximately 100-200 earth radii (R_E) past Earth. Magnetic reconnection at this point is hugely energetic, and stored potential in the elongated solar field lines gets transferred to newly created closed geomagnetic field lines that travel back towards Earth in events known as substorms. Energetic particles from the plasma sheet are delivered to ionospheric altitudes during substorm events, driving intense auroral events on the night side. *Akasofu* [1964] recognised the auroral substorm as a repeating feature of magnetospheric convection by studying ground-based images of the resulting auroral emissions.

The day and night side magnetic reconnection processes summarized above are only the main features of the complex magnetospheric convection system. In reality the magnetosphere's linkage with the solar wind is a changing and fluid interaction whereby particles can enter the atmosphere in a number of places (see Figure 2.1), even during quiet periods. It is possible to have a degree of geomagnetic connection when the IMF is northward (positive B_z), whilst the east/west B_y component determines magnetospheric circulation patterns and connection points. For example *Shi et al.* [2013] have recently reported significant amounts of quiet solar wind input to the high-latitude magnetosphere, measured by the Cluster satellites in regions tail-ward of the open cusp entry points. In situ satellites provide the best measurements of the interplanetary medium and magnetospheric linkage conditions. The most important of these within the past two decades has been the Advanced Composition Explorer (ACE), which sits at the first Lagrangian orbit point between Sun and Earth, making continuous observations of the solar wind composition, speed, density, temperature and IMF orientation (see Figure 5.2 as an example). By data transmission it can provide advanced warning of shock front arrival or IMF perturbations at the magnetosphere, an important service for astronauts and satellite operators, and a useful tool for ionospheric research. A more complete description of the solar wind and its interactions with the magnetosphere can be read in books by *Tascione* [1994] or *Hunsucker & Hagreaves* [2003], together with helpful diagrams.

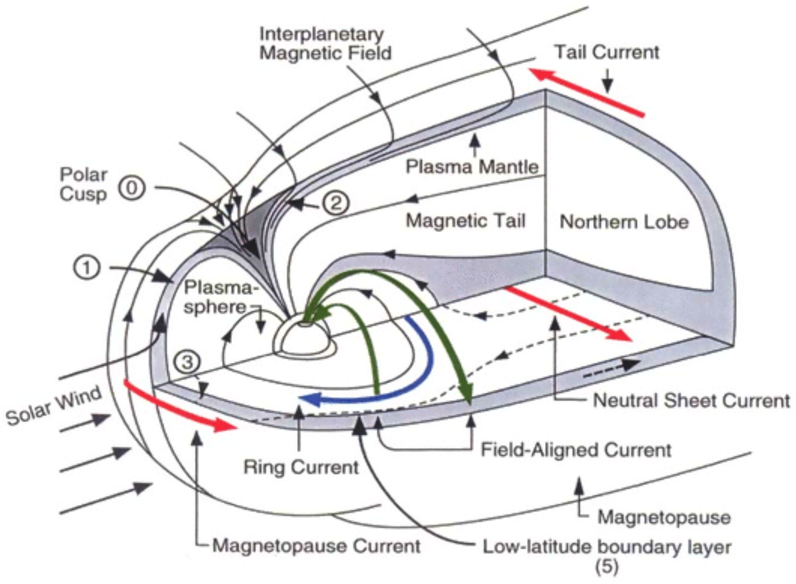

Figure 2.1: Schematic illustration of magnetospheric topology with boundary layers toward the solar wind. The following plasma regions have been marked: (0) exterior cusp, (1) low-latitude boundary layer in the subsolar region, (2) high-latitude boundary layer (plasma mantle), (3) dayside extension of the central plasma sheet, and (5) the low-latitude boundary layer along the postnoon flank. Magnetospheric current sheets, Birkeland currents, and the ring current have been marked by red, green, and blue arrows, respectively.

Figure 2.1 – A three dimensional diagram of the magnetosphere with cross section, showing its major current systems and boundary layers where particles can enter from the solar wind. *Sandholt, Carlson & Egeland* [2002]; with kind permission from Springer Science+Business Media B. V.

2.2 The ionosphere's global morphology

Surrounding the Earth, the ionosphere is the ionized layer of the atmosphere that extends from ~60 km to over 1000 km altitude. It is composed of free electrons and positive ions, generally in equal numbers, in a plasma medium that is electrically neutral. The charged particles are small in number compared to the neutral atmospheric components, but the electrons hold great influence over the electrical properties of the medium, and their presence allows the possibility of radio communication over large distances. The early history of the ionosphere is strongly associated with the development of radio communications, such as the first trans-Atlantic transmissions by *Marconi* in 1901. *Kennelly* and *Heaviside* later suggested that Marconi's transmissions, because of the Earth's curvature, must have been reflected by an ionized layer. Subsequent research has revealed the ionosphere's vertical structure, its temporal and spatial variations, and the physical processes that drive its formation and circulation.

The ionosphere's formation and composition are driven mostly by the Sun, so its structure and behaviour are highly variable across the globe. A balance of production and loss processes govern the ionosphere's presence in the atmosphere. There are multiple catalysts contributing to ionospheric production, including extreme ultra-violet (EUV) solar radiation and energetic particles from space. The most dominant process globally is photo-generation of free electrons through EUV and X-ray exposure of the neutral atmosphere. This reaction is demonstrated in Equation 2.1, where X is an atmospheric gas particle, typically oxygen or nitrogen in atomic or molecular form.

Photo-generation of free electrons: $\mathrm{X} + v \rightarrow \mathrm{X}^+ + \mathrm{e}$ (2.1)

Production at high latitudes also occurs through collisions between incoming solar particles and neutral atmosphere components, a process discussed in Section 2.3.2. Loss of the ions is by two main recombination processes, direct and dissociative. The majority of recombination in the ionosphere occurs at night, when there is a lack of incident solar radiation, i.e. the rate of loss becomes greater than the rate of production. Direct recombination sees a free electron recombine with a positive ion in a single charge transfer:

$$\mathrm{X}^+ + \mathrm{e} \rightarrow \mathrm{X} + \mathrm{h}v \tag{2.2}$$

Dissociative recombination is more common and involves two stages. The positive charge is first exchanged between the ion and a common molecular species (such as O or N_2), and then the charged molecule is dissociated by recombining with a free electron.

$$\text{i)} \qquad \mathrm{X}^+ + \mathrm{A}_2 \rightarrow \mathrm{AX}^+ + \mathrm{A} \tag{2.3}$$

$$\text{ii)} \qquad \mathrm{AX}^+ + \mathrm{e} \rightarrow \mathrm{A} + \mathrm{X} \tag{2.4}$$

The movement of ionized particles also governs the balance of production and loss. Various transport mechanisms hold influence on the ionosphere, including diffusion, neutral winds, and electromagnetic drift. Complete descriptions of ionospheric chemistry and morphology are available in the textbooks by *Tascione*, [1994], *Kelley* [2009] and *Rees* [1989]. The rate of ionization at any altitude depends on two main factors; atmospheric composition, and the characteristics of the incident radiation at that height. The intensity of solar EUV light becomes greater with increase in altitude; however atmospheric density decreases. As solar radiation propagates down through the neutral atmosphere, the various frequency bands of this radiation are attenuated and absorbed by different amounts; different types of molecules and atoms are ionized by different wavelengths of radiation. Consequently, different ionization processes become dominant at different heights, resulting in a multi-layer structure with maxima in electron density – generalised by the term 'ionosphere.'

The principal layers are designated D, E and F, each being characterised by a different set of ionization processes. These regions themselves have sub-divisions, being E, Es (sporadic-E), F1 and F2. The vertical structure of the ionosphere, amount of layers, their heights and electron densities, all vary with time and in space. An approximated vertical profile of the ionospheric layers is shown in Figure 2.2, distinguished by altitude and electron density. Dashed and solid lines indicate the variations experienced during periods of solar minimum and maximum respectively.

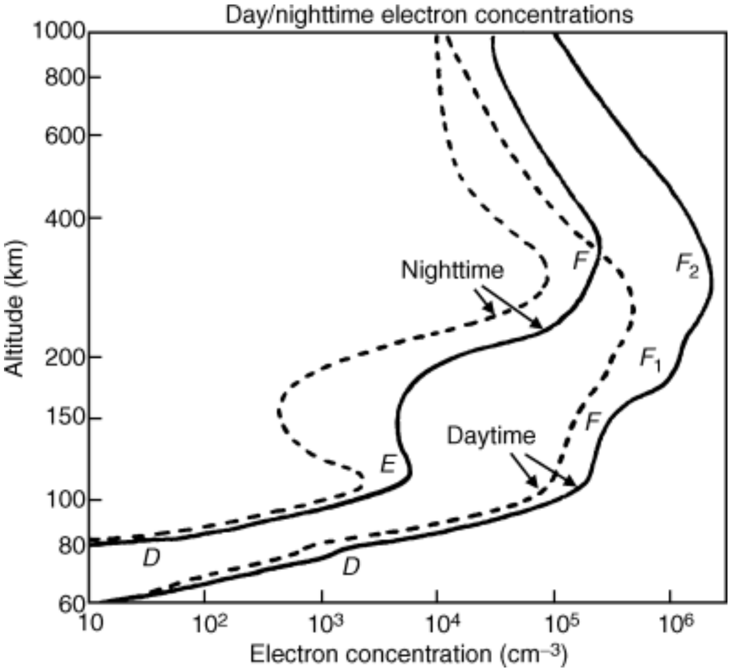

Figure 2.2 – A vertical profile of the ionospheric electron concentration layers, with extents shown for day and night time. Dashed lines indicate the profile during solar minimum and solid lines during solar maximum. Image reproduced and adapted from [*Barclay*, 2003].

Electron density layers have pronounced maxima during the daytime, with roughly an order of magnitude decrease or more at night time; only the F2 and E regions may remain at night. Dependence on the solar cycle is also shown in Figure 2.1, with markedly higher electron concentrations during a maximum period. The solar dependency of ionospheric behaviour exists on three main periodic timescales:

- Diurnal – throughout the day.
- Seasonal – throughout the year.
- Solar activity – the 11-year solar cycle (and subsequent solar wind conditions).

In summary the ionosphere is non-uniform globally, existing mainly above the Sun-illuminated side of the globe where solar UV radiation is most intense. The incidence angle of UV radiation becomes more oblique with increase in latitude, and photo-production falls off towards the Poles. The terrestrial ionosphere can be categorised broadly in to three main latitudinal regions. The high-latitude ionosphere is the main focus of this research, and is described in Section 2.3.

2.2.1 Low and equatorial latitudes

Generally ionospheric electron density should be at maximum at the dayside equator during equinox, when the Sun is directly overhead and ionization rate is at maximum [*Hargreaves*, 1979]. The equatorial ionosphere is host to some of the largest electron concentrations on Earth during the day. Its strong interaction with radio transmissions has rendered the equator an extensive area of ionospheric study [e.g. *Gwal et al.*, 2004].

At the geomagnetic equator, field lines are aligned horizontally overhead along a South-North orientation. Also present is a horizontal electric field directed to the East, generated in the E region. The ionosphere is first lifted at the equator by daytime tropospheric heating. In the presence of both an electric and magnetic field, electrons are carried aloft by electromagnetic drift (E×B force). Constrained by the magnetic field lines, the plasma is then guided to higher latitudes, converging in two F region bands at ±15° from the geomagnetic equator; the equatorial or Appleton anomalies. The mechanism as a whole is referred to as the fountain effect, which was first described explicitly by *Hanson & Moffett* [1966].

After sunset the plasma remains suspended throughout the night in the presence of the horizontal magnetic field. Recombination can be a slow process at higher altitudes because of the low density of the neutral atmosphere. Subsequently, 'bubble' structures can form in the plasma from its underside (via the Rayleigh-Taylor instability), rising upwards for a few hundred to a thousand kilometres [e.g. *Kintner et al.*, 2007]. These depletion regions also elongate along the magnetic field lines, and can move gradually to higher latitudes. The consequence of such instability is a lingering, drifting area of high electron density gradient, which can be extremely problematic for ionospheric radio communications during the night. Sunrise sees an increase in ionizing production rate, and depletion regions are filled in; the ionosphere returns to its more stable daytime form.

2.2.2 Mid-latitudes

Hunsucker & Hargreaves [2003] claim that the mid-latitude ionosphere is the region most explored and best understood by science. This is understandable given that human population is concentrated mainly within these latitudes, and founding knowledge of the ionosphere stems from radio communication between people (e.g. *Marconi*, 1901). Although widely accepted that ionization here is mostly produced by direct solar EUV and X-ray exposure, *Kintner*'s review of GPS and ionospheric scintillation [2007] suggests that the mid-latitude ionosphere is indeed the least understood in its behaviour. In the presence of secondary coupling effects, coming from strong activity at the magnetic equator and auroral regions, it is difficult to isolate processes that are inherent to mid-latitudes. *Kintner* argues that attention and resources are focused on the more active equatorial and high-latitude ionospheres, meaning the mid-latitude becomes neglected in terms of useful observation. The growth of global monitoring networks and modelling improvements will help to develop knowledge of the mid-latitude ionosphere and its effects on radio propagation.

2.3 The high latitude ionosphere

At latitudes above ~60 degrees in the Northern and Southern hemispheres, ionospheric behaviour changes markedly from that observed elsewhere on Earth. Globally, the ionosphere is produced almost entirely from solar EUV and X-ray radiation, but at high latitudes magnetospheric interaction has a dominant role. Here the geomagnetic field lines tend towards a vertical orientation, along which trapped solar particles (due to the

Lorentz force) accelerate downwards into the upper atmosphere. Energetic particle precipitation can penetrate a range of altitudes, adding to free electron production through collisional reactions. This additional ionization can be extremely localised and sporadic, particularly during periods of geomagnetic disturbance. Another consequence of vertical field line geometry is the circulation of ionospheric plasma at high latitudes in drift patterns associated with magnetospheric linkage. The twisting magnetic components of a perturbed solar wind stream can influence and transform these flows completely. A complex mixture of production, loss and transport therefore exists in the high-latitude ionosphere, which leads to some of the most dynamic and unpredictable behaviour and structuring found on Earth. Current knowledge of the subject is very clearly laid out in the textbook by *Hunsucker & Hargreaves* [2003].

2.3.1 Circulation, storms and irregularities

The reconnection and movement of IMF-connected terrestrial field lines over the polar regions maps down to the ionosphere, manifesting as a permanent and highly variable electromagnetic E×B plasma convection system. This is more or less fixed with respect to the Sun-Earth line, and so the Earth and, to a much weaker extent its neutral atmosphere, rotate underneath the plasma flow. When IMF B_z polarity is negative, a dual cell circulation pattern is set up at high latitudes with a strong anti-sunward flow across the polar cap, and subsequent return flow along the dawn and dusk sectors. Plasma circulation is weaker during prevalent quiet conditions, when B_z is positive, but the flow can exhibit a more complex quad-cell pattern. The east/west orientation of the IMF, the B_y vector component, modulates the position of the convection system along the dawn-dusk axis as illustrated in Figure 2.3. A more recent depiction of these two main high latitude plasma convection systems is shown in Figure 2.4, as electric potential maps based on statistical evidence from six years of in situ satellite data.

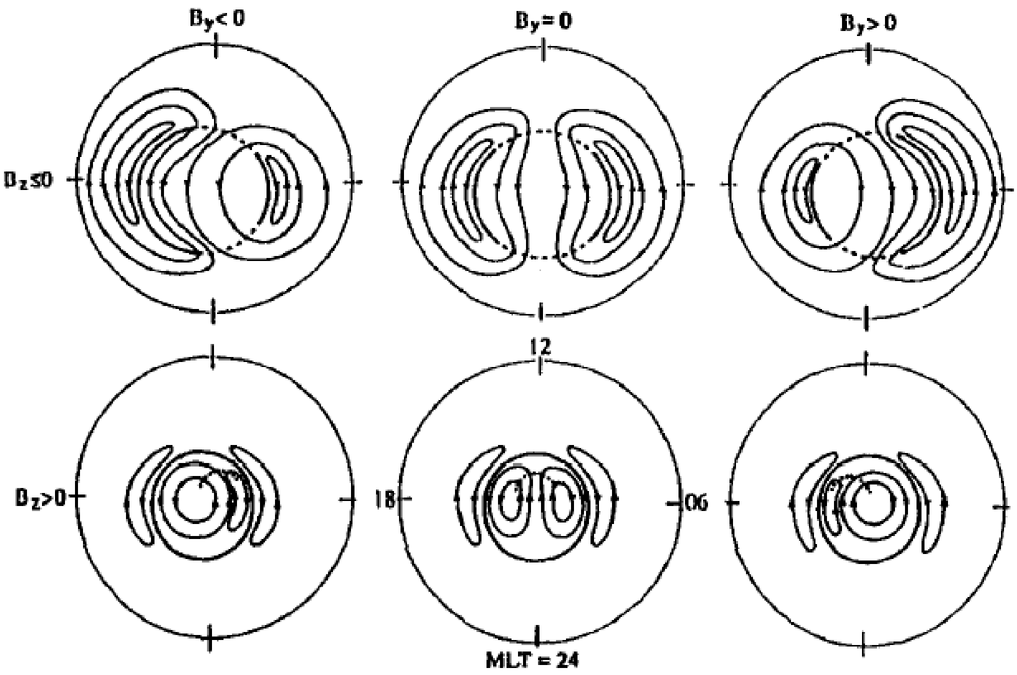

Figure 2.3 – Sketches of plasma-flow convection patterns (solid lines) in the northern hemisphere with varying IMF direction (top row $B_z < 0$, bottom row $B_z > 0$). Note the characteristic dual plasma-flow cells during negative B_z conditions, and the pattern's shift in position towards local dawn or dusk sectors according to B_y direction. Positive B_z conditions lead to a more complex but generally weaker quad cell pattern. The central dashed circles represent an approximate boundary of closed and open geomagnetic field lines i.e. extent of the Polar Cap [*Lester and Cowley*, 2000, after *Cowley*, 1998].

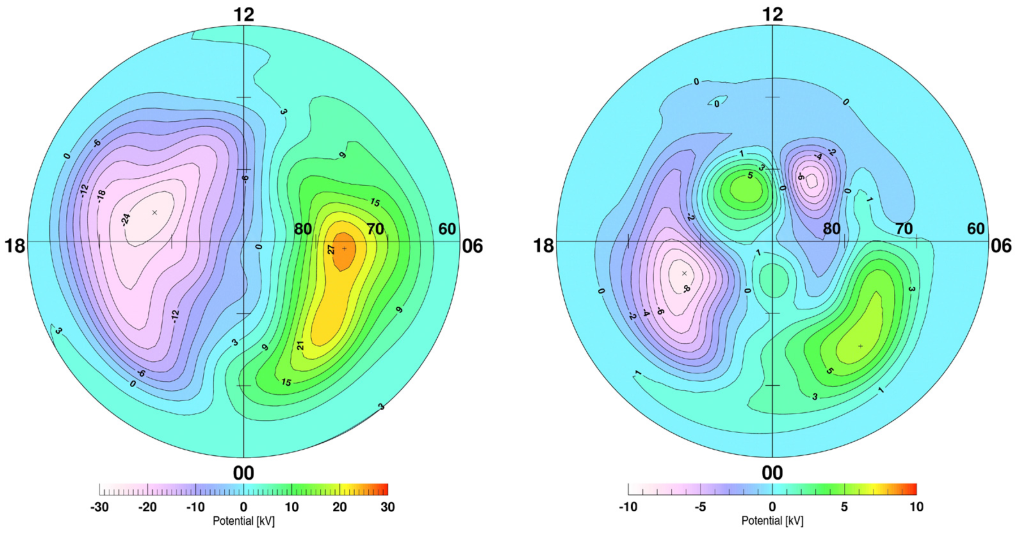

Figure 2.4 – Electric potential maps showing plasma convection flow patterns for southward B_z (left) and northward B_z conditions (right), based on six years of in situ electron drift measurements made by the multi-satellite Cluster mission [*Haaland et al.*, 2007].

The most important source of production in the global ionosphere is photoionization by sunlight. At high latitudes this process is restricted to the partially sunlit portion of the Earth, up to the solar terminator line that moves across the polar region with diurnal and seasonal variation. On the nightside of the hemisphere plasma recombines quickly in the E-region, while at higher altitude the F-region is more slowly eroded because of the lower neutral atmospheric density. When the large-scale convection system is imposed on this simple photo-production and recombination-loss relationship, the solar plasma can be drawn from the dayside and transported over large distances into the night side before recombining. In this way, even quiet magnetospheric conditions can produce more complicated plasma morphology than the simple effect of the solar terminator. Conversely the winter hemisphere can exhibit regions of marked electron density depletion on the nightside, when higher latitudes experience very little or no sunlight throughout the day. This effect is pronounced in the dusk-midnight sector when ionospheric convection flows are slowed by co-rotation effects from the plasmasphere, resulting in a mid-latitude trough at ~60° [e.g. *Brinton et al.*, 1978; *Kelley*, 2009].

Disturbed magnetospheric conditions can bring about some of the most interesting ionospheric phenomena at high latitudes. 'Storm' events are likely when the IMF linkage is strong, and the magnetosphere is compressed by fast and dense solar wind flows. The occurrence of these storms varies with the solar cycle, with the last solar maximum year of 2003 seeing 28 disturbance events with planetary magnetic index $K_p > 5$ (see Section 4.6.1). In contrast the recent solar minimum of 2009 was absent of any events with $K_p > 5$ (source: Kyoto Geomagnetic Database).

Generally a storm event transpires as three main phases in time, but can last between a few hours to a week. The initial impact phase constitutes the solar wind shock front arrival at the magnetopause, and magnetic compression on the dayside. This often leads to sudden injection of energetic solar particles into the ionosphere through the polar cusp, cap and auroral latitudes. This is one source of atypical ionospheric structuring, as E and F regions are enhanced by precipitation on multiple spatial and temporal scales. The main phase of the storm follows, which can be visualised as the Earth sitting in the wake of the initial shock front that typically exhibits the largest IMF deviations. This is the longest stage of a storm, and ionospheric convection patterns are set up in response to IMF changes and field line movement over the poles. Anti-sunward convection velocities can easily reach several hundred ms^{-1} (measurable using ionosonde Doppler techniques or HF backscatter radar e.g. *Grant et al.*, [1995]), carrying dayside plasma past the solar terminator and across the polar cap and auroral oval. A resulting ionospheric feature is the 'tongue' of ionization (TOI), a large-scale elongated plasma structure stretching from the dayside and across the auroral oval, having been transported from mid-latitudes in the noon sector near the cusp [e.g. *Foster*, 1993]. They are observable as enhancements in Total Electron Content (TEC, see Section 4.1) that can reach up to a few thousand km in length and hundreds of km wide, and can display severe electron density gradients and structure breakup at their edges [e.g. see review by *Tsunoda*, 1998].

Plasma 'patches' are an irregular feature of the F-region at high latitudes that sometimes develop after TOI structuring. Patches are enhancements of plasma between 50-1000 km across that 'break-off' from the dayside plasma or TOI structure, and drift in an anti-sunward direction across the polar cap [e.g. *De Franceschi* et al., 2008]. Their electron densities can be as much as a factor of ten above the surrounding background plasma on the night-side, where they can linger due to slow recombination rates at F-region altitudes. The exact causes of these patch break-off events are not yet fully understood, but it is known that changes in the incident IMF conditions (particularly the B_z component) and subsequent convection patterns are primarily responsible [e.g. *Sojka et al.*, 1993; *Decker et al.*, 1994]. It is also believed that enhanced eastward and westward electrojet flows in the late morning and early afternoon sectors lead to enhanced recombination rates in the F-region, depleting the ionization in narrow regions and isolating patches from TOIs [e.g. *Sellek et al.*, 1991; *Idenden et al.*, 1997; *Moen et al.*, 2006]. The dissipation of a patch structure may happen in a number of different ways, either depleting eventually through recombination, merging with the mid-latitude ionosphere, or becoming stretched along the auroral latitudes in the sunward return flow of a convection pattern. Some recent observations of plasma patches are referred to in Chapter 3.

2.3.2 Particle precipitation & the aurora

A significant amount of energy is delivered to the high latitude ionosphere via precipitation of solar particles. At times, they dissipate over ten times the energy deposited by incident solar radiation at ionospheric altitudes [*Sandholt*, 2002]. The majority of this energy input occurs at auroral latitudes, where the Earth's geomagnetic field lines are open to the solar and plasma tail particle populations in the magnetosphere. The auroral oval is a prominent feature of the high latitude ionosphere, discovered by *Feldstein* in 1963 using all-sky camera data. It exists as a dynamic ring of enhanced electron density encircling the polar cap in each hemisphere, formed by solar particle precipitation and subsequent collisional ionization. Energetic particles are known to enter ionospheric altitudes through the dayside polar cusp and nightside footprint of the magnetotail [see for example *Sandholt et al.*, 2002]. It is known from ultraviolet satellite images that the auroral oval is always present to some degree [e.g. *Huffman*, 1992], but it expands and intensifies readily during geomagnetic storms when the prevailing solar wind is fast and dense. High flux and energy levels of particle precipitation lead to enhanced electron densities at E and F region altitudes [e.g. *Robinson & Vondrak*, 1985], which either linger and drift with convection patterns or recombine quickly depending on magnetic location and altitude. The auroral oval morphology is a critical aspect of high latitude radio communications, as electron density gradients and recombination structuring can affect signal propagation conditions. The extents of the auroral oval, the equator-ward and pole-ward boundaries, have been adopted as fundamental indicators of space weather activity and driver inputs to leading ionospheric models (e.g. *Zhang et al.* [2010] & IRI 2012, www.irimodel.org).

Collisional ionization around the auroral oval leads to one of the most well known ionospheric phenomena, the visible aurora. The photons that make up auroral emissions are actually the by-product of ionization, released as excess energy when excited ions return to a relaxed state. The brightest visible emissions result from recombination of atomic oxygen at two main levels of excitation [e.g. *Kelley*, 2009]:

$$\mathrm{O}\ (^{1}\mathrm{D}) \rightarrow \mathrm{O}\ ({}_{3}\mathrm{P}) + \mathrm{h}v\ (630.0\ \mathrm{nm}) \qquad (2.5)$$

$$\mathrm{O}\ (^{1}\mathrm{S}) \rightarrow \mathrm{O}\ (^{1}\mathrm{D}) + \mathrm{h}v\ (557.7\ \mathrm{nm}) \qquad (2.6)$$

These reactions produce red (Equation 2.5) and green (Equation 2.6) emissions at characteristic altitudes of around 120 km and 200 km respectively; although the aurorae are field-aligned structures and so extend across a wide altitude range. Figure 2.5 is a long exposure photograph showing these emissions. The full spectroscopy of auroral emissions is explained in [*Sandholt*, 2002].

There are many observable forms of visible aurora, ranging from wide-area diffuse brightening (hundreds of km) to discrete arcs and 'wisp' structures (hundreds of metres) [e.g. *Davis*, 1978; *Haerendel et al.*, 1996; *Dahlgren et al.*, 2010; *Sandahl et al.*, 2011]. It has been observed that these optical emissions are closely correlated with the sporadic electron density structuring in the ionosphere [e.g. *Benson*, 1960; *Sears & Vondrak*, 1981; *Hunsucker et al.*, 1995; *Stoker et al.*, 1996; *Kintner et al.*, 2002], but this physical relationship is complex and difficult to quantify.

Figure 2.5 – Long exposure photograph of the *aurora Borealis* above Sweden. The visible red and green emissions arise from the relaxation of excited oxygen atoms, following collisions with field-aligned solar and plasma sheet particles that spiral down from the magnetosphere. Used with permission from Professor Yusuke Ebihara (Kyoto, Japan).

2.4 Ionospheric scintillation

Irregularities in the ionosphere's electron density have a significant influence on radio wave propagation. A primary focus of this research is the study of an effect called scintillation, the rapid fluctuation of a radio signal's phase and amplitude. This phenomenon is attributed to the presence of ionospheric irregularities via refraction and diffraction processes, but at this point it is useful to describe the concept from a more visual perspective. The effect of scintillation on the Global Positioning System is treated separately in Chapter 4.

The word 'scintillation,' in a dictionary, can be attributed to the twinkling or tremulous nature of light from the stars. This definition is a useful starting point when considering scintillation as an atmospheric phenomenon. Any electromagnetic signal travelling over a distance is subject to degrading effects as it propagates. A star can appear faint to the unaided human eye, because its intense visible radiation emissions decrease in amplitude gradually through absorption over the long time taken to reach Earth. It is also known that, because of the huge distances involved, the light seen from Earth will have left a star long before it is perceived; this is an example of propagation delay.

The observed small-scale 'twinkling' occurs due to effects experienced by the light signal within the Earth's atmosphere. The atmosphere is very dynamic, varying in composition, density and conductivity over altitude and time. From an observer's position on Earth, the line of sight to a star is a narrow, irregular path through the atmosphere (and space beyond). The weak light is dispersed by diffraction and refraction, and as a result appears, to the human eye, to fluctuate slightly in shape and brightness. Hence, the twinkling of a star.

A satellite-Earth radio signal is subject to the same atmospheric effects described above, to some approximation. The GPS can be described as a 'weak-signal' system – its air-borne signals traverse great distance, and are transmitted with the low power that a satellite can sustain. The atmosphere therefore has some significance in the performance of the system, as it directly affects signal integrity. Propagation delay and decay are common to any communications system, but at GPS frequencies, ionospheric scintillation is an important problem. GPS propagation and scintillation effects are discussed in more detail in Chapter 4.

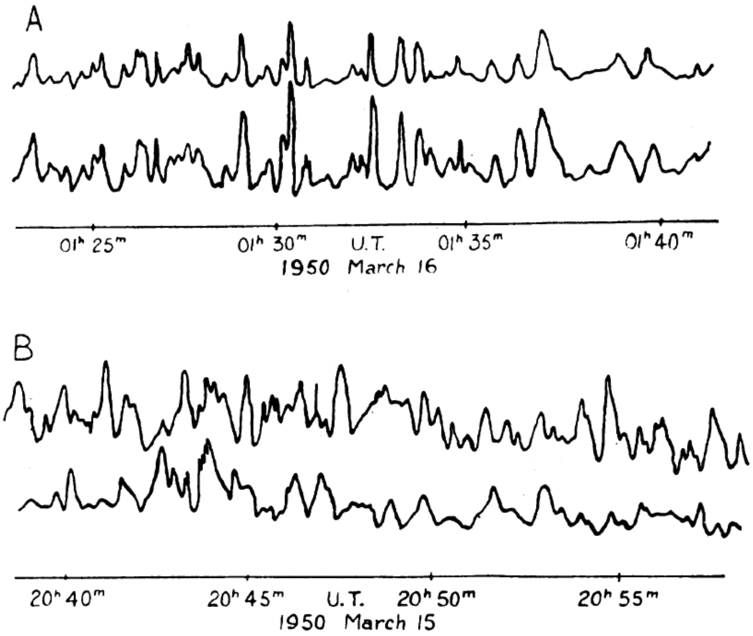

Figure 2.6 - Simultaneous amplitude fluctuation recordings, observed from the Cassiopeia constellation by two receivers spaced 11 km apart. Record ‘A’ shows good temporal correlation, giving some indication of the irregularity’s area of influence on the ground [*Booker*, 1958].

Some of the first indications of radio scintillation became apparent during the post WWII 1940s and 1950s, when much improved communications equipment allowed the observation of radio emissions from discrete sources of cosmic noise (commonly radio stars). Early recordings showed variation in received signal strength, so it was proposed initially that the source itself may fluctuate in emission intensity [*Hey, Parsons and Philips* in 1946, observing cosmic noise of the Cygnus constellation at 68 MHz]. A more plausible explanation however, was that the radio signal was being altered at some point during transit along its propagation path.

As more people began to observe cosmic radio emissions, it was discovered that there was no correlation between the received signal fluctuations at significantly distant points on the ground [*Smith*, 1950]. There was however fairly good agreement between signal recordings made at locations within a kilometre or so of each other. This revelation led to the concept of irregularities in the Earth’s atmosphere having effect on propagating radio waves. The propounded theory generally described a ‘shadow’ being formed by the irregular areas of electron density, the extent of which could be measured on the Earth by the correlation agreement between spaced receiver amplitudes, as demonstrated in Figure 2.6 [*Booker*, 1958].

2.5 Summary

This concludes the Chapter introducing the ionosphere. An overview of the Sun-Earth system placed the ionospheric research in a wider context. The basic properties of the low and mid-latitudes have been described, followed by the more complicated features at high latitudes where the ionosphere is more closely coupled with the magnetosphere. The chapter concluded with an introduction to the concept of ionospheric irregularities and radio scintillation. The next Chapter provides a literature review about the high latitude ionosphere with a focus on radio system observations and applications.

3 Literature review

This Chapter is a review of the high latitude ionosphere with a focus on radio system observations. Recent developments in ionospheric imaging and scintillation studies are reviewed, concluding with the main questions that this research aims to explore.

3.1 Recent work in the Antarctic and Arctic

This research aims to combine the fields of ionospheric imaging and scintillation monitoring, to better understand the processes causing scintillation at high latitudes. The methods applied in this thesis are described in Chapter 4, but the motivation for the work stems from the progress made in recent years in the Antarctic and Arctic. This section reviews some key advances in the combined fields of ionospheric tomography, GPS scintillation monitoring, and auroral imaging at high latitudes.

3.1.1 Combined ionospheric imaging and scintillation observations

It is well known that solar disturbances can cause periods of geomagnetic and ionospheric disturbance that affect Global Navigation Satellite System (GNSS) signals. Signal refraction and diffraction via small-scale electron density structuring (tens of kilometers down to hundreds of meters) can result in amplitude and phase scintillation (see Section 4.1 and 4.2). Severe scintillation conditions pose significant problems to GNSS receivers, such as signal power fading and phase jitter (see Section 4.4). GNSS scintillation is well known at equatorial latitudes [e.g. *Basu et al.*, 2002] and has important implications for navigation. Reports of GNSS amplitude scintillation at high latitudes are less common; *Smith et al.* [2008] show an event associated with an auroral arc during a substorm. Phase scintillation is more common at high latitudes, for example *Mitchell et al.* [2005] report phase scintillation on the edge of polar cap patches in the high European Arctic, and *Ngwira et al.* [2010] associate phase scintillation in the Antarctic with auroral electron precipitation. *Burston et al.* [2009] show evidence for both plasma turbulence and the gradient drift instabilities for the production of electron density irregularities at high latitudes. Even though the general mechanisms are broadly thought to be known, the mechanisms causing particular scintillation events in the high latitude ionosphere are not always easy to trace. Moreover, quantifying them and developing a confidence about the exact cause of an event is still quite rare.

GPS (Global Positioning System) signals can be used to observe the ionosphere over a large area through inversion tomography techniques (see Section 4.5). Imaging the high latitude ionosphere is a particularly useful application of GPS tomography, as a multi-instrument philosophy is required for observation of the complex physical processes that exist there [e.g. *Bust & Mitchell*, 2008]. For example a wide-area picture of the plasma morphology is important in understanding geomagnetic storm features and their development. Typically these high latitude electron density reconstructions can be verified using a combination of Incoherent Scatter Radar (ISR) profiles, ionosondes, and independent satellite-based TEC (see Section 4.1) or occultation profiles. Many ionospheric storm studies have used GPS tomography in resolving polar cap plasma patches and Tongues of Ionization (TOI) [*Bust et al.*, 2007, *Bust & Crowley*, 2007, *Pokhotelov et al.*, 2010, *Yin et al.*, 2009, *Spencer & Mitchell*, 2007, *Kinrade et al.*, 2012]. With the current geographic distribution of some 50 GPS receivers across Antarctica, electron density structures of scale hundreds of kilometers across can be imaged. This is too low in spatial resolution to see structures directly responsible for GPS scintillation; however the images have been effective in locating regions of disturbance in the Arctic that correlate with scintillation activity [e.g. *De Franceschi et al.*, 2008]. Specialised GPS scintillation receivers have already been deployed for several years in the Arctic [e.g. *Prikryl et al.*, 2010; *Spogli et al.*, 2009]. This thesis reports on results from a new network of dedicated GPS scintillation receivers deployed at high latitudes in the Antarctic during a geomagnetic storm (see Chapter 5).

One recent study has correlated many high-latitude scintillation measurements in a comprehensive inter-hemispheric conjugate study during a geomagnetic disturbance [*Prikryl et al.*, 2011]. The results indicate both symmetries and asymmetries in the ionospheric response and scintillation occurrence, demonstrating the complexities and dynamic nature of the physical mechanisms acting at high-latitudes. It is accepted that seasonal axial tilt and asymmetry in the geomagnetic field render the Arctic and Antarctic ionospheres subject to different energy input and magnetospheric linkage for any given solar event.

The majority of high-latitude Global Navigation Satellite System (GNSS) scintillation studies associated with auroral activity has been on a single case study basis. *Garner et al.* [2011] report a case of L2 (1227.60 MHz) signal loss associated with an auroral arc over

Fairbanks, Alaska. *Smith et al.* [2008] observed, on multiple and closely sited GPS receivers, rapid signal fading and loss of GPS satellite lock associated with an optical arc and auroral precipitation over Norway during a geomagnetic substorm. Chapter 6 introduces a new technique for combining scintillation measurements with optical all-sky imager data, in an effort to improve our ability to match scintillation activity with specific small-scale structuring.

Ionospheric irregularities are too small and dynamic to be imaged directly by current GNSS tomography methods (which have a minimum horizontal resolution of ~100-200 km depending on measurement coverage). At high latitudes they are typically associated with field-guided particle precipitation or the break-up of larger bodies of enhanced plasma density [e.g. *Fejer et al.*, 1980; *Moen et al.*, 1998]. Although advanced ionospheric imaging and data assimilation methods are now being applied effectively at high latitudes [e.g. *Bust et al.*, 2007; *Kinrade et al.*, 2011; *Yin et al.*, 2009], the achievable resolution of plasma morphology is limited by the density and distribution of the instruments and by the sparse nature of the inversion problem. The regional coverage of high latitude ground-based GNSS receivers has vastly improved over the last decade through active polar campaigns; however the available ray path geometry only supports the reconstruction of large-scale ionospheric features of hundreds of kilometers or more. Ionospheric irregularities are difficult to model or predict; they are usually only observed using ionospheric radars [e.g. *Carlson*, 2012]. Radio propagation models at high latitudes are only just beginning to account and mitigate for the physical mechanisms that cause ionospheric irregularities and scintillation [e.g. *Aquino et al.*, 2009; *Strangeways*, 2009].

3.1.2 The auroral oval

Global Positioning System (GPS) signals are sensitive to the auroral ionosphere. E and F region ionization enhancement and auroral arc structures within the auroral oval and polar cap are strongly associated with fast GPS TEC fluctuations and refractive phase scintillation [e.g. *Aarons et al.*, 2000; *Garner et al.*, 2011; *Kintner & Kil*, 2002]. *Coker et al.* [1995] demonstrated that the equator-ward oval boundary can be broadly located using a single GPS ground station (Fairbanks, Alaska), by examining slant TEC fluctuations from all observed satellites and mapping instances above a threshold value associated with E region irregularities. The equator-ward boundary of the auroral oval is effectively the pole-ward edge of the ionospheric trough [e.g. *Rodger et al.*, 1992], a latitudinal band of electron density depletion that has since been imaged at mid and northern European latitudes using ionospheric ray tomography [*Kersley et al.*, 1997; *Meggs et al.*, 2005; *Baumgardner et al.*, 2013].

The presence of the auroral oval was confirmed in the 1960s through optical studies of its visible emissions, utilising both ground [reviewed by *Feldstein et al.*, 2010] and aircraft-based cameras [*Buchau et al.*, 1972]. The advent of satellite-based imagery in the 1970s allowed topside observation of the auroral morphology to complement the growing array of ground-based cameras [*Akasofu*, 1974]. Some of the first complete images of the auroral oval were provided by the ISIS-II satellite [*Anger et al.*, 1973], with the later Dynamics Explorer-1 (DE-1) [*Frank et al.*, 1982] and Viking [*Cogger et al.*, 1988] satellites producing large databases of images in both visible and ultraviolet wavelength bands. The far and extreme ultraviolet emissions associated with the aurora can be detected in isolation from day-glow emissions using spectrometers or filtering, allowing imagers to resolve the auroral oval in both the nightside and sunlit dayside of the Earth [e.g. *Frey et al.*, 2003; *Huffman*, 1992]. Global ultraviolet imaging from space provides coherent images of the auroral oval in its completeness, allowing the extraction of boundary and shape information [e.g. *Samadani et al.*, 1990; *Longden et al.*, 2010]. Hemispheric comparison studies are a major advantage when enough satellites can provide simultaneous images, and have shown significant polar asymmetries in oval morphology [*Østgaard et al.*, 2007, *Laundal & Østgaard,* 2009]. The IMAGE [*Mende et al.*, 2003] and Polar [*Brittnacher et al.*, 1997] satellites were the last active campaigns to record auroral images from high altitudes (between ~4-9 R_E). At present there are no active satellites capable of capturing the entire auroral oval within a single image.

Determination of the large-scale auroral morphology currently relies on multi-instrument contributions. Wide-area ground networks of all-sky imagers (ASI) can profile the nightside oval and substorm visible emissions in high time resolution of several seconds (but limited to clear sky conditions), such as the THEMIS array [*Mende et al.*, 2007]. Small-scale auroral ionization patterns can be profiled at some high latitude sites by Incoherent Scatter Radar (ISR) [e.g. *Semeter et al.*, 2009], which together can be used to infer prevailing wider scale conditions such as particle precipitation and plasma convection boundaries; *Imber et al.* [2012] suggest that it may be possible with good radar coverage to determine the auroral oval radius. Polar-orbiting weather satellites capture nightside visible auroral images with regional coverage and high spatial resolution, resolving both diffuse and discrete emissions [for example the SUOMI-NPP satellite, *Seaman & Miller*, 2013]. The Tiny Ionospheric Photometer (TIP) on board the low Earth orbit (LEO) COSMIC/FORMOSAT-3 satellites can image ultraviolet emissions on the dayside at 30 km spatial resolution every few seconds, however such data by itself can only be used to produce full statistical auroral oval positions on a monthly average basis [*Tsai et al.*, 2010]. The polar-orbiting Defense Meteorological Satellite Program (DMSP) satellites carry the Special Sensor Ultraviolet Spectrographic Imager (SSUSI), an instrument capable of imaging multiple wavelength bands of the Far Ultraviolet (FUV) spectrum simultaneously. The DMSP satellites currently provide the most complete measurement set of auroral particle fluxes and boundary locations available through derived SSUSI auroral products.

Without high-altitude imaging satellites, data assimilation is required to obtain full and near-real time images of the global auroral oval. The best available service is OVATION [*Newell et al.*, 2002] that uses primarily zenith particle spectrometer data from DMSP satellite passes to produce auroral oval projections and parameters. The spectrometer provides detailed electron and ion spectra that are used to detect the pole-ward boundary (typically the transition from structured characteristic plasma sheet precipitation in the oval to ‘soft’ and uniform polar cap precipitation) and equator-ward edge of the oval. The boundaries from several satellite passes are then extrapolated to a full auroral oval projection using a combination of shape fitting [*Sotirelis, Newell & Meng*, 1998] and a precipitation model [*Sotirelis & Newell*, 2000, *Machol et al.*, 2012]. Other near-real time auroral oval projections can be obtained from the Space Weather Prediction Centre (SWPC) POES service [online: http://www.swpc.noaa.gov/pmap/ (last accessed 7 May 2013)], and the Canadian Space Science service (based on electrojet current flow estimates using ground-based magnetometer data) [online: https://cssdp.ca/ssdp/app/static/related _projects/rt_oval.html (last accessed 7 May 2013)].

There are few reports of auroral oval TEC being identified by ionospheric tomography routinely, despite the method’s potential to do so; *Mitchell et al.* [1995] identified night-side auroral E-region electron density levels of up to 1.35×10^{11} m^{-3} at ~100 km altitude using two-dimensional tomography with signals from the Navy Navigational Satellite System (NNSS) and five receiving stations across Svalbard and Scandinavia. *Meggs et al.* [2005] reconstructed the equator-ward edge of the auroral oval using three-dimensional GPS tomography, with vertical TEC maps showing a latitudinal band of plasma enhancement (20-25 TECU, 1 TECU = 10^{16} electrons m^{-2}) northward of the main trough in the early evening above Scandinavia. Prior to the research in this thesis there have been no published images of the entire auroral oval using ionospheric tomography, likely for two reasons. Firstly, recovery of auroral TEC in tomographic reconstructions requires ray path geometry from substantial receiver coverage, which has been historically poor around remote longitudes of the Arctic Circle. Secondly, electron density associated with the auroral oval is typically only a small contribution of total ionospheric TEC [e.g. *Coker et al.*, 1995], compared with F region plasma convection and dayside enhancement during storms. Auroral TEC levels sit between the ambient dayside maximum and nightside minimum levels (and are present even in the absence of ionospheric storms), and so a midrange treatment of colour scales has been applied in this work to pick out the auroral morphology.

There remains no single method or accepted standard for imaging the complete auroral oval. There are significant efforts to estimate the near-real time auroral oval position in the absence of satellite global imagers, but these could be complemented by the addition of wide area ionospheric electron density maps that GPS inversion tomography can provide.

3.2 Research aims

There are several aims of the research in this thesis:

1) To undertake experimental measurements to quantify the amount of phase scintillation in the Antarctic over an extended period around solar maximum.

2) Through case studies using multiple ionospheric instruments, to relate individual scintillation events observed on GNSS receivers to their ionospheric source and further relate these to the larger Sun-Earth system.

3) To further the potential use of GNSS observations as a tool to investigate the geophysical climate of the polar ionospheres and to demonstrate new techniques mapping the polar ionospheres.

3.3 Summary

This Chapter reviewed recent high-latitude ionospheric imaging efforts, with a focus on combined GPS scintillation studies. Work in large-scale auroral oval imaging was also considered, as the auroral latitudes are strongly associated with irregular ionospheric enhancement in the E and F regions. Finally the main aims of the thesis were presented. Chapter 4 explains the tomographic imaging and scintillation monitoring techniques applied throughout the thesis in search of these aims.

4 GPS as a tool for scintillation and tomographic imaging

The Global Positioning System (GPS) provides a fully global navigation and timing service. Initially a field tool developed for the United States military, the GPS now serves the Earth's population with free-to-use positioning and timing signals. The user community is now global and highly integrated, to the extent that most mobile phone and vehicle owners have access to location services. Safety-critical and precise positioning and timing services exist at the other end of the user spectrum. Applications such as marine platform drilling, global financial trading and air traffic control are heavily dependent on GPS service.

The system consists of a constellation of satellites, a network of ground control stations, and an unlimited number of user receivers. There are 32 satellites in orbit (plus spares) shared among six semi-synchronous orbits at an altitude of ~20,200 kilometres. At least four satellites are visible above the horizon at any time and place on Earth. The GPS can provide accurate positioning in latitude, longitude and altitude, and also a precise timing standard. The operation of the GPS, including signal structure, ranging and velocity determination, is explained explicitly by *Kaplan* [2006].

This chapter discusses the use of GPS for ionospheric study. The fact that GPS signals are affected by propagation through the ionosphere allows its use as a remote sensing tool, in a sense opposed to positioning and timing applications where the ionosphere poses an engineering problem as a source of signal error. Two techniques are introduced. The first is scintillation monitoring, the analysis and interpretation of GPS signal fluctuations caused by ionospheric irregularities and plasma gradients. The second is tomographic imaging, which is used to reconstruct the four-dimensional ionospheric electron density using differential GPS measurements from ground receiver networks. Some additional observation techniques are discussed at the end of the Chapter, which have been used throughout the research for verification of geomagnetic activity and ionospheric electron content.

4.1 Ionospheric propagation and GPS TEC derivation

The propagation speed of a wave in a medium, v, is governed by the refractive index of the medium, n, which can be defined as the ratio of the wave's speed in free space to that in the medium:

$$n = \frac{c}{v} \tag{4.1}$$

Where c is the speed of light in a vacuum. When the group refractive index is greater than unity, as is the general case with the ionosphere, a delay is imparted to the travelling signal. The free electrons in the ionospheric plasma have a dispersive effect on electromagnetic wave propagation, and so this delay is frequency dependent. Differencing or comparing measurements made at various frequencies can therefore provide information about the ionosphere.

The dual frequency signal broadcasts of the GPS (L1 at 1.57542 GHz and L2 at 1.2276 GHz) allow the computation of ionospheric Total Electron Content (TEC), which is a key parameter in ionospheric study. It is an integral measure of electron density, n_e, and is quantified in TEC units (1 TECU is equal to 10^{16} electrons per m^2) as the number of electrons in a hypothetical one metre square column along the satellite-receiver propagation path, l.

$$TEC = \int_r^s n_e \, dl \tag{4.2}$$

The simplest way to measure TEC using GPS is through use of the pseudorange, which is the measured or apparent satellite-receiver distance in metres, expressed here with dispersive (frequency dependent) terms in bold:

$$p = \rho + c(T + \boldsymbol{I} + \boldsymbol{m}) + c(b_s + b_r) + \Sigma \tag{4.3}$$

Where:

$$b_s = clk_s + \boldsymbol{d_s} \tag{4.4}$$

$$b_r = clk_r + \boldsymbol{d_r} \tag{4.5}$$

ρ is the true geometric range (m), c is the speed of light in a vacuum (ms^{-1}), T is the tropospheric delay (s), $\boldsymbol{I}$ is the ionospheric delay (s), $\boldsymbol{m}$ is a multipath and signal noise term (s), b_s and b_r are satellite and receiver timing biases respectively (s), and Σ represents small residual errors (m). Each bias term represents a clock timing error clk, and a dispersive term associated with electronics hardware effects, $\boldsymbol{d}$, as shown in equations (4) and (5).

The phase of the modulated GPS carrier signals can also be used to measure ionospheric TEC, and can be expressed as length units in a similar way to the pseudorange in Equation (4.3):

$$\phi = \rho + c(T - \boldsymbol{I} + \lambda \boldsymbol{A}) + c(b_s + b_r) + \Sigma \tag{4.6}$$

Where λ is the signal wavelength (19 cm at GPS L1 frequency) and $\boldsymbol{A}$ is an integer phase ambiguity, comprising a delay term that is present because the real number of cycles between the satellite and receiver is not known. The difference in polarity of the ionospheric term in Equations (4.3) and (4.6) reflects the fact that the carrier signal experiences a phase advance as it propagates through the ionosphere, and the pseudorange a group delay due to the ionosphere's real and complex refractive indices.

To obtain a measure of TEC it is necessary to isolate the ionospheric delay term $\boldsymbol{I}$ in Equation (4.3) or (4.6), which is proportional to the electron density n_e, by differencing measurements made at two or more different frequencies (some new receivers are able to decode the new civilian L5 signal standard in addition to L1 and L2). By considering radio propagation through a refractive plasma medium, the ionospheric delay imparted to the signal can be related to the electron densities present and hence TEC. The following is a simplified form of the Appleton-Hartree equation for the ionosphere's refractive index, which ignores the influence of the magnetic field and electron-neutral collisions in the plasma [*Davies*, 1996, pp.73]:

$$n^2 = 1 - \frac{n_e e^2}{4\pi^2 \varepsilon_0 m_e f^2} = 1 - k\frac{n_e}{f^2} \tag{4.7}$$

Where n is the real part of the complex phase refractive index, n_e is electron density per m^3, ε_0 is the permittivity of free space, m_e is the mass of an electron, e is the charge of an electron, and f is the signal frequency. k is extracted as a constant for simplicity:

$$k = \frac{e^2}{4\pi^2 \varepsilon_0 m_e} = 80.6 \tag{4.8}$$

From *Davies* [1996, pp.15], the group refractive index, n', is related to the phase refractive index by:

$$n' = \frac{d}{d\omega}(\omega n) \tag{4.9}$$

Where ω is the angular frequency equal to $2\pi f$. Using the first approximation of the binomial expansion series, Equation (4.7) can be written as:

$$n = \sqrt{1 - k\frac{n_e}{f^2}} \approx 1 - k\frac{n_e}{2f^2} \tag{4.10}$$

Combining Equations (4.9) and (4.10) it follows that:

$$n' = \frac{d}{d\omega}\left(\omega\left(1 - \frac{k}{2f^2}n_e\right)\right) \tag{4.11}$$

$$n' = \frac{d}{2\pi df}\left(2\pi f\left(1 - \frac{k}{2f^2}n_e\right)\right) \tag{4.12}$$

$$n' = \frac{d}{df}\left(f - \frac{k}{2f}n_e\right) \tag{4.13}$$

$$n' = 1 + \frac{k}{2f^2}n_e \tag{4.14}$$

Thus, the ionospheric delay term in the pseudorange is given by the integral:

$$I_f = \int_r^s (1 - n')dl = \frac{k}{2f^2}TEC = \frac{40.3}{f^2}TEC \tag{4.15}$$

Note that the ionospheric delay term in the carrier phase is expressed the same way as Equation (4.15) but with opposing sign signifying a phase advance.

Given the relationship with ionospheric delay in Equation (4.15), TEC is therefore found by differencing dual-frequency pseudorange measurements to remove non-dispersive terms and isolate the ionospheric term in Equation (4.3):

$$\Delta p = p_{L2} - p_{L1} = c(\Delta \boldsymbol{m} + \Delta \boldsymbol{I}) + c(\Delta \boldsymbol{d_s} + \Delta \boldsymbol{d_r}) \tag{4.16}$$

$$\Delta \boldsymbol{I} = \frac{\Delta p}{c} - \Delta \boldsymbol{d_s} - \Delta \boldsymbol{d_r} - \Delta \boldsymbol{m} \tag{4.17}$$

The same can be performed on the carrier phase measurements from Equation (4.6):

$$\Delta \phi = \phi_{L2} - \phi_{L1} = c(\Delta \lambda \boldsymbol{A} - \Delta \boldsymbol{I}) + c(\Delta \boldsymbol{d_s} + \Delta \boldsymbol{d_r}) \tag{4.18}$$

$$\Delta \boldsymbol{I} = \frac{\Delta \phi}{c} - \Delta \boldsymbol{d_s} - \Delta \boldsymbol{d_r} - \Delta \lambda \boldsymbol{A} \tag{4.19}$$

Where:

$$\Delta \boldsymbol{I} = \frac{f_{L1}^2 - f_{L2}^2}{f_{L1}^2 f_{L2}^2} 40.3TEC \tag{4.20}$$

The line of sight TEC obtained through pseudorange differencing is an absolute value, but can be noisy because of the multipath and $\boldsymbol{\Delta d}$ terms, known as the inter-frequency biases. These are difficult to measure and remove as they are caused by the relative travel times of the L1 and L2 signals between antenna and control processing unit (CPU) through internal electronics, varying with local temperature and pressure. Carrier phase differencing provides a cleaner TEC measurement, as phase noise is generally two orders of magnitude less than pseudorange noise [*Garner et al.*, 2008]. The phase ambiguity, however, renders this TEC measurement offset from the absolute level. The carrier phase is also susceptible to cycle slips when the receiver's tracking loop responds to rapid changes in the integer ambiguity along the signal path, which must be detected and removed before TEC can be computed [*Kintner, 2007*]. It is then possible to remove the phase ambiguity offset from the TEC using the pseudorange level, obtaining an estimate of TEC that is both low noise and without phase bias. Inter-frequency biases are typically addressed separately from this process [e.g. *Dear et al.*, 2006].

4.2 Fundamental scintillation theory

The radio propagation phenomenon known as scintillation was introduced in Section 2.4 using the example of radio stars. This section explains the fundamental theory of ionospheric scintillation, namely how it develops physically in the presence of irregularities or strong plasma gradients. Ionospheric scintillation affects GPS signals in two ways, refraction and diffraction. Both of these effects originate in the group delay and phase advance that a GPS signal experiences as it travels through regions of free electrons (see Section 4.1).

In the refractive sense, changes in the integrated electron density (TEC) along a ray path can cause phase scintillation, which is dependent on the motion of both the satellite and any structuring present in the ionosphere. An abrupt change in electron density (and therefore refractive index) would be perceived, for example, if a ray path intersected a plasma patch drifting at high velocity in an opposing direction. *Basu et al.* [1998], *Mitchell et al.* [2005], *De Franceschi et al.* [2008], and *Prikryl et al.* [2010] have reported such cases of GPS phase scintillation associated with patch convection in the polar cap. Phase scintillation is also prevalent at auroral latitudes, where electron density concentrations are often field aligned and elongated [e.g. *Fremouw & Lansinger*, 1981, *Pryse et al.*, 1996]. The inclination angle of geomagnetic field lines can be similar to the higher elevation angles of the GPS constellation at auroral latitudes, and so changes in TEC along the moving ray path can be significant in the presence of particle precipitation and auroral arcs [*Burns & Hargreaves*, 1996, *Jones et al.*, 1997]. For example, the highest inclination angle of a GPS satellite at Tromsø (69°N 19°E, Norway) is ~70°, where the geomagnetic field lines are inclined at ~78° (*International Geomagnetic Reference Field 2011* value). A comprehensive experiment by *Aarons* [1997] showed that GPS phase scintillation activity increases when the receiving station is underneath the auroral oval, particularly during geomagnetic storms.

Amplitude scintillation is attributed to diffraction in the presence of irregularities in the ionosphere's electron density. This theory was first developed for the ionosphere by *Booker* [1950] and *Hewish* [1951], and approximates the irregularities as a thin phase-changing screen (illustrated in Figure 4.1). An incident radio wave passing through the screen will experience phase modulation from randomly spaced changes in refractive index. Phase perturbations then develop and evolve as the wave continues to propagate, and constructive and destructive signal mixing distorts the wave front. Scintillation is, in this case, the perception of a local interference field at the receiving antenna. Note that the phase screen imparts only phase changes to the propagating signal, but subsequent interference produces a diffractive-like pattern on the ground. The phase screen model is effectively a two-dimensional compression of the irregularity region, and is a basic tool in the statistical interpretation [e.g. *Yeh & Liu*, 1982] and simulation [e.g. *Deshpande et al.*, 2011] of this multi-scale spatial and temporal problem. The diffractive element of the theory concerns the size and spacing of the irregularities with respect to the signal's wavelength. The irregularities are believed to be 'small-scale' and diffractive if their spatial distribution has dimensions smaller than a parameter known as the Fresnel length [e.g. *Yeh & Liu*, 1982; *Kintner et al.*, 2007]:

$$d_F = \sqrt{2\lambda z} \tag{4.21}$$

Where λ is the signal wavelength (m) and z is the effective distance of a receiver from the irregularity region. At L1 GPS frequency (1575.42 MHz), and assuming an F-region altitude of 350 km for irregularity production, the Fresnel length is ~365 m. In simple terms this can be thought of as the largest spacing of a slit in a diffraction screen that would induce an eventual interference field. Electron density structuring with spatial scales above the Fresnel length is conducive to large-scale TEC gradients and phase scintillation. An irregularity region, in reality, consists of a whole spectrum of spatial scales, which leads to a scintillation spectrum [e.g. *Umeki*, 1977; *Rino*, 1979; *Aarons*, 1982]. The theory outlined here provides only a simple approximation of what in reality is a complex mix of physical processes leading to scintillation. Extensive consideration of scintillation theory can be found in the seminal works of *Rino* [1976; 1979], *Fremouw & Secan* [1984], *Umeki et al.* [1977] and *Yeh & Liu* [1982].

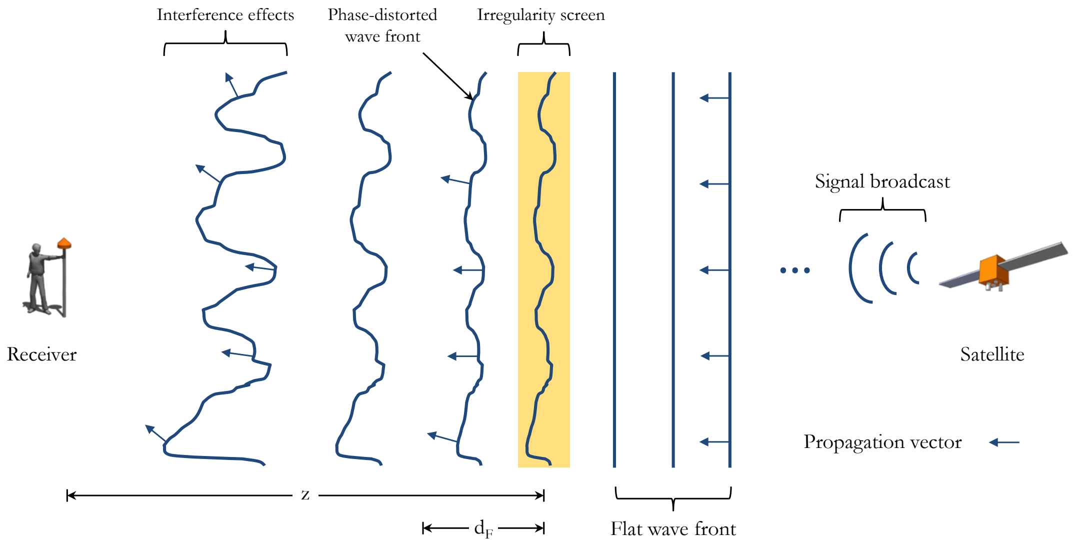

Figure 4.1: A one-dimensional illustration of the thin phase-changing screen approximation for the ionosphere causing diffractive interference on a propagating radio wave. This example shows the signal in context travelling from satellite (right) to receiver (left) through an irregularity screen representing a region of the ionosphere. Using Huygen's principle, the broadcast signal can be approximated as a flat wave front composed of multiple point sources of secondary wavelets. As the wave propagates through the irregularity screen its phase is affected by random fluctuations in refractive index, dependent on the size and electron density distributions of irregularities within the screen. Upon emerging from the irregularity layer the signal's phase front is therefore randomly modulated. These induced phase perturbations then evolve as the wave travels, an effect exaggerated in this figure over distance z. Ultimately an interference field is set up at the receiving antenna, the net effect of constructive and destructive summing along the wave front between virtual point sources of differing phase.

4.3 GPS scintillation – measurement, indices & data treatment

GPS provides a convenient way of measuring scintillation activity on a global basis. Continuous service is provided freely, and many points in space can be sampled simultaneously. Modified GPS receivers are capable of recording signals with fine phase and amplitude information required for scintillation analysis. These receivers are often called ionospheric scintillation monitors, their main hardware feature being an oven controlled crystal oscillator (OCXO) for robust and precise phase tracking. The modified *Novatel* GSV4004 GPS receiver is used throughout this research. This receiver tracks up to 11 satellites simultaneously at L1 (1575.42 MHz) and L2 (1227.60 MHz) frequencies, measuring phase and amplitude changes at a sample rate of 50 Hz. Before scintillation measurements can be analysed, the data must first be treated to remove some effects of signal propagation other than scintillation.

Data 'detrending' is required to remove the satellite motion from the raw data (typically of 50 Hz sampling rate), which otherwise dominates and masks the high frequency scintillation signatures of interest. This is typically achieved with GPS data using a high-pass Butterworth filter of cut-off frequency 0.1 Hz [*Van Dierendonck*, 1993, 1999; *Forte*, 2005]. Conversely, multipath interference and tropospheric absorption can produce high frequency fluctuations on signals from satellites that are rising or setting [e.g. *Benton & Mitchell*, 2011], so an elevation mask is used to reject signals received below ~10-20° above the horizon. Comparing day-to-day repeatability of fluctuations can identify any remaining multipath effects from static reflectors, as the satellite-receiver geometry repeats every 24 sidereal hours. In addition to the elevation angle mask, a minimum lock time may also be specified, so that measurements from a satellite are not recorded until the receiver has acquired lock and tracked the signal for at least several minutes. In essence the detrending stage minimises the impact of the local multipath environment and ensures that scintillation signatures reflect true ionospheric conditions.

Once detrending is complete, indices are computed and used to characterise the received signal amplitude and phase. Amplitude scintillation is measured using the S_4 index [*Briggs & Parkin*, 1963], defined as the square root of the normalised variance of signal intensity during a given time interval:

$$S_4 = \sqrt{\frac{\langle SI^2 \rangle - \langle SI \rangle^2}{\langle SI \rangle^2}} \tag{4.22}$$

Where SI is the signal intensity and $\langle\ \rangle$ denotes the mean value within a time interval. Scintillation receivers record signal intensity as carrier power-to-noise ratio, C/N_0, measured in dB-Hz. This is proportional to the signal-to-noise ratio, S/N_0, provided that the system noise term remains constant over the averaging period. The main source of ambient noise is generated by the effective temperature of hardware electronics, so this is a realistic assumption (e.g. *Forte* [2005] showed thermal noise to be small compared to scintillation level variances, around an order of magnitude less). Scintillation monitors typically calculate S_4 over 60-second intervals, but this is variable whilst the averaging duration is kept long compared to the Fresnel length (see Section 4.2) divided by the irregularity drift speed [*Kintner et al.*, 2007]. Ten-second windowing has been shown to be more effective in detecting the depth of rapid signal fades associated with auroral activity [*Smith et al.*, 2008].

Phase scintillation is measured using the standard deviation of the carrier phase, denoted as the σ_φ index (in radians). GPS scintillation receivers measure phase as an accumulative Doppler range (ADR), measured in cycles, which must also be high-pass filtered for removal of satellite motion. *Forte* [2005] demonstrated that the σ_φ index is sensitive to how data are detrended, and can misrepresent the scintillation-based phase variations. The ideal value for low frequency cut-off depends on the irregularity drift speeds relative to the ray path motion, but this is not readily known and requires close to real-time calculation. In general a cut-off of 0.1 Hz is used.

4.4 GPS performance issues during severe scintillation events

GPS is transmitted at low power, and scintillation activity can potentially degrade or interrupt receiver operation. During normal receiver operation, the code and carrier components of the GPS L1 coarse-acquisition (C/A) signal are typically tracked by a delay-locked loop (DLL) and a phase-locked loop (PLL) respectively [e.g. *Beniguel et al.*, 2011]. To retain signal 'lock,' the PLL makes constant adjustments to minimize the error between the received phase and its estimated phase output, which is then given to the receiver's processor. The magnitude of this tracking error variance or 'jitter' is dependent on thermal noise, oscillator noise and phase scintillation [*Hegarty*, 1997]. The oscillator and thermal noise components place minimum requirements on receiver design in terms of signal reception and quality, however scintillation is more difficult to account for.

Complete tracking loss has been observed on individual satellite links for several minutes during severe scintillation activity at equatorial latitudes [*de Rezende et al*, 2007], where deep fades caused loss of both signal code and carrier. Only a few cases of GPS amplitude scintillation and tracking issues have been reported at high latitudes [*Mitchell et al.*, 2005; *Smith et al.*, 2008], which were short-duration events (10 seconds) associated for the first time with diffractive auroral processes. Typically the field aligned electron density structuring at high latitudes leads to a prevalence of phase scintillation over amplitude scintillation at GPS frequencies (see Section 4.2). *Skone & Cannon* [1999] and *Skone* [2001] reported that high convection velocities and large-scale TEC gradients can lead to ionospheric range delay errors during magnetic storms and auroral oval expansion, degrading differential GPS (DGPS) positioning accuracies with errors of 60-80 cm. *Belcher* [2008] also demonstrated that ionospheric irregularities have a limiting effect on the autofocussing ability of space-based synthetic aperture radar (SAR), impacting achievable image resolution.

The levels of navigation accuracy mentioned above are of interest to precise engineering and survey applications, whilst continuity and robustness of service is important for aviation and safety of life applications at high latitudes. There is a need to develop methods that mitigate the impact of scintillation on GPS performance, including robust receiver architectures [e.g. *Humphreys et al.*, 2005], modelling [e.g. *Secan et al.*, 1997; *Strangeways*, 2009] and selective satellite rejection schemes [e.g. *Aquino et al.*, 2009]. The addition of the Galileo satellite programme (completion is projected for 2020) to existing GNSS constellations also holds great potential for the advancement of scintillation monitoring and mitigation.

4.5 Ionospheric tomography using GPS – MIDAS

Ionospheric tomography provides a useful way of observing the global and regional electron content of the ionosphere. The initial idea to image the ionosphere tomographically using radio-to-ground signals was proposed by *K. C. Yeh* [1986] in the Beacon Satellite Symposium of 1986. At this stage the signals used were from the Navy Navigation Satellite System (NNSS) and the ionosphere had already been measured in terms of the Total Electron Content (TEC). The next major step was to invert the TEC to reveal electron density. This idea was developed by several different research groups in the USA (Applied Research Laboratory at The University of Texas), Russia (Moscow State University) and the UK (Aberystwyth University). The first ionospheric tomography performed in Antarctica was by *Heaton, Jones & Kersley* [1996] using two receiving stations and signals from the NNSS. Shortly after this *Mitchell et al.* [1998] imaged the Arctic electron density using NNSS tomography, verified for the first time using the EISCAT radar.

With the deployment of Global Positioning System (GPS) satellites the natural step was then to use that new navigation system for the same task. This brought new challenges because of the more complicated geometry and slower moving satellites. To tackle these issues the University of Bath set out in 1999 to develop a 4D tomographic imaging system called MIDAS (Multi-Instrument Data Analysis Software), the first results from which were presented at the Beacon Satellite Symposium in 2001 by *Spencer & Mitchell* [2001]. These revealed the dramatic enhancements in electron density from the July 2000 storm. This section explains the fundamental MIDAS method and its adaptation for use at high latitudes, to provide context to the images obtained in this research. The MIDAS algorithm is described explicitly by *Mitchell & Spencer* [2003].

Given a data set of slant TEC measurements from GPS ray paths, tomographic imaging presents a convenient way of reconstructing the most likely spatial and temporal conditions in the ionosphere. Essentially, in this case, an algorithm produces a set of refined estimates for unknown variables (electron density and phase ambiguity), based on other known variables (orbit geometry and slant TEC) during the same time period. To create an environment for numerical evaluation, the ionosphere is discretised into a three dimensional grid of volume pixels, or *voxels*.

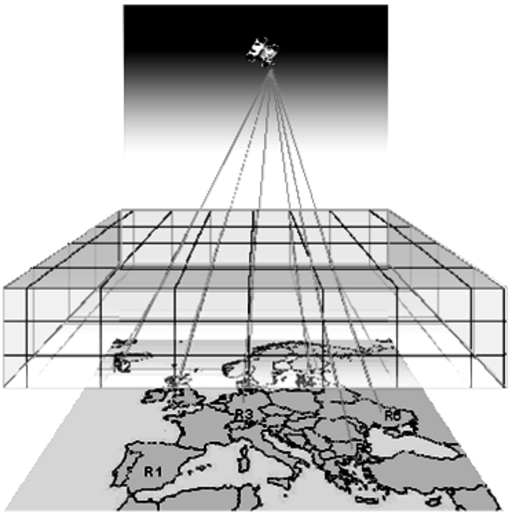

Figure 4.2 – an illustrative example of the three dimensional ionospheric grid required for the tomographic inversion. A single GPS satellite is shown along with typical ray path orientation to multiple ground receivers [image credit: *Robert Meggs*].

The horizontal resolution of the MIDAS reconstruction grid is defined by steps in longitude and latitude, typically ranging from 1-4° depending on data coverage and geographic area. MIDAS is capable of performing global or regional reconstructions. At equatorial latitudes a 1×1° pixel is approximately 110 km^2, but longitude lines converge towards the poles. Northern European or high latitude reconstructions, for example, may require the rotation of an equatorial grid to the area of interest to maintain grid uniformity. The grid's vertical resolution is typically 100-200 km, however the vertical distribution of electron density in MIDAS is controlled by the use of Empirical Orthogonal Functions (EOFs), as explained later in this section. Note that a systematic limitation of MIDAS is that the reconstruction grid does not currently extend to plasmaspheric altitudes, having a maximum altitude of ~2000 km. MIDAS works on the basis that all of the measured GPS slant TEC is accumulated within the reconstruction grid, and so it is likely that an unknown amount of plasmaspheric TEC is redistributed at ionospheric altitudes in the reconstructions. MIDAS is currently being adapted for plasmaspheric tomography using measurements from the NASA Cluster satellites (private communication: Talini Pinto Jayawardena, University of Bath, December 2013).

Slant TEC measurements are made over a defined time window along each satellite-receiver ray path. A pre-processing stage collates both measurements from multiple GPS receivers (if a ground network is being implemented) and GPS ephemeris orbit coordinates:

$$sTEC = \begin{bmatrix} z_1 \\ \vdots \\ z_m \end{bmatrix} = \boldsymbol{z} \tag{4.23}$$

Where m is the number of measurements at a point in time, and for the purposes of this description is equal to the number of satellite-receiver pairs. In practice the number of observations is large and includes values across a time range.

The fundamental model of the forward problem can be expressed as:

$$z_i = \sum_{j=1}^{p} l_{ij} n_j + b_i \qquad i = 1{:}\, m \tag{4.24}$$

Where:

p = total number of grid voxels intersected by ray path

n_j = electron density in j^{th} cell

l_{ij} = length of ray path section in j^{th} cell

b_i = satellite-receiver bias term

A bias value is associated with each satellite-receiver pair, but in practice this is removed by carrier phase and pseudorange differencing over time as explained in section 4.1. The forward problem can then be written in matrix form:

$$\begin{bmatrix} z_1 \\ \vdots \\ z_m \end{bmatrix} = \begin{bmatrix} l_{11} & \cdots & l_{1p} \\ \vdots & & \vdots \\ l_{m1} & \cdots & l_{mp} \end{bmatrix} \begin{bmatrix} n_1 \\ \vdots \\ n_p \end{bmatrix} \tag{4.25}$$

Using matrix and vector notation:

$$\boldsymbol{z} = L\boldsymbol{n} \tag{4.26}$$

Matrix L, the forward operator, is known geometrically through the use of a predefined volumetric grid and observed satellite orbit coordinates. Vector $\boldsymbol{z}$ represents the slant TEC measurements from multiple ray paths. The inversion algorithm is required to find the vector $\boldsymbol{n}$, electron density, which gives the closest mathematical fit to the slant TEC measurements, $\boldsymbol{z}$. To define the inversion problem:

$$L^T\boldsymbol{z} = L^T L\boldsymbol{n} \tag{4.27}$$

$$(L^T L)^{-1} L^T \boldsymbol{z} = \boldsymbol{n} \tag{4.28}$$

This underdetermined problem is difficult to solve, so in implementation several forms of regularisation are used to make it solvable. The first is the addition of a mapping matrix M that transforms the problem into one of unknown basis coefficients $\boldsymbol{x}$ of empirical orthogonal functions (EOF). The EOFs are chosen to describe shape of the altitude profile of ionospheric electron density (based on Chapman profiles), and so provide a level of prior information to the inversion [e.g. *Fremouw et al.*, 1997]. This constrains the problem vertically in space, and the problem becomes:

$$\boldsymbol{z} = LM\boldsymbol{x} \tag{4.29}$$

$$(M^T L^T LM)^{-1} M^T L^T \boldsymbol{z} = \boldsymbol{x} \tag{4.30}$$

The second form of regularisation constrains the problem horizontally. The algorithm's initial estimates of electron density are iteratively refined by least squares minimisation of a regularised cost function, which promotes linear gradients in space and time. The use of a regularisation parameter (λ) allows the user to essentially force a 'smooth' ionospheric reconstruction (by minimising the rate of change of horizontal gradient), or to relax the horizontal conditions in order to better extract finer spatial structuring. This is generally a cautious decision that takes account of geomagnetic conditions and data coverage, as a solution has the potential to become unstable eventually if not constrained i.e. the number of possible solutions becomes large, and the potential for false artefacts increases. The effect of regularisation is demonstrated by Figure 4.3, a series of European MIDAS TEC maps at 1840 UT on 26 September 2011, produced by integrating through three separate reconstructions of electron density with different levels of horizontal regularisation constraint (λ). Column A shows the MIDAS TEC in the frame of the reconstruction grid, with a resolution in this example of 2° latitude by 4° longitude. Column B shows the equivalent smoothed images using interpolation. The top row shows the TEC resulting from a strongly constrained reconstruction (λ = 10.0), which typically renders a smooth ionosphere. The middle row (λ = 1.0) shows the default MIDAS regularisation setting that, with good data coverage, allows a stable reconstruction with good resolution of TEC associated with irregular structuring, such as the area of enhancement over Scandinavia in this example. The bottom row (λ = 0.1) shows the result of a more loosely constrained reconstruction i.e. the regularisation effect is weaker. Although the general form of the TEC enhancement over Scandinavia varies, the structure is consistently present in all three reconstructions and considered to be a real ionospheric feature.

The ground network of GPS receivers in Europe is well populated and spaced, and regional images can reveal storm-time ionospheric structuring such as the mid-latitude depletion trough (also visible around 56° latitude in Figure 4.3) and localised patch enhancements. The TEC maps in Figure 4.3 contributed to the profiling of a geomagnetic storm over Europe on 26 September 2011 [*Baumgardner et al.*, 2013], which is investigated from a polar perspective in Chapter 7.

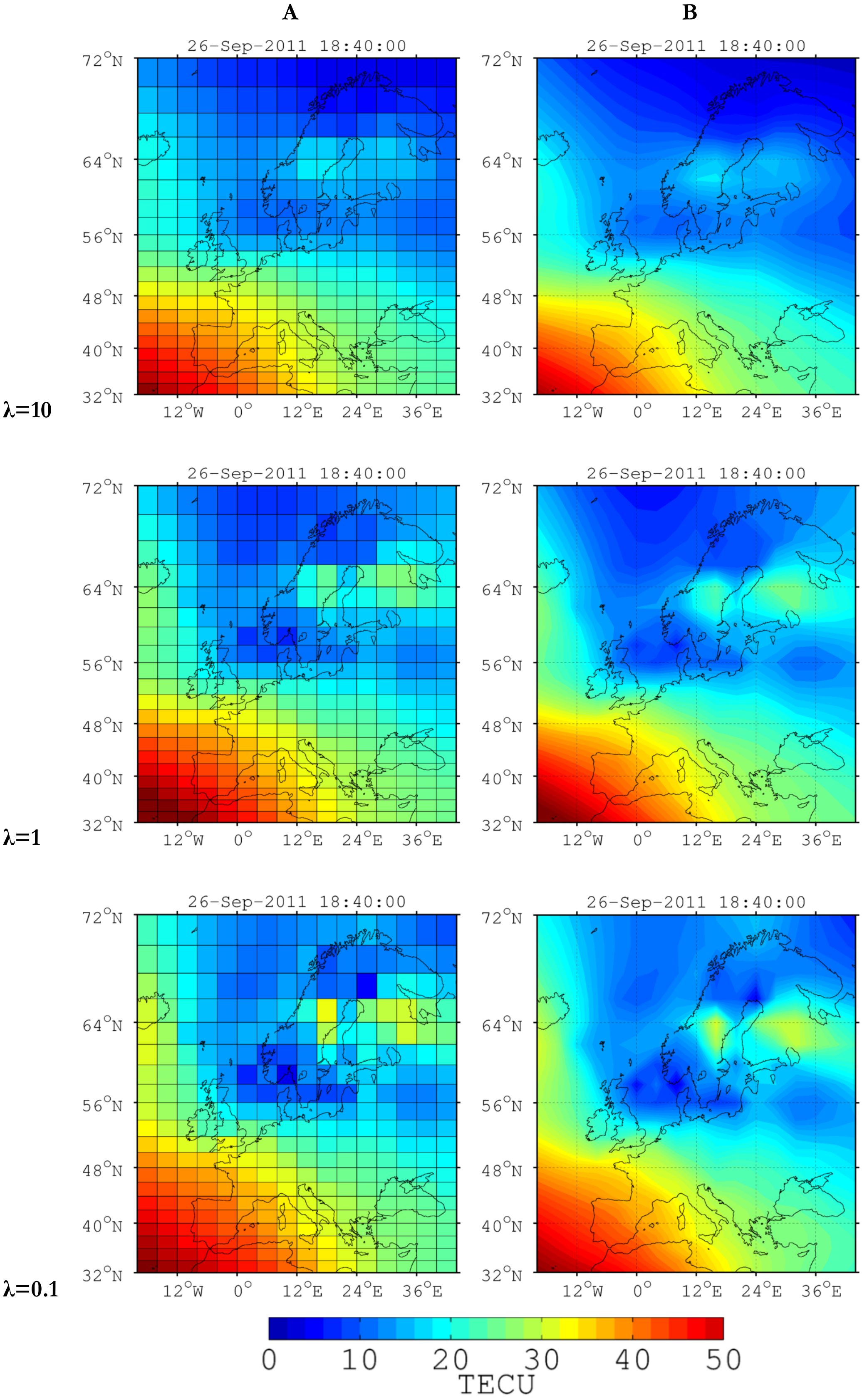

Figure 4.3. A set of European MIDAS TEC maps at 1840 UT on 26 September 2011, demonstrating the effects of image interpolation smoothing (columns A versus B) and relaxing of the horizontal regularisation constraint (three rows of decreasing λ value).

MIDAS is sensitive to several limiting factors at high latitudes. Historically the ground-based receiver distribution has been sparse and uneven, more so in the Antarctic, although this has vastly improved over the last decade. GNSS satellite elevations also get lower towards the poles due to constellation design, so ray path geometry becomes limited. A GPS receiver at the South Pole, for example, will only observe satellites between the horizon and ~43° elevation. Plasma velocities can be very high over the polar cap, which can lead to image blurring. This problem was first addressed by *Spencer & Mitchell* [2007], improving MIDAS ability in this respect by considering prevalent plasma motion in the inversion solution (derived from the Weimer electric field and IGRF magnetic field models). Reconstruction times are also kept short, typically with a 10-20 minute time step. Convergence of longitude lines at the poles dictates the need for a grid rotation from the equator, in order to maintain a more uniform voxel size distribution in the reconstructions. The first specific reconstruction settings adjusted for Antarctica were reported by *Yin et al.* [2009].

4.6 Verification techniques

The primary methods of ionospheric measurement used in this research are tomographic imaging and scintillation monitoring. This section presents the supporting measurement tools used for the purposes of verification throughout the research.

4.6.1 Geomagnetic indices

Large-scale geomagnetic activity may be identified by observing a number of computed indices, which are derived from measurements at magnetic observatories around the globe. The planetary K_p index is based on the three-hourly mean value of disturbance levels in the horizontal magnetic field component measured at 13 mid-latitude stations. These field disturbances reflect magnetic compression and changes in the equatorial ring current (see Figure 2.1), which is largely driven by ion particle population during magnetic storms. In addition to indicating the general severity of a storm (within a range of 0-9) the K_p index is also useful in analysing historical or long term geomagnetic activity, as modern records span several decades and multiple solar cycles. More temporal detail is provided by the magnetic storm D_{st} index ('disturbance field,' nT), which is derived from low-latitude magnetometer measurements that are sensitive to changes in the horizontal component of the geomagnetic field . It is particularly useful for determining the intensity and duration of individual magnetic storms. A prolonged reduction of the horizontal magnetic component at the equator characterises the main phase of a geomagnetic storm, which can last several hours. Subsequent substorm activity can last from hours to a few days.

The A_e (auroral electrojet) index (nT) is similar to the K_p index, but is based on magnetometer measurements from auroral latitudes in the Northern hemisphere. Peaks in A_e index correspond with enhanced flows of the eastward and westward electrojet currents around the auroral oval, typically during periods of auroral activity or geomagnetic storms. The A_e index is a better indicator of substorm activity than the D_{st} index. A_e data is obtained from the Kyoto Centre for Geomagnetism.

In addition to geomagnetic indices, knowledge about the incident solar wind conditions is important for diagnosing geomagnetic storm conditions. Sudden increases in the velocity and particle density of the solar wind indicate a travelling shock front compression, and the orientation of the IMF can determine the extent of its linkage with the magnetosphere upon impact (see Section 2.1). Solar wind and IMF measurements are available from the ACE satellite, which was introduced in Section 2.1. The satellite orbits at the first Lagrangian position between the Sun and the Earth, and makes solar wind measurements with up to 1-second time resolution. These measurements can be projected forwards in time to the magnetopause, either by simple time delay (see Chapter 5) or by correlation with Earth-orbiting satellites such as Geostationary Operational Environmental Satellite (GOES) and WIND. ACE data is available from the ACE Science Centre and the OMNIWeb service.

4.6.2 Incoherent Scatter Radar

An ISR transmits a radio wave signal and receives a scatter signature some time later. They operate within a much higher frequency range than ionosondes, typically from 50 MHz to over 1000 MHz, therefore well above the typical reflection frequencies (i.e. above the plasma frequencies) of the ionosphere. An ISR transmission passes through the ionosphere almost entirely, but information comes from the small amounts of energy scattered by ionospheric electrons at different altitudes. The result is a complete ionospheric altitude profile, without the reflection limitations of ionosonde sounding from the ground or topside. Information is provided above the F region peak, and the scans are able to resolve the F region even in the presence of a dense E layer. An ISR does, however, require a large antenna footprint and high power transmissions to achieve this detail in electron density resolution, and so the radar sites are limited in number globally (~15 in 2009 [*Kelley*, 2009]).

4.6.3 DMSP SSJ/4 Particle Spectrometer

The Defense Meteorological Satellite Program (DMSP) satellites are in sun-synchronous, low Earth polar orbits of period 101 minutes and nominal altitude of 830 km. Each crossing of the polar cap and auroral oval takes approximately 10-15 minutes. Four DMSP satellites (F15-F18) are currently flying with the SSJ/4 precipitating electron and ion spectrometer instrument.

The SSJ/4 spectrometer was designed to measure the flux of charged particles as they enter the Earth's atmosphere from the magnetosphere. A multi-channel particle detector looks towards the satellite zenith, discriminating ions and electrons within an energy range of 30 eV to 30 keV. Resulting spectrograms show the energy and flux of particles travelling into the high latitude ionosphere. Each satellite pass essentially indicates a broad morphology of the high latitude energy input in cross section, with the auroral oval thickness and boundary locations discernible in most cases. Polar cap precipitation and arcs can also be identified at times. DMSP SSJ/4 data have been used in this work as a source of in situ verification of high latitude ionospheric structure and presence of precipitation. An excellent commentary by *Newell et. al.* [2009] provides detail on the correct interpretation of these spectrograms.

4.6.4 South Pole All-Sky Imager

The ASI is located on the roof of the Amundsen-Scott South Pole Station, in close proximity to the true geographic South Pole; or 74.3° Corrected Geomagnetic Latitude (CGLAT) [*Tanaka et al.*, 2012]. The camera provides a temporal and spatial measure of optical auroral emission intensities within the central Antarctic plateau during the dark winter months [*Ebihara et al.*, 2007; *Ejiri et al.*, 1999]. The optics consists of a *Nikkor* F1.4 aperture, 180° field-of-view (FOV) 'fish-eye' lens, projecting a wide-angle image on to a CCD sensor of resolution 512 × 512 pixels. A rotating filter mechanism allows the capture of a range of images at discrete optical wavelength emissions, including atomic oxygen ([OI] 557.7 nm green line and [OI] 630.0 nm red line). Image exposure time is typically four seconds for both 557.7 nm and 630.0 nm emission intensities; images are recorded with a capture interval of ~24 seconds (image capture of different emission wavelengths is interleaved in time as the filter mechanism rotates across the lens element). The intensity saturation point of the camera sensor for 557.7 nm emissions is ~44000 Rayleigh; the Rayleigh (R) is a photometric unit and is a measure of the rate of emission intensity or spectral radiance of spatially extended light-emitting sources [*Baker*, 1974]. Conversely, the sensitivity of the imager to low intensity emissions is dependent on instrument noise. The deviation of noise for the South Pole imager is +/- 50 counts around the pixel value, corresponding to ~96 Rayleigh at 630.0 nm, for a four second exposure. Taking the typical brightness of a low intensity emission such as airglow as 300 Rayleigh [*Hosokawa et al.*, 2010], an image capture would have a signal-to-noise ratio (SNR) of approximately three. The detection of airglow would require dedicated longer exposures of more than 12 seconds, increasing the SNR to over ten. Some systematic corrections are applied to the 'raw' images [*Kubota et al.*, 2001], including lens distortion correction, brightness uniformity adjustment and compensation for atmospheric extinction and the Van Rhijn effect; the characteristic increase of observed emission intensity with increase in zenith angle towards the horizon [*Chamberlain*, 1961].

4.7 Summary

This chapter has described the use of the GPS as a tool for ionospheric imaging and scintillation monitoring. Fundamental ionospheric propagation and scintillation theories were given firstly for context. Scintillation is caused by a complex mix of multi-scale processes associated with ionospheric irregularities, with phase scintillation prevalent at high latitudes. Scintillation measurement methodology was then shown, including receiver hardware and data treatment considerations. The detrimental effects of scintillation on GPS performance were briefly outlined, highlighting the need for the development of mitigation schemes. Finally, MIDAS was described in its capacity for tomographic imaging of the ionosphere. MIDAS is sensitive to several limitations at high latitudes, but expansion of ground receiver network coverage in the Arctic and Antarctica over the last decade has increased the potential for resolving structures that are associated with scintillation. Chapter 5 investigates the combination of scintillation monitoring and ionospheric imaging in Antarctica.

5 Antarctic imaging

In this chapter the effect over Antarctica of the ionospheric storm of 5-6 April 2010 is investigated. The aim of this work is to assess the ionosphere's large-scale response in the Southern hemisphere to the impact of a coronal mass ejection event, and identify any structuring that can be linked with the causes of GPS scintillation activity. This study combines GPS tomographic images and scintillation measurements for the first time in Antarctica. Section 5.1 provides the aims of the experiment in the context of previous strategy in the Arctic. Section 5.2 builds on the content of Chapter 4 with some specifics about the instruments and methods used in this experiment. Section 5.3 presents observations and image analysis, followed by an interpretation of the scintillation mechanisms present during the storm in Section 5.4. Finally a summary of the work is given in Section 5.5

The results presented in this chapter are published in the *Journal of Geophysical Research* [*Kinrade et al.*, 2012].

5.1 Introduction

The causes of GPS scintillation at high latitudes are attributed to the presence of ionospheric irregularities and large-scale gradients in electron density. The mechanisms causing particular scintillation events are, however, difficult to trace. Moreover quantifying them and developing a confidence about the exact cause of an event is still quite rare, particularly in Antarctica. GPS tomographic imaging, described in Section 4.5, has been used at high latitudes for over a decade now, as it can provide useful estimates of electron density in regions inherently sparse in wide-area observations. Tomography cannot directly provide the spatial resolution required to see the small-scale structures responsible for GPS scintillation. The images that tomography provide, however, have been used successfully in the Arctic to identify instances of ionospheric storm features and scintillation activity that are matched spatially and temporally (see Section 3.1). This study aims to build on this strategy by combining tomographic images with measurements from a new network of dedicated scintillation receivers in Antarctica.

5.2 Instruments & methods

In January 2010 a total of seven GPS scintillation receivers were deployed across the central plateau of the Antarctic continent at latitudes within the auroral zones and polar cap. The modified Novatel GSV4004 GPS receivers track up to 11 satellites simultaneously at L1 (1575.42 MHz) and L2 (1227.60 MHz) frequencies, measuring phase and amplitude changes at a sample rate of 50 Hz. L1 amplitude and phase scintillation measurements are recorded in the form of the computed indices S_4 and σ_φ respectively [*Van Dierendock*, 1999]. A description of scintillation data and their pre-processing is provided in Section 4.3.

Vertical TEC maps are produced by integrating through electron density images produced by MIDAS, the tomographic imaging tool described in Section 4.5. In 2010 a total of 50 ground-based GPS receivers were providing dual frequency measurements, available from the PoleNet and IGS (International GNSS Service) databases through the UNAVCO facility [online]. Figure 5.1a shows the distribution of GPS ground receivers that contributed the data used in this study; some site name labels have been omitted for clarity due to the close proximity of several sites. Figure 5.1b shows (for an example) the observed GPS ray path coverage during 5 April 2010 1600-1700 UTC, projected on to the ionosphere at an altitude of 350 km.

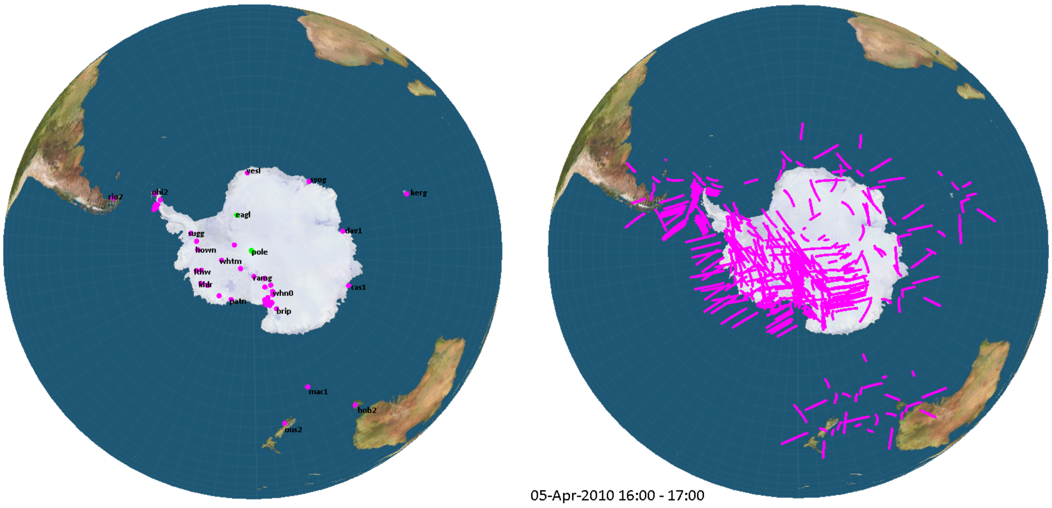

Figure 5.1 (a, b): The geographic distribution of GPS ground receiver sites used in this study (5.1a) and an indication of observed GPS ray path coverage above 20° horizon elevation within a typical one hour period, projected on to the ionosphere at 350 km altitude (5.1b). Note that the ray path coverage is concentrated within the western and central continent, and sparse over the oceans and north-eastern continent. The two scintillation receiver locations of interest here are shown in green, at the geographic South Pole and remote site 'Eagle' (81°S 22°W).

The ionospheric electron density was reconstructed on a three-dimensional grid of resolution 4° in latitude, 4° in longitude and 40 km in altitude. The grid was formed around the equator prior to being transformed to the high-latitudes using a rotation matrix, hence mitigating the problems that would be associated with longitudinal convergence towards the geographic pole in the un-rotated case. The radial distribution of the ionosphere is defined as a mathematically modelled set of empirical orthogonal functions (EOF), thus reducing the number of unknown variables in the inversion problem to a set of basis function coefficients [*Fremouw et al.*, 1997] (see Section 4.5). Electron density images were produced with 10-minute GPS data samples in this study.

Magnetic observations are presented from a number of instruments. IMF observations were obtained from the Advanced Composition Explorer (ACE) satellite monitoring solar wind, magnetic field and energetic particle activity at the first Lagrangian orbit position. Planetary 3-hourly K_p indices are used to indicate a general level of global geomagnetic disturbance, and were obtained from the Space Physics Interactive Data Resource (SPIDR). Provisional A_e (auroral electrojet) indices provide an indication of auroral magnetic activity, and were obtained from the World Data Centre for

Geomagnetism, Kyoto. Background information on geomagnetic indices can be found in Section 4.6.1.

Energetic electron and proton particle data were obtained from the Defense Meteorological Satellites Program (DMSP) and Polar Operational Environmental Satellite (POES), a series of polar orbiting weather satellites at orbital altitudes of ~830-870 km. Electron and ion spectrometer plots are used here to identify auroral and polar cap precipitation that could cause irregular electron density structuring and hence scintillation.

GPS data taken from the CHAMP (Challenging Mini-satellite Payload) and GRACE (Gravity Recovery and Climate Experiment) polar orbiting satellites were used to produce track projections of vertical TEC to verify the presence of large-scale plasma gradients revealed through the inversion tomography.

5.3 Observations & analysis

5.3.1 IMF & geomagnetic activity

The period of geomagnetic disturbance during the 5 and 6 April 2010 was the focus of the study. A detailed account of the IMF conditions during this storm is provided by *Möstl et al.* [2010]. Figure 5.2 depicts a number of geomagnetic indicators within the period 5-7 April 2010. Figure 5.2a shows the variation of three-hourly K_p index that reached a peak value of 8- between 0900-1200 UT (Universal Time) on 5 April 2010. Figure 5.2b shows provisional levels of A_e index that reached a peak value of 2291 nT at 0920 UT on 5 April 2010. Figures 5.2c, 5.2d and 5.2e present measurements from the ACE satellite; Figures 5.2c and 5.2d show the orientation of the IMF components B_y and B_z respectively over the duration of the disturbance, and Figure 5.2e is a record of solar wind velocity.

From Figures 5.2c, 5.2d and 5.2e it can be seen that a period of both fluctuation in the IMF and acceleration of solar wind velocity occurred on 5 April 2010. A shear in the solar wind speed at ~0750 UT is strong indication of a travelling shock front, with the V_x velocity component rising sharply from ~500 kms^{-1} to values above 700 kms^{-1} in ~30 minutes. A maximum velocity of 816 kms^{-1} was recorded at ~1357 UT, after which the wind speed remained high (> 600 kms^{-1}) and gradually decelerated into the next day.

The IMF was subject to sudden disturbance at ~0755 UT, coincident with the solar wind velocity shear. The B_z and B_y components fluctuated strongly within the period ~0755-1055 UT, switching orientation between negative and positive in the range -18 nT to +15 nT. A period of sustained positive B_z then occurred from ~1055 UT, with values reaching up to +21 nT. The main signature of the disturbance occurred at ~1200 UT, with the B_z and B_y components rapidly switching polarity within a few minutes. The B_y value fell significantly from +9 nT to -22 nT, and remained negative for over nine hours. The B_z value dropped from +21 nT to -2 nT, before settling into a prolonged undulating period between weakly negative and positive levels over the following 12 hours. Note that IMF conditions recorded at the ACE satellite position propagated to the magnetopause approximately 40 minutes later in time (ACE projection based on distance and solar wind velocity). A sudden peak signature in the A_e index at ~0920 UT suggests that the auroral geomagnetic field responded to the shock front a little later in time; however the A_e index is based solely on Arctic magnetic observations and therefore may not be representative of the Southern high latitudes.

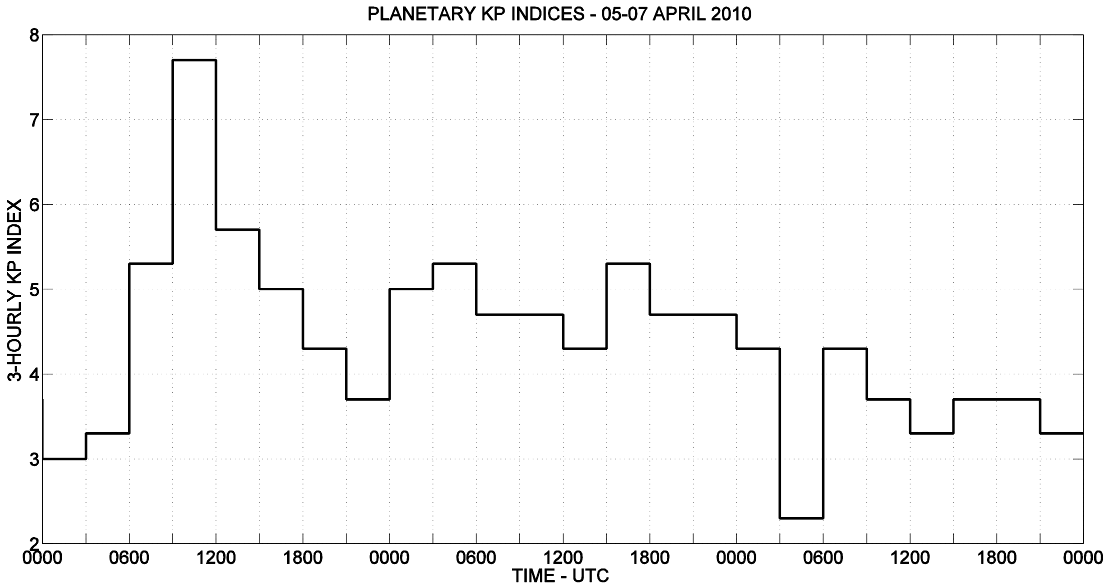

PLANETARY KP INDICES - 05-07 APRIL 2010

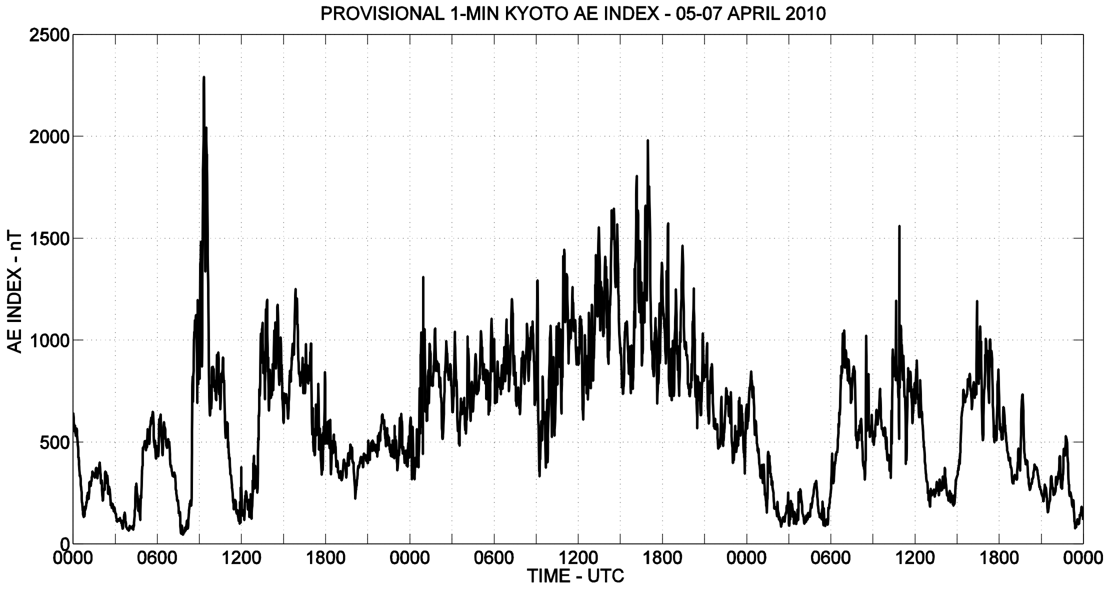

PROVISIONAL 1-MIN KYOTO AE INDEX - 05-07 APRIL 2010

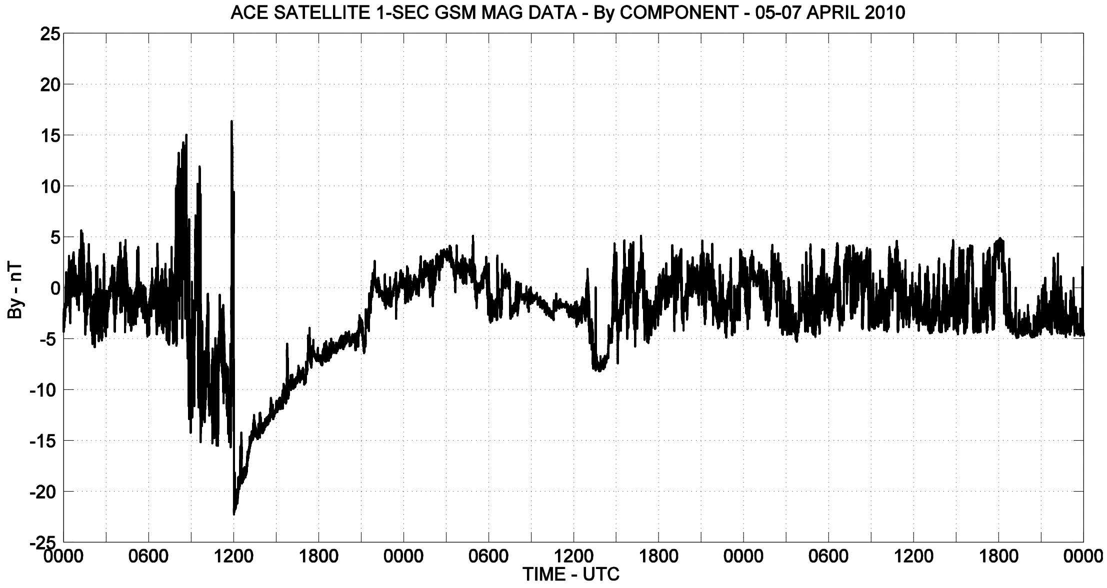

ACE SATELLITE 1-SEC GSM MAG DATA - By COMPONENT - 05-07 APRIL 2010

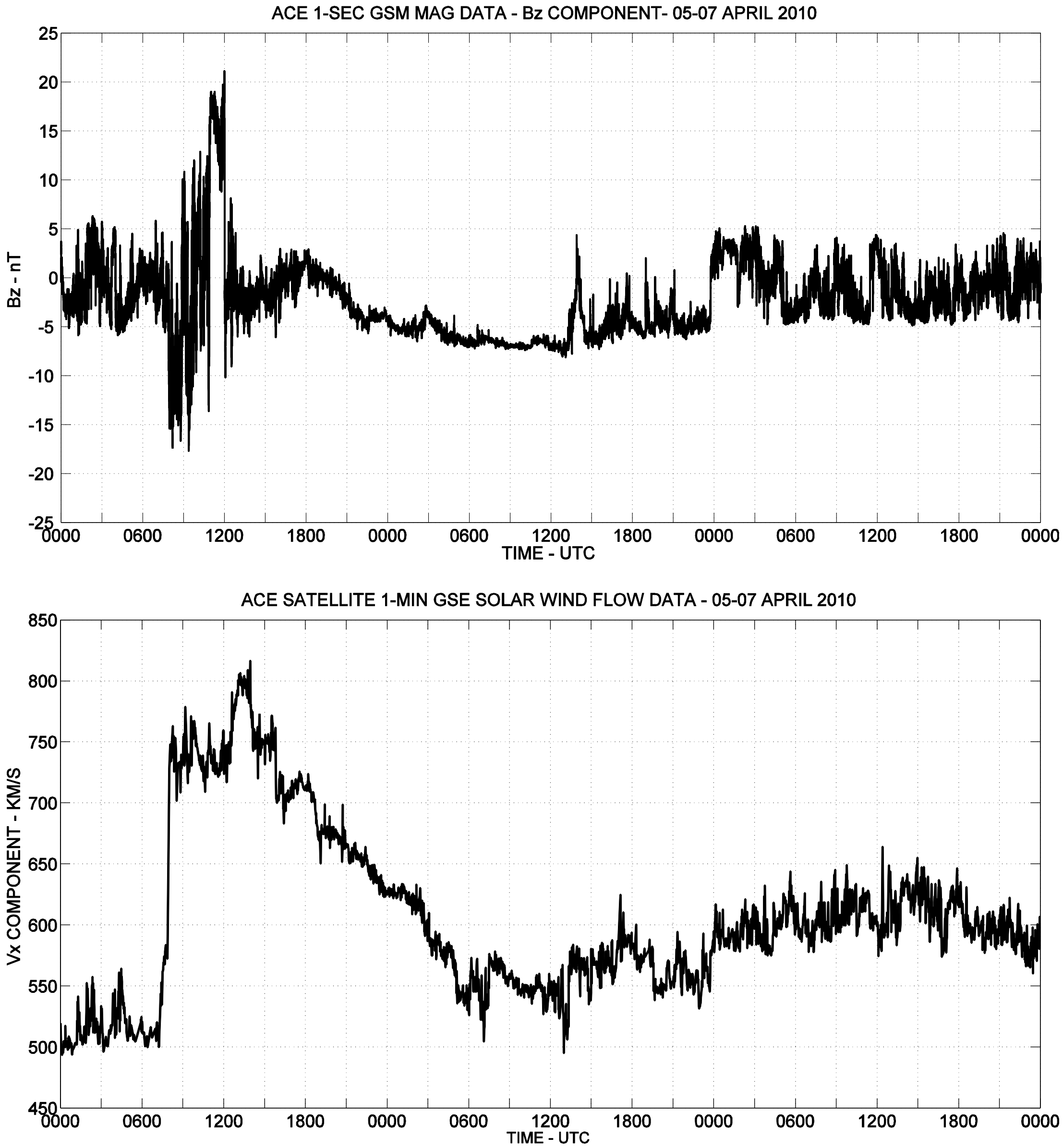

Figure 5.2 (a-e): Geomagnetic indicators and IMF measurements during the period 5-7 April 2010. The variation of magnetic activity indices K_p (5.2a) and A_e (5.2b) show the geomagnetic storm and sub-storm phases during days 5-7. The IMF components at the ACE satellite position (geocentric solar magnetospheric [GSM] plane) are perturbed, with signatures visible in both B_y (5.2c) and B_z (5.2d). A record of solar wind velocity at the ACE satellite position (geocentric solar ecliptic [GSE] plane) (5.2e) reveals a travelling shock front at ~0750 UT on 5 April 2010.

5.3.2 Phase scintillation

Scintillation data were analysed for the period of geomagnetic disturbance. Figures 5.3a and 5.3b present a two-day record of the 1-minute scintillation indices from the receiver located at the geographic South Pole (~74°S corrected geomagnetic [CGM] latitude), and site Eagle (81°S 22°W, ~67°S CGM latitude). An extended period of elevated σ_φ index was prominent between ~0830-1830 UT on 5 April 2010. It is interesting to note the short time of just over 40 minutes between the event at the ACE satellite and the onset of scintillations, indicating that the scintillation closely followed the arrival of the event at the magnetopause. Phase scintillation indices reached values of up to 0.55, indicating only moderate signal phase variation; however it is interesting to note that the majority of observed satellites were subject to scintillation over a period spanning ten hours. There is little evidence of associated amplitude scintillation during this time, with only a slight rise in the S_4 index base level notable between ~1000-1400 UT. This predominance of phase rather than amplitude scintillation would indicate larger-scale (above the Fresnel scale of one to a few hundred metres at GPS signal frequencies) structures being responsible for most of the scintillation (see Section 4.2).

Each image in Figure 5.4 shows an hourly representation of vertical TEC over Antarctica during 5 April 2010, overlaid with 350 km intercepts of L1 phase scintillation indices from two GPS receivers – one at the geographic South Pole and the other at site Eagle (81°S 22°W). The time indicates the centre of the imaging window used to produce the vertical TEC reconstructions, while scintillation points are overlaid from within the hour shown e.g. the 1630 UT image represents a TEC reconstruction overlaid with scintillation recordings from 1600-1700 UT. The series of TEC images, colour-mapped in units of 1 TECU = 10^{16} el/m^2, shows the formation of a TEC 'patch' structure over the Western Antarctic. Interestingly, the structure's initial formation is relatively coincident with the switch of the IMF B_z and B_y at 1200 UT, seen in the 1230 UT image. The plasma structure is well formed over the 'western' Antarctic by 1630 UT but there is a dip in the density in a region associated with moderate scintillation. This region is interesting because it lies in the region of sunlit plasma and for some reason, there is a decrease in density over a localised area, and then further inside the convection region there is an increase in TEC.

During the hour beginning 1700 UT the structure then separates from the original body of plasma (-30°E, -72°N), displaying estimated TEC levels of up to ~20 TECU (-90°E, -81°N). A defined plasma gradient lies approximately along the solar terminator line, from -180°E to -30°E longitude. It is possible that this enhancement is sustained by its prolonged period in the sunlight. By 1830 UT the mid-latitude plasma has receded away from the Antarctic, and the separate structure has started to drift westwards and dissipate. The 1930 UT image suggests that the ionosphere has almost returned to a quiet, smooth state across most of the continent.

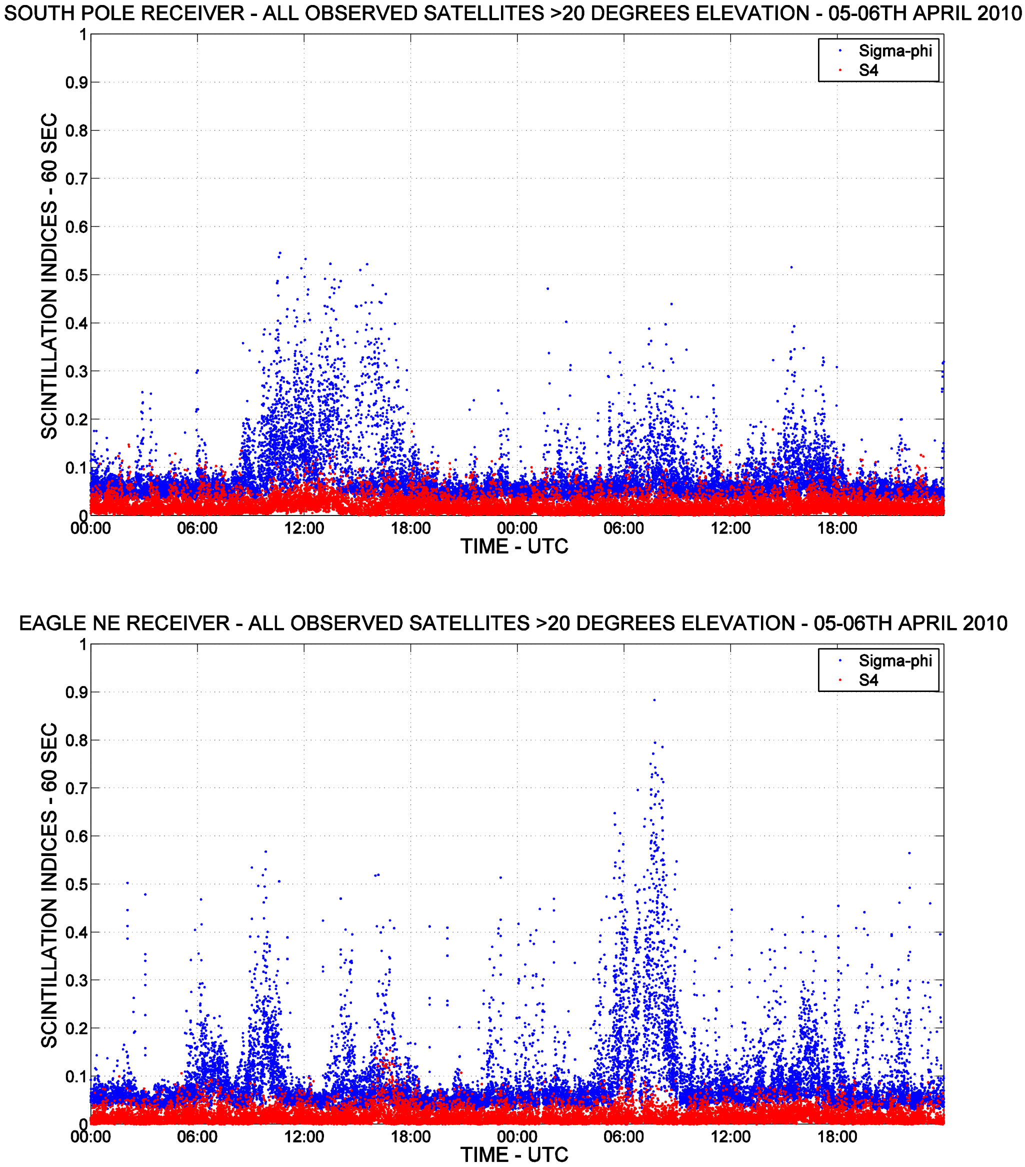

Figure 5.3 (a, b): Amplitude and phase scintillation indices during 5-6 April 2010 at (5.3a) South Pole and (5.3b) site Eagle. Note the almost immediate onset of phase scintillation with the CME shock front, particularly at South Pole. The lack of significant amplitude scintillation indicates that the ionospheric irregularities present are of sizes larger than the first Fresnel radius of one to a few hundred meters at GPS frequencies.

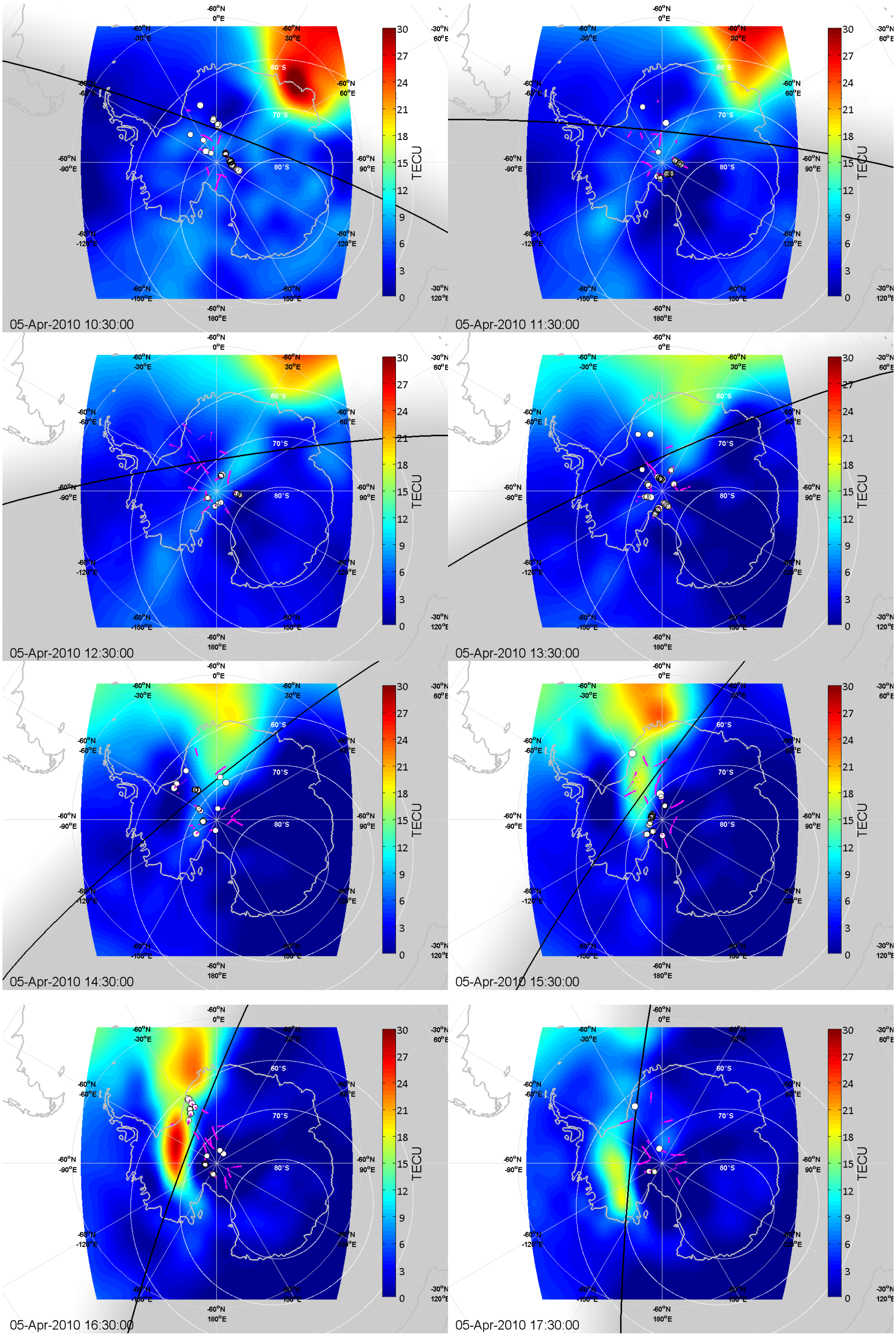
05-Apr-2010 10:30:00
05-Apr-2010 11:30:00
05-Apr-2010 12:30:00
05-Apr-2010 13:30:00
05-Apr-2010 14:30:00
05-Apr-2010 15:30:00
05-Apr-2010 16:30:00
05-Apr-2010 17:30:00
TECU
0
3
6
9
12
15
18
21
24
27
30
60°S
70°S
80°S
-60°N 0°E
-60°N 180°E
-60°N -90°E
-60°N 90°E

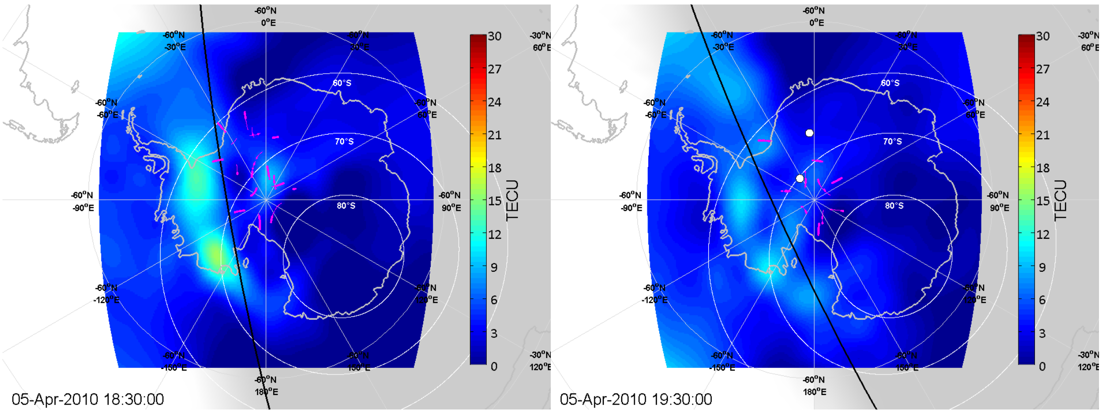

Figure 5.4: Combined GPS vertical TEC images and GPS L1 phase scintillation occurrence as observed from receivers at the geographic South Pole and site Eagle (81°S 22°W) on 5 April 2010. Sun orientation is indicated by the solar terminator (black line, ground level) and nightside shading. Greenwich meridian longitude is the central vertical line in each image. Approximate geomagnetic field lines are centred on the 2005 altitude-adjusted corrected geomagnetic [AACGM] pole. Phase scintillation indices are plotted in area-scaled magenta points for each observed satellite within the hour of observation, at a sub-ionospheric ray path pierce height of 250 km along the satellite track. Points having values greater than or equal to 0.3 are plotted as area-scaled white 'bubbles' to emphasize stronger phase scintillation occurrence [elevation cut-off 20°, lock-time > 240 seconds]. The sequence of TEC reconstructions shows the formation and lifetime of a plasma enhancement patch in the local dawn-midday sector, which breaks off the dayside plasma and drifts southward before dissipating. Phase scintillation appears coincident only in a temporal sense, with the exception of a possible spatial correlation at the break-off point in the 1630 UT image.

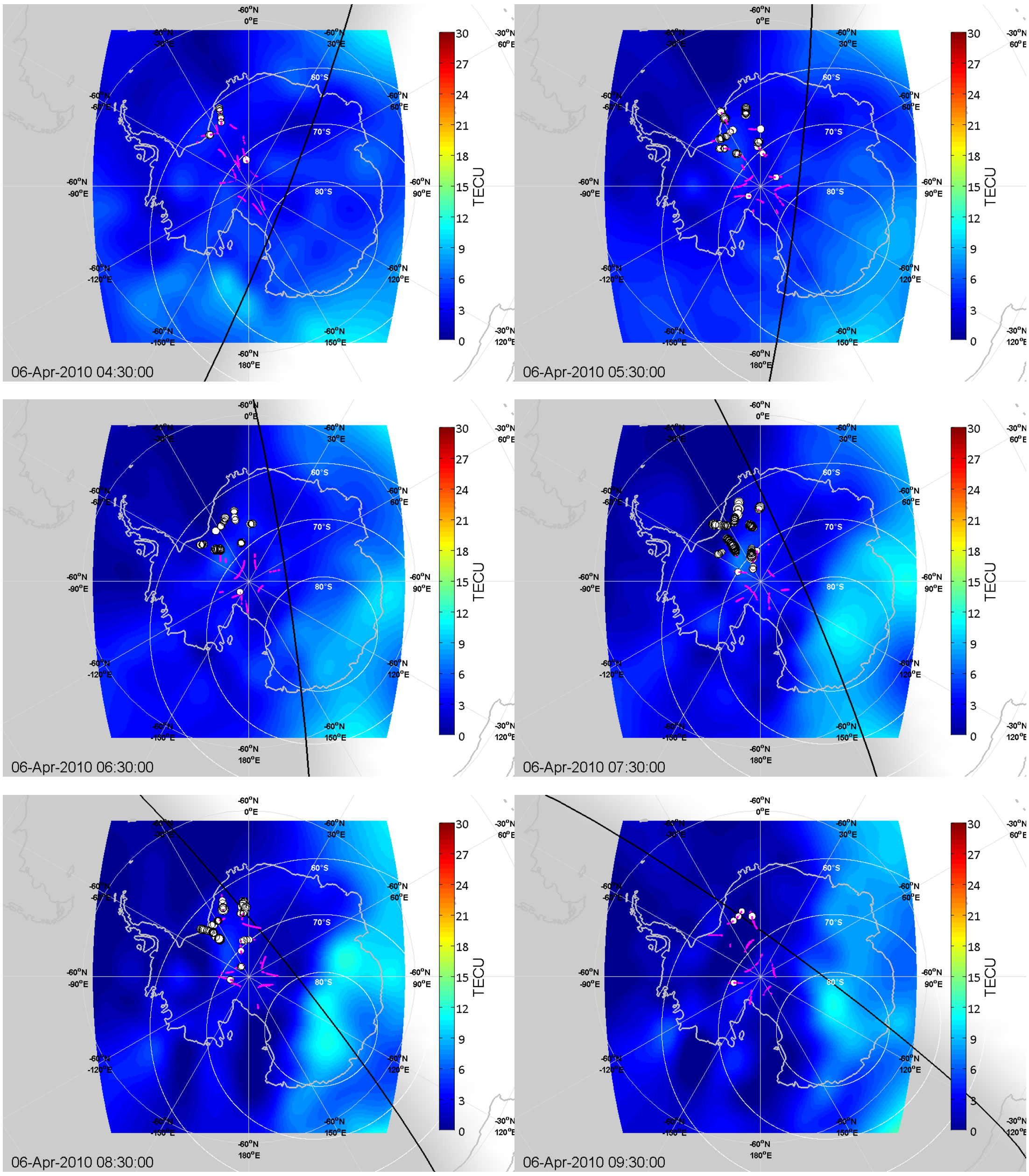

Figure 5.5: A time series of ionospheric TEC images during 6 April 2010, overlaid with phase scintillation index variation from GPS receivers at the geographic South Pole and site Eagle. The TEC images suggest a relatively smooth ionosphere, absent of any large-scale plasma gradients. During the same time period, scintillation receivers at South Pole and site Eagle recorded moderate phase scintillation ($\sigma_\varphi > 0.3$) on the majority of observed satellites within the dusk-midnight sector.

K_p remained high on 6 April 2010, when it is likely that the magnetosphere was still being influenced by the interplanetary magnetic cloud following the shock front on 5 April 2010. The phase scintillation indices recorded at South Pole (Figure 5.3a) and site Eagle (Figure 5.3b) suggest this also, with ‘burst’ periods occurring across all observed satellites throughout 6 April 2010. The TEC image sequence of Figure 5.5 suggests relatively quiet plasma conditions, and there is no evidence of any polar cap or auroral structuring. Interestingly this implies that, in this instance and based on the GPS tomography results, the phase scintillation indices were not associated temporally or spatially with any TEC gradients of plasma structuring. In fact the scintillation region of the ionosphere was in darkness during this period.

5.4 Discussion

The presence of ionospheric scintillation at high-latitudes is typically attributed to some form of irregular plasma structuring, and subsequent signal refraction and diffraction. In this section cases are presented for the presence of both energetic particle precipitation and large-scale plasma structures as catalysts for the observed GPS phase scintillation during the period of study.

5.4.1 Particle precipitation

Attention is focused on two periods of interest. The first period was the ~1630 UT time period on 5 April 2010 (see Figure 5.4). During this period, South Pole and site Eagle (81°S W22°) were both in the magnetic local noon sector at ~(1230, 1310) MLT respectively, while South Pole was at ~74°S corrected geomagnetic (CGM) latitude and Eagle was at ~67°S CGM latitude. Both the South Pole GPS receiver and the Eagle GPS receiver showed significant scintillations, but in two significantly different magnetic latitude sectors; South Pole would typically have been considered to be in the dayside cusp region while Eagle would have been in the dayside auroral zone, although magnetic storm conditions can alter the cusp and auroral boundaries. The second period of interest was the ~0730 UT period on 6 April 2010 (Figure 5.5). Again, both stations showed significant scintillations. However, they were then in the magnetic local midnight sector, and there was very little large-scale structuring at all. Thus, it appears that the observations indicate three distinctly separate scintillation events, with differing geophysical conditions.

The first event was the 1630 UT period for the South Pole scintillations. These scintillations were located near the dayside cusp. Over the one-hour period from 1600 to 1700 UT, four separate satellites observed scintillations, with three satellites observing two separate periods of scintillations over the one-hour period. Of the total seven scintillation periods, five of them exhibited very similar properties. Each scintillation event consisted of a short 'burst' of phase fluctuations that lasted ~30 seconds. Within the 30-second burst there were several pseudo-periodic oscillations that lasted ~5-6 seconds. Each of the scintillation bursts was located in local magnetic time near 13 MLT, and at magnetic latitude of 73-74°S. In addition, the amplitude of each of the scintillation events varied by 3-4 dB over the 30 second period, indicating that the source was likely diffractive in nature. These similar characteristics indicate a single source of the scintillations located near 13 MLT, 73-74°S latitude and extending in time for at least 30 minutes. It seems likely this source region was due to cusp precipitation of some kind. However, without correlative data this must remain only a plausible supposition. Figure 5.6 presents a representative example over a 200 second period for one of the 30-second burst events for PRN 4. The phase scintillations have been filtered with a 6th order Butterworth filter (with 0.1 Hz cut-off frequency, see Section 4.3). The short burst of scintillations is similar for all five events.

The second event was the 1630 UT period for the Eagle scintillations. These scintillations were located in or near an electron density depletion region at ~70°S geographic latitude and ~330°W longitude. This depletion region appeared at the 'break-off' point of the plasma enhancement, between the solar-produced dayside plasma and the resulting patch-like body of enhancement that drifted southward. There are three interesting questions regarding this event. Firstly, what was the cause of a density depletion region, at local noon, which was in a sunlit region? Secondly, what was the cause of the phase scintillations and thirdly were the physical causes of the density depletions and scintillations linked? To help in answering these questions, Figure 5.7 presents a pass of DMSP 17 over Antarctica from 1610-1615 UT. The third panel down presents the electron energy and energy flux along the pass, while the fourth panel presents the ion energy and energy flux. Unfortunately, this pass was in the ~1600 MLT sector rather than the 1300 MLT sector of the observations. However, it is at least possible that the precipitation observed by DMSP in this sector was similar to precipitation events at ~0300 MLT away, considering the same magnetic latitude regions. Focussing on the elevated 'red' electron precipitation from the time 1612 UT for ~35 seconds, energies of > 1 keV and large energy fluxes were present. This would imply fairly 'hard' E-region precipitation. In addition, the proton precipitation in the same time period showed 1-10 keV energies also in the E-region. During this period the magnetic latitudes were ~70-68°S, which is very similar to the Eagle magnetic latitudes. Particle data from the POES N18 satellite also showed strong electron precipitation and some proton precipitation in the ~1400 MLT sector (geographic longitude 344.7°, latitude 69.9°S at ~1638 UT), lending further support to the suggestion of precipitation energy spread over the entire post-noon sector. Thus it seems likely that the Eagle phase scintillations manifested as a result of mixed plasma structuring; kilometer scale (or larger) E-region precipitation irregularities, and large-scale plasma density gradients associated with the enhancement structure break-off. However, there was also significant < 1 keV soft electron precipitation especially at ~1612 UT. This was probably F-region precipitation, and was located at similar geomagnetic latitudes to the large density depletion observed in Figure 5.4. It is possible that the F-region precipitation had elevated the electron and ion temperatures, which would lead to enhanced recombination of O^+, and thus reduced electron densities [e.g. *Brinton et al.*, 1978]. *Valladares et al.* [1994] show evidence for this mechanism causing multiple TOI break-off events in the northern high latitudes.

The third event of interest was on 6 April 2010, from 0600-0800 UT, and is represented in Figure 5.5 above. Here there was significant phase scintillation on a number of different satellites from both Eagle and South Pole. During this period, the ionosphere was unstructured in the region of scintillations and had low overall TEC values. Figure 5.8 presents a DMSP F18 pass from 0630-0640 UT. The pass trajectory went right through the region of the scintillation observations, particularly the period from 0633-0637 UT. During this period there were very high energies of electron precipitation (> 10 keV), with high-energy flux, that extended across the region from ~350° to 293° geographic longitude, and from ~74°S to 80.4°S latitude. This suggests hard auroral precipitation directly causing kilometer scale irregularities, which produced the observed phase scintillations. There was also a narrowly confined region of high energy proton precipitation located at approximately 315° longitude and 80°S latitude that appears to correlate well with some of the larger scintillations presented in Figure 5.5 for the 0630 UT and 0730 UT panels.

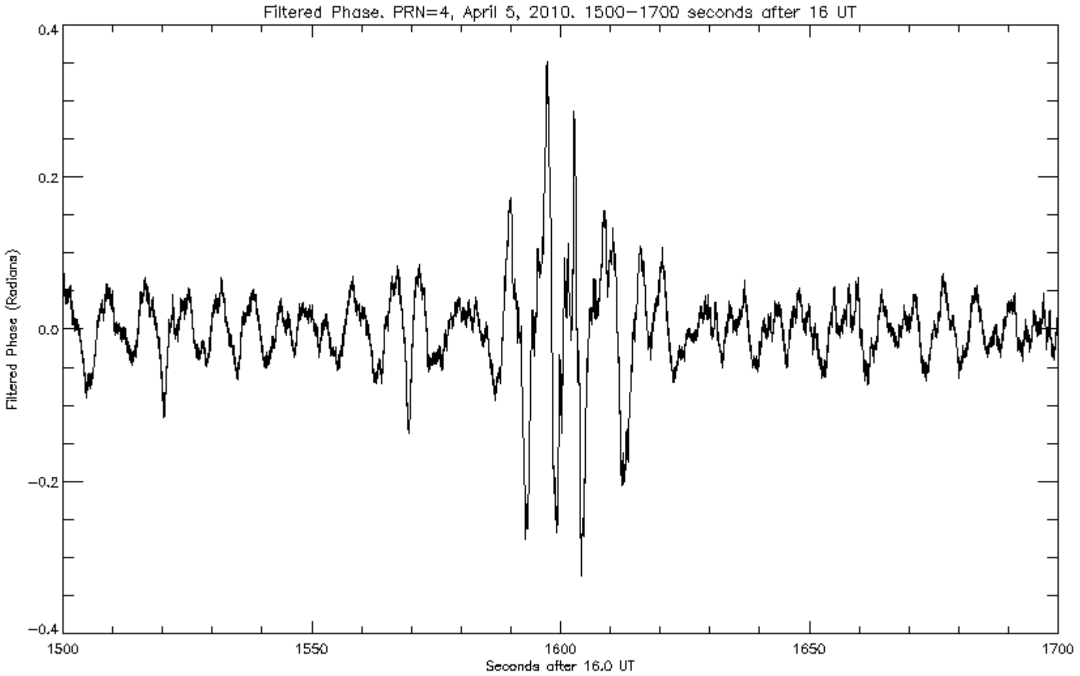

Figure 5.6: High data rate phase scintillations from PRN 4 recorded at South Pole during 1500-1700 seconds after 1600 UT on 5 April 2010. A 30 second 'burst' period included several pseudo-periodic oscillations that lasted ~5-6 seconds. Similar signatures from other satellites during the same period suggest a source of signal diffraction fixed in magnetic local time for ~30 minutes, likely due to cusp precipitation.

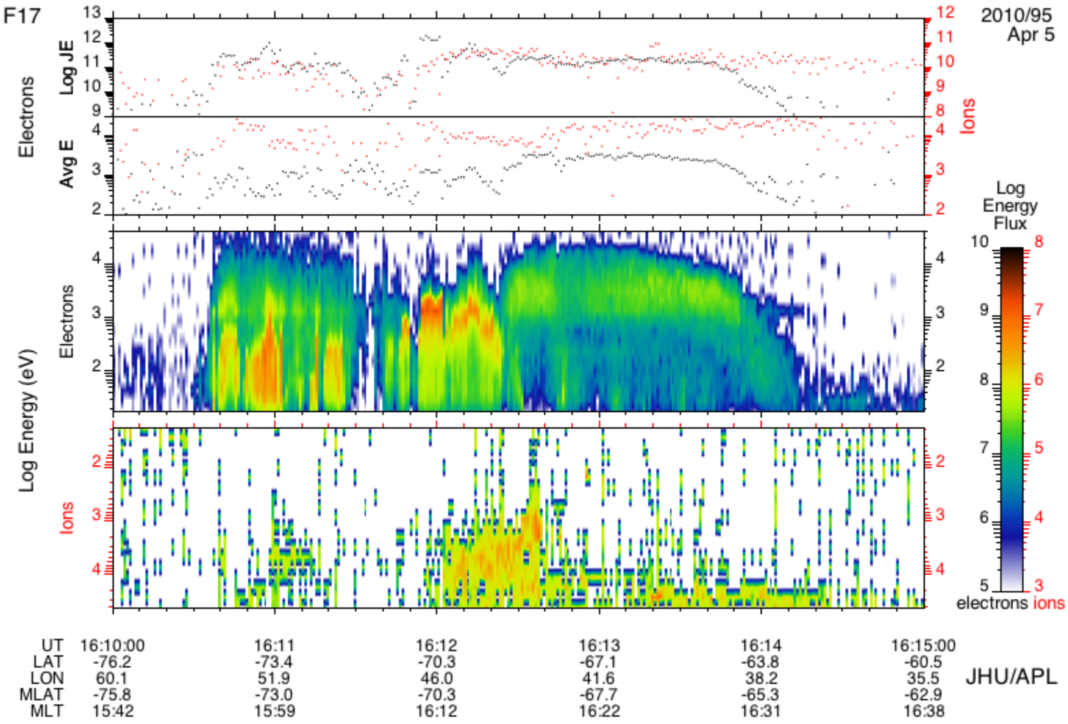

Figure 5.7: A particle spectrometer record from DMSP satellite F17 during 1610-1615 UT 5 April 2010. Labelled longitudes are Eastern. Electron energies of >1 keV and proton energies of 1-10 keV, and elevated energy flux levels, indicate a period of hard E-region precipitation within a few sectors of MLT from the plasma enhancement ‘patch’ break-off point.

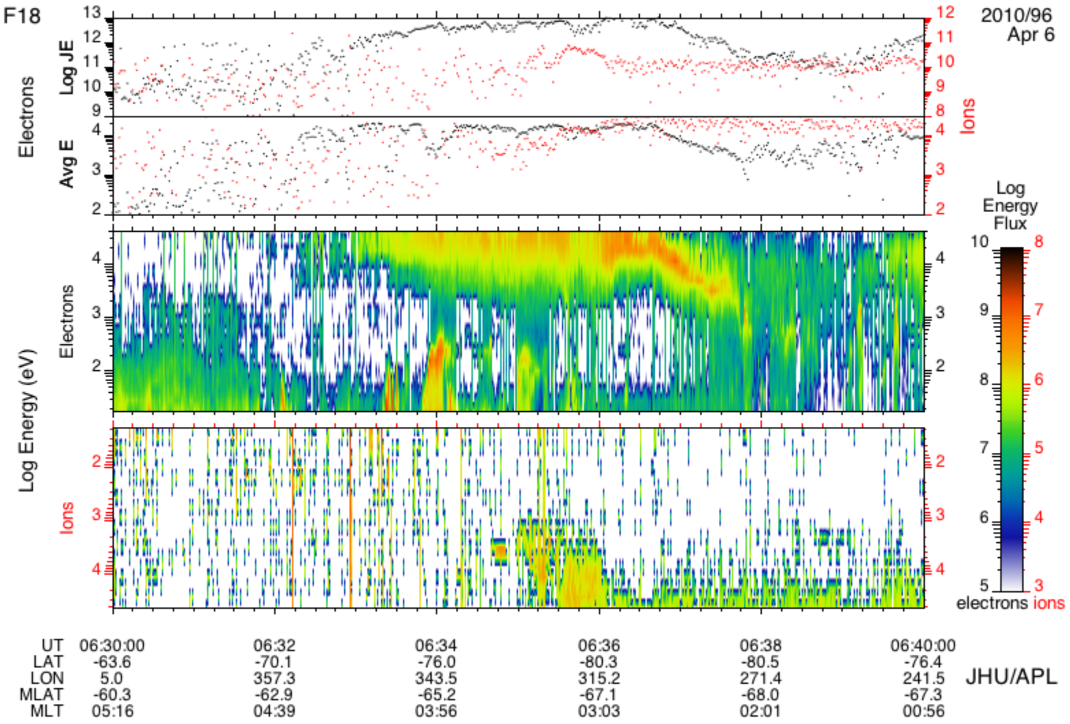

Figure 5.8: A particle spectrometer record from DMSP satellite F18 during 0630-0640 UT 6 April 2010. Very high electron energies (>10 keV) with high-energy flux were present, extending from 293-350° geographic longitude and 74-80°S geographic latitude i.e. in the observation area of site Eagle. This suggests hard auroral precipitation. Note also the short period of high-energy proton precipitation at ~0635 UT.

Figure 5.9a shows a sample single-satellite time series of detrended 50 Hz L1 phase fluctuation during 0704 UT on 6 April 2010 at site Eagle. The low frequency component due to satellite movement has been removed by a 6th order Butterworth filter with cutoff frequency 0.1 Hz (see Section 4.3). Figure 5.9b shows an accompanying energy density spectrum of phase fluctuations from PRN 16, obtained by Fourier transform of 9000 50 Hz samples (three minutes in time). Phase fluctuations were occurring on a time-scale of several seconds, implying that the ionospheric changes were of correspondingly longer time scales than those associated with classical diffractive scintillation. This is also supported by the phase scintillation spectrum (Figure 5.9b) that shows significant phase fluctuation occurrence at lower frequencies. It is likely that TEC gradients, associated with local precipitation energy input, were the cause of the phase scintillation in this case.

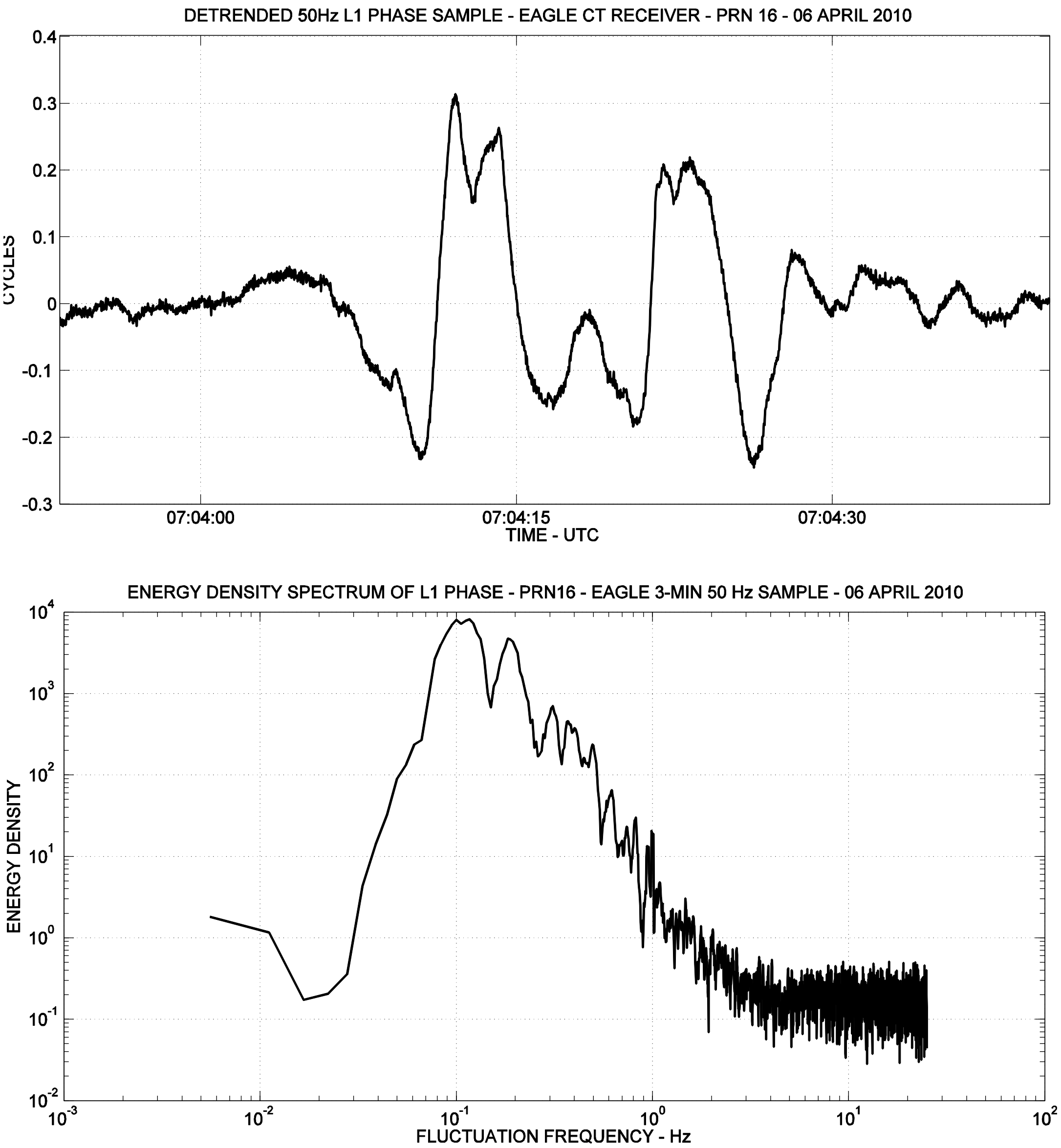

Figure 5.9 – A sample of detrended 50 Hz L1 phase fluctuation from PRN16, recorded at site Eagle during 0704 UT on 6 April 2010 (5.9a) and accompanying smoothed energy density spectrum of the phase fluctuation using a total of 9000 samples around this time (5.9b). Detrending was performed using a high-pass 6th order Butterworth filter with cutoff frequency of 0.1 Hz. Phase fluctuations were occurring on a time-scale of several seconds, implying that the ionospheric changes were of correspondingly longer time scales than those associated with classical diffractive scintillation.

Incoherent scatter radar measurements [e.g. *Haldoupis et al.*, 2000; *Yin et al.*, 2008; *Mitchell et al.*, 1998] have previously shown that during strong precipitation events, enhancements in E-region electron density can reach up to 4x10^{11} electrons per cubic metre over an extended altitude range. Projecting this electron density over, for example, an arbitrary 50 km vertical distance equates to ~2.5 TECU. Taking into account also the low elevation nature of GPS ray path geometry at high-latitudes, phase fluctuations such as those in Figure 5.9a could feasibly have arisen from E-region irregularities.

5.4.2 Large-scale plasma structuring

The time sequence of large-scale (hundreds of kilometres) plasma structuring in Figure 5.4 above shows a plasma enhancement structure ‘breaking off’ from the lower-latitude solar-produced plasma, resulting in a large southward drifting plasma ‘patch’ and apparent depletion region at the break-off point. The reconstructed enhancement ‘patch’ in the 1630 UT image of Figure 5.4 is approximately 1000 km long and 500 km wide; however 500 km is approaching the limit of the reconstruction resolution. The plasma depletion region is interesting since it occurred in the sunlit sector of the polar region, and appeared to be well equator-wards of the cusp, within the auroral oval. It has been suggested above that the depletion region was due to enhanced recombination of O^+ due to soft electron precipitation. However it is important to consider whether the depletion region could be an artefact of the tomographic imaging process, particularly because there is not an abundance of data in the Antarctic region. To address this issue a completely separate imaging method, Ionospheric Data Assimilation Four-Dimensional (IDA4D) [*Bust et al.*, 2004], based on data assimilation techniques was run over the same time periods as MIDAS. For the 5 April 2010 analysis, IDA4D used IRI (International Reference Ionosphere) as a background initial model, and ingested the same dual-frequency GPS data set from 50 sites shown in Figure 5.1, i.e. identical ray path observations were processed by both MIDAS and IDA4D assimilation tools. In addition, IDA4D ingested TEC from the ~55 ground DORIS (Doppler Orbitography and Radio-positioning Integrated by Satellite) stations, including four on the continent of Antarctica, LEO satellite occultation TEC from five COSMIC (Constellation Observing System for Meteorology, Ionosphere and Climate) satellites, LEO satellite topside TEC data from five COSMIC satellites and SAC-C (Satellite de Aplicaciones Cientifico-B). IDA4D uses a Gauss-Markov Kalman Filter to predict the solution forward in time.

Figure 5.10 shows IDA4D specification of TEC over Antarctica at 1645 UT, overlaid with the data coverage ingested in its production. There is broad agreement with the MIDAS result shown in Figure 5.4. The two imaging methods use different algorithms and assumptions and further, IDA4D has used radio occultation data from COSMIC. Of particular note is the improved data coverage in the IDA4D specification across the region of depletion in plasma entering the polar cap. This provides some confidence in the accuracy of the TEC maps.

Further verification is provided by the GPS receivers on-board the CHAMP and GRACE satellites. Figure 5.11a shows the upward looking vertical TEC projection above the CHAMP satellite altitude of ~300 km. It is clear that there is an enhancement of electron density in the topside ionosphere above the satellite in the vicinity of the plasma enhancement 'patch' from the tomographic images. Figure 5.11b shows a similar plot of vertical TEC for the GRACE satellite altitude of ~480 km. It is noted that the high altitude of the patch may be indicative of the *Carlson et al.* [2006] mechanism of formation. Thus, the plasma enhancement region is believed to be a real physical effect, most likely a result of anti-sunward plasma drift from a TOI separation being sustained by field-aligned soft electron precipitation.

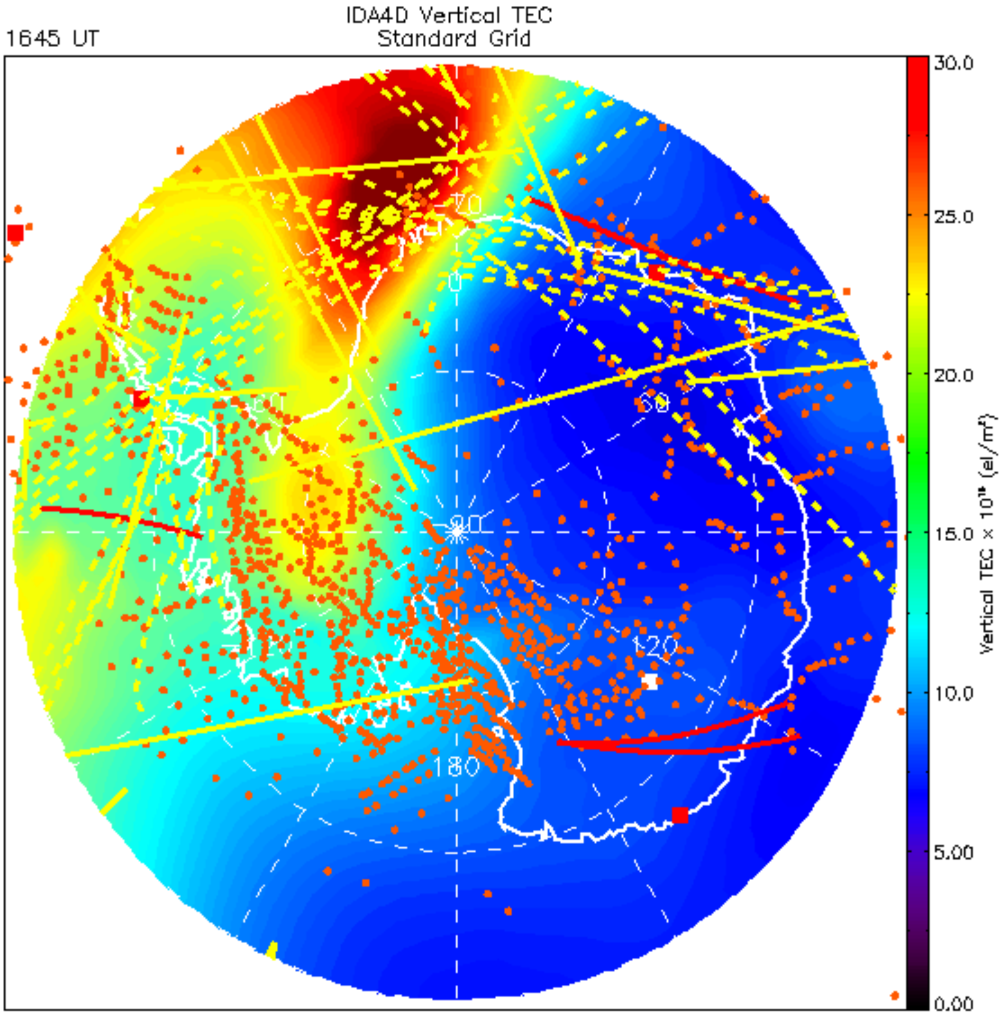

Figure 5.10: IDA4D TEC image over Antarctica at 1645 UT on 5 April 2010, overlaid with ingested data coverage. Solid yellow lines show COSMIC occultation intercepts (derived from the longest great-circle paths between receiver and satellite, along the occultation trajectory up to 800 km altitude). Orange dots represent GPS ray path intercepts at 350 km. Dashed yellow lines show topside TEC intercepts at 1000 km from COSMIC, CHAMP and GRACE. Red squares and lines show DORIS coverage at 350 km intercepts. This reconstruction used identical GPS ray path observations to the MIDAS method, with the addition of TEC input from DORIS, COSMIC and SAC-C instruments and a Kalman filter approach.

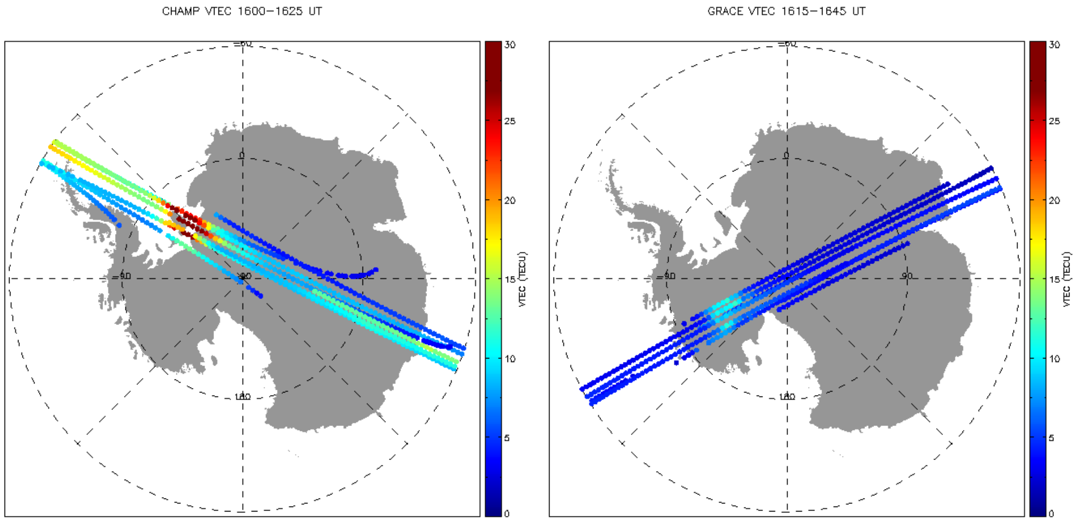

Figure 5.11 (a,b): GPS vertical TEC projections over Antarctica above (11a) the CHAMP satellite between 1615-1645 UT and (11b) the GRACE satellite between 1600-1625 UT. Both show enhancements in TEC at the crossing of the plasma enhancement 'patch', with the GRACE levels slightly lower due to its orbital altitude above the bulk of the F-region.

5.5 Summary

First results from a remote network of Antarctic GPS Ionospheric Scintillation and TEC Monitors have been presented in this Chapter. The scintillation receivers have operated remotely and over extended periods in the extreme environmental conditions of the central Antarctic plateau.

An extended period of moderate GPS L1 phase scintillation has been identified at polar cap and auroral latitudes during 5 and 6 April 2010 in response to a CME. The majority of observed satellites at the geographic South Pole displayed elevated σ_φ indices during a ten hour period from ~0830 UT to 1830 UT. There was also significant phase scintillation at 81°S at site Eagle.

TEC images from GPS tomography have revealed the presence of plasma enhancement 'patch' structure during 5 April 2010, which formed and dissipated between the hours of ~1200-1900 UT. Shortly after an IMF B_z and B_y change at midday UT, plasma was transported pole-wards from sunlit mid-latitudes and gradually separated as an isolated travelling structure moving in the convection pattern along the solar terminator. The plasma concentration remained largely within the local dawn-midday sector during the entirety of its lifetime. TEC from three semi-independent sources, the IDA4D assimilation tool and satellite passes from CHAMP and GRACE, have supported the presence of this plasma structure.

Superposition of phase scintillation indices onto the MIDAS TEC images has allowed the examination of spatial and temporal correlation with plasma gradients associated with the plasma enhancement structure. Phase scintillation was present throughout both days and was not necessarily associated with plasma gradients. However, there was one notable time between 1600-1700 UT on the first day when there was evidence of spatial association between a depletion region at the plasma enhancement break-off region and the phase scintillation.

There were limited DMSP satellite passes in close proximity to the scintillation regions. However, the passes of DMSP and POES did show general elevated levels of electron and ion temperature and energy, indicating that there was precipitation into the polar cap.

Three distinct scintillation events were identified. In the first, soon after the CME, there were phase scintillations associated with the dayside cusp confined to a short MLT window. They occurred in short bursts of ~30 seconds, with 4-5 clear oscillations. The second event was associated with a sunlit TEC depletion region where the plasma enhancement structure entered the polar cap and separated from the dayside plasma. The third event was on the nightside on the second day, where elevated levels of phase scintillation were observed in a region of low TEC.

Previous studies from the Arctic have indicated a number of mechanisms for scintillation on GPS signals, for example cusp precipitation, auroral precipitation and gradient drift/turbulence. This Antarctic experiment indicates that the most likely cause of scintillation during this storm is particle precipitation causing irregularity structuring on both the dayside and the nightside ionospheres.

6 Auroral emissions as a proxy indicator of scintillation

This chapter investigates the relationship between GPS phase scintillation and the optical emissions of the *aurora Australis*, or Southern Lights. A long-standing assumption is that the visible features of the aurora can be used as a proxy indicator for the small-scale ionization structuring caused by particle precipitation, although its validity has never been fully tested. This unique experiment aims to quantify this proxy using instrumentation at the geographic South Pole. A GPS scintillation receiver and collocated all-sky imager (ASI) allow the superimposition of scintillation measurements and images of the aurora during the dark winter periods in Antarctica. Correlation statistics are obtained using a new image processing technique, which provide the first quantitative evidence that discrete auroral structuring is closely related in space and time with GPS phase scintillation.

The results presented in this Chapter are published in the *Journal of Geophysical Research* [*Kinrade et al.*, 2013].

6.1 Introduction

Ionospheric irregularities are too small to be imaged directly by current GPS tomography methods. The results of the Antarctic study in Chapter 5 showed that tomographic reconstructions of electron density can be used to locate areas of large-scale TEC gradients associated with scintillation activity, where it is expected that structures cascade down to smaller scales. The study also revealed evidence, however, of auroral particle precipitation driving phase scintillation in the absence of large-scale TEC gradients. All-sky imagers can capture the comparably fine detail of auroral optical emissions, which have long been assumed to be a proxy indicator of direct ionization structuring from auroral particle precipitation. GPS phase scintillation activity associated with auroral arcs has been reported in isolated cases (see Section 3.1), supporting this assumption.

There is not a direct physical link between optical auroral emissions and ionospheric scintillation. Photon release is a discrete energy product from the delayed relaxation of excited ions after collisional ionization (see Section 2.3.2). However, the optical emissions are to some extent expected to be local to the immediate area of ionization or ‘radio aurora’ (this is dependent on the energy and flux of incoming particle precipitation, altitude and neutral densities present). For example *Kintner et al.* [2002] observed TEC increases of 10 TECU coincident with auroral arcs in ASI images over timescales of several minutes. Using collocated equipment at the South Pole, this study examines the spatial and temporal correlation of ionospheric GPS scintillation with the intensity of optical auroral emissions. If a link can be quantified between the optical aurora and GPS scintillation, it may be feasible to use optical emissions as a proxy indicator of small-scale plasma structuring on a more systematic basis. The study of ionospheric irregularities and scintillation would benefit from a source of small-scale plasma observations.

6.2 Instruments & method

6.2.1 GPS scintillation receiver

In 2010 the University of Bath installed a *Novatel* GSV4004 GPS scintillation receiver at the South Pole. The antenna is located on the roof of Amundsen-Scott research station, less than 30 m from the true geographic pole. The receiver records amplitude and scintillation parameters as described in Section 4.3, which also details the data treatment process. Data is currently stored on a local computer at the research station, and sent back to the University of Bath periodically for processing.

6.2.2 South Pole All-Sky Imager (ASI)

The all-sky imager (ASI) at South Pole provides horizon-to-horizon images of optical auroral emissions at multiple emission wavelengths, as described in Section 4.6.4. The imager is located several meters away from the University of Bath’s GPS scintillation receiver, on the roof of Amundsen-Scott research station.

6.2.3 Image processing & satellite tracking

The optical images are mapped onto a geographic coordinate projection, to facilitate the matching of scintillation measurements with optical-image pixels using latitude/longitude pierce point positions. This requires the assumption of fixed altitude shells at 120 km and 200 km; these shell heights were chosen because they are characteristic of the most intense nightside 557.7 nm and 630.0 nm atomic oxygen emissions respectively [*Sandholt et al.*, 2002]. Satellite-to-ground pierce points are calculated using GPS sp3 orbit file coordinates and intersection with the assumed emission altitudes. The mapping transform is demonstrated in Figure 6.1. A limitation of the instruments and method is that the image aspect represents the optical aurora from one position on the ground i.e. at low elevation viewing angles the ability to discern field-aligned structures is lost, and the intensity measurement represents an integral summation of the emissions. At the South Pole, the GPS constellation only provides elevation satellite coverage of up to ~43° above the horizon, however the geometric projection of scintillation measurements on to 120 km and 200 km altitude shells somewhat constrains the observation area to the central portion of the topside-mapped and distortion-corrected images (where auroral arc or 'curtain' features are still discernible). The use of multiple ground-based ASIs and/or topside satellite based optical instruments is required to better resolve small-scale structures over a large area.

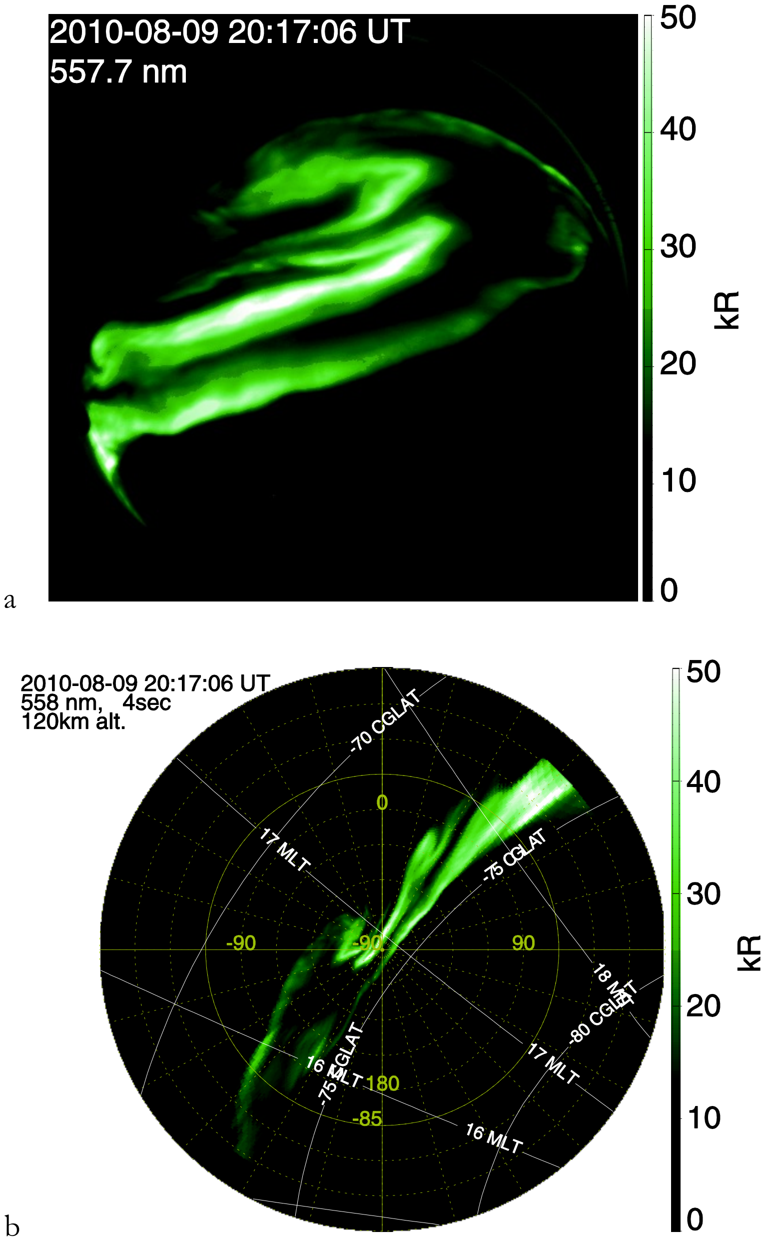

Figure 6.1 – 6.1a an exemplary 557.7 nm emission image from the South Pole all-sky imager (ASI) on 9 August 2010 at 20:17:06 Universal Time (UT). The ASI is oriented so that the image appears as it would if the viewer was looking directly overhead (at the zenith) whilst stood at the geographic South Pole, with the Greenwich Meridian line passing vertically down the centre of the image. The silhouette of the GPS antenna is just visible in the bottom-left edge of the image. Image processing is used to correct the images for wide-angle lens distortion and to map the pixels to the geographic coordinate system at shell heights of 120 km (557.7 nm emissions) and 200 km (630.0 nm emissions). Image 6.1b shows a corrected and pixel-mapped image, now orientated so that the viewer is looking from above (essentially how the aurora might appear from low-Earth orbit). Yellow lines indicate the geographic coordinate grid, with the majority of the useful image area falling within the latitude range 85-90°S. The colour-scale is in Rayleighs, a photometric unit, and applies to both images 6.1a and 6.1b.

Each satellite pierce point, calculated using a fixed and assumed altitude shell, has an unknown level of uncertainty with regard to how closely it is matched with the true height of the optical emissions. This limitation motivates the statistical treatment of the images to improve conditions for spatial-based cross correlation with the GPS data and reduce pixel noise. Matrices of mean emission intensity are produced with one value representing each pixel for each time step by averaging each original pixel intensity value with respect to its surrounding pixels (+/- 5 pixels in the vertical and horizontal) i.e. a moving operator window. This process is also repeated to obtain 'maximum' intensity images, taking the brightest value within the operator window. The use of these processed matrices (particularly the 'maximum' values) in correlation with tracked GPS ray path measurements increases the likelihood of a scintillation event being matched correctly with smaller scale auroral emission structures such as wisps or curtains. Post processing, optical images have a pixel resolution of 200 × 200, with each pixel space corresponding to an approximate physical dimension of 7.8 km – this dictates the lower limitation of scale for resolving structures within the processed images.

Each scintillation measurement is time-matched with an optical image to within one minute, with the closest image pixel position determined by calculating the least Euclidean distance between the orbit-derived latitude and longitude pierce point and the image coordinate grid (i.e. grid distance and not physical distance). A three-point moving average filter is then also applied to the image pixels and scintillation measurements in time to improve conditions for cross correlation. By tracking multiple satellites in time and space, two collective time series result from the image processing; tracked emission intensities, $x_i(k)$, and phase scintillation measurements, $x_j(k)$. Correlation statistics are obtained directly from these two time series. The cross correlation coefficient, R_{ij}, is related to the cross correlation, C_{ij}, by the following equations:

$$R_{ij} = \frac{C_{ij}}{\sqrt{C_{ii}C_{jj}}} \tag{6.1}$$

$$C_{ij} = \frac{1}{N-1}\sum_{k=1}^{N}(x_i(k) - \mu_i)(x_j(k) - \mu_j) \tag{6.2}$$

$$\mu_i = \frac{1}{N}\sum_{k=1}^{N} x_i\,(k) \tag{6.3}$$

$$\mu_j = \frac{1}{N}\sum_{k=1}^{N} x_j\,(k) \tag{6.4}$$

Accompanying visual plots depict the optical image with superimposed scintillation measurements from each tracked satellite (Figures 6.2 & 6.3 in Section 6.4.1 are examples); the σ_φ values are plotted as area-scaled white circles, intended to highlight the apparent visual correspondence between signal phase variance and emission intensity at the pierce points.

A total of 17 visible aurora days were selected for study from the Antarctic winters of 2010-11, with activity ranging in intensity, duration and structuring. Selection was on a visual basis, discounting images that captured the moon (an unwanted source of brightness that effectively masks the auroral emissions in an image) and favouring image sequences that displayed discrete or persistent auroral structuring. Correlation was performed at both wavelengths for each entire case study day (all satellites and all time samples available, Appendix Tables 10.1 & 10.2 in Section 10.2.1), and additionally over visually selected time intervals of pronounced auroral activity (Tables 6.2 & 6.3), ranging from discrete auroral arcs to diffuse brightening. This visual selection sought to isolate 'burst' periods i.e. the entire lifetime of an arc or active period from formation to dissipation. By removing extended periods of 'dark sky' from the time series, images that are not of interest are removed and the statistics represent more closely the relationship between the optical emissions and associated GPS phase fluctuations. The dates studied are listed in Tables A1 & A2 in Section 6.7.1. Notable times of interest throughout these dates are listed in Tables 6.2 & 6.3. Summarized image sequences can be viewed online [*Ebihara*, 2007].

6.3 Results & analysis

6.3.1 Discrete auroral arc – 9 August 2010

Of all the dates studied, the imagery of the auroral arc occurring over the Antarctic on 9 August 2010 displayed the most discrete and persistent optical activity. The imager recorded strong optical emissions (> 40 kR) present during the times 1900-2200 Universal Time (UT). The arc spanned Magnetic Local Times (MLT) of 1600-1900 MLT at latitudes ~73-74° CGLAT. The duration and relatively stable magnetic position of the arc made it a useful candidate for tracking coincident scintillation 'through' the optical images, and illustrating the method as a first case study here. Figures 6.2 and 6.3 provide a selection of geographic projections of 557.7 nm and 630.0 nm emission intensities and GPS L1 phase scintillation indices respectively, illustrating their visual correspondence – this was readily observed when the images were viewed in time-lapse animation.

Two time series result from simultaneously tracking the observed satellites 'through' the filtered ASI images; Figure 6.4 shows the collective satellite mean 557.7 nm intensity and σ_φ fluctuations on 9 August 2010. Periods of auroral brightening can be seen mainly around 0300 UT and 2000 UT, which matched well with 'burst' periods of phase fluctuation. A smaller peak response was also present around 0500 UT. It is also important to note the occurrence of increased levels of phase fluctuation in the absence of optical emissions at this wavelength, during 1600-1700 UT for example, when it is likely that either a different physical mechanism was responsible for the ionospheric irregularities affecting L1 signal propagation (see Section 6.4.2), or that particle precipitation was predominant at a different altitude at that time. Comparison of the tracked time series at dual emission wavelengths allows a basic level of altitude discrimination. Figure 6.5 shows the tracked 630.0 nm time series on 9 August 2010. Referring to Figures 6.4 & 6.5, the phase fluctuations between 1600-1700 UT appear to be associated with 630.0 nm emissions at 200 km, but not 557.7 nm at 120 km, indicating that the responsible ionization structuring was nearer the F-region at the time. This is a significant finding, as it supports the possible use of multiple-wavelength auroral images to determine both the sky area of likely scintillation conditions, and the approximate altitude of the driving ionization. Polar cap ionization patches have been observed to exhibit low intensity (100-500 Rayleigh) [OI] red 630.0 nm emissions at F-region altitudes [*Garner et al.*, 1996], however this level of brightness is close to the ASI noise threshold in the context of this experiment, particularly for the weaker 630.0 nm emission line, as discussed in Section 4.6.4. Detection of polar cap patch-related emissions can be improved by increasing image exposure times, and is an interesting aspect of planned future work.

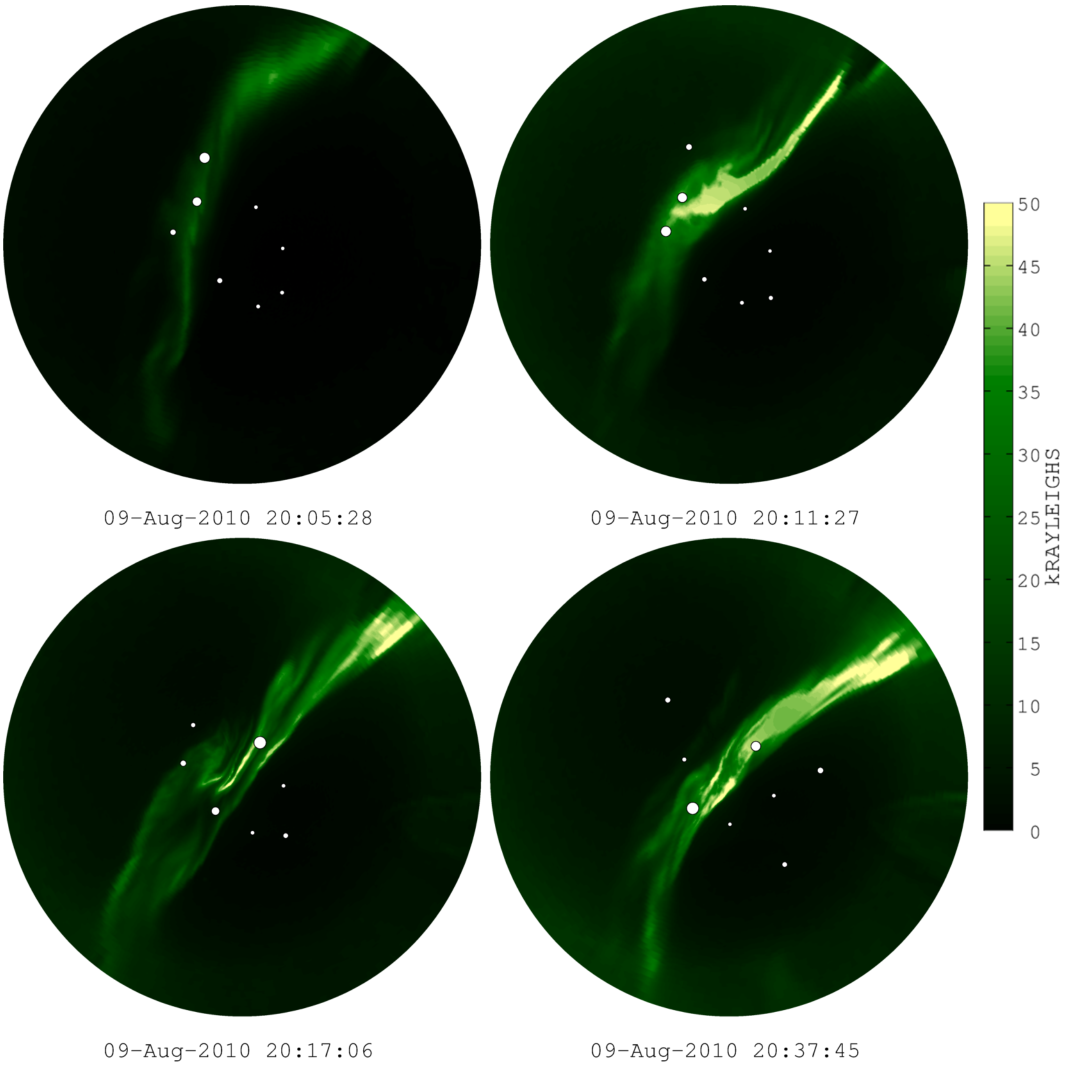

Figure 6.2 – A selection of combined geographic projections of 557.7 nm emission intensity (kR) and GPS L1 phase scintillation indices (60-second σ_φ) at times 6.2a 20:05:28 UT, 6.2b 20:11:27 UT, 6.2c 20:17:06 UT and 6.2d 20:37:45 UT on 9 August 2010 at South Pole. A common shell height of 120 km is assumed (characteristic of peak 557.7 nm atomic oxygen emissions on the nightside). The phase scintillation indices are plotted as area-scaled white circles, intended to highlight the apparent visual correspondence between signal phase variance and emission intensity at the pierce points; on visual inspection the phase variance appeared to increase when the pierce point traversed brighter areas of emission. This relationship was most apparent when projections were viewed as a time-lapse animation. The colour mapping of emission intensity uses a black-green-yellow scale for clarity.

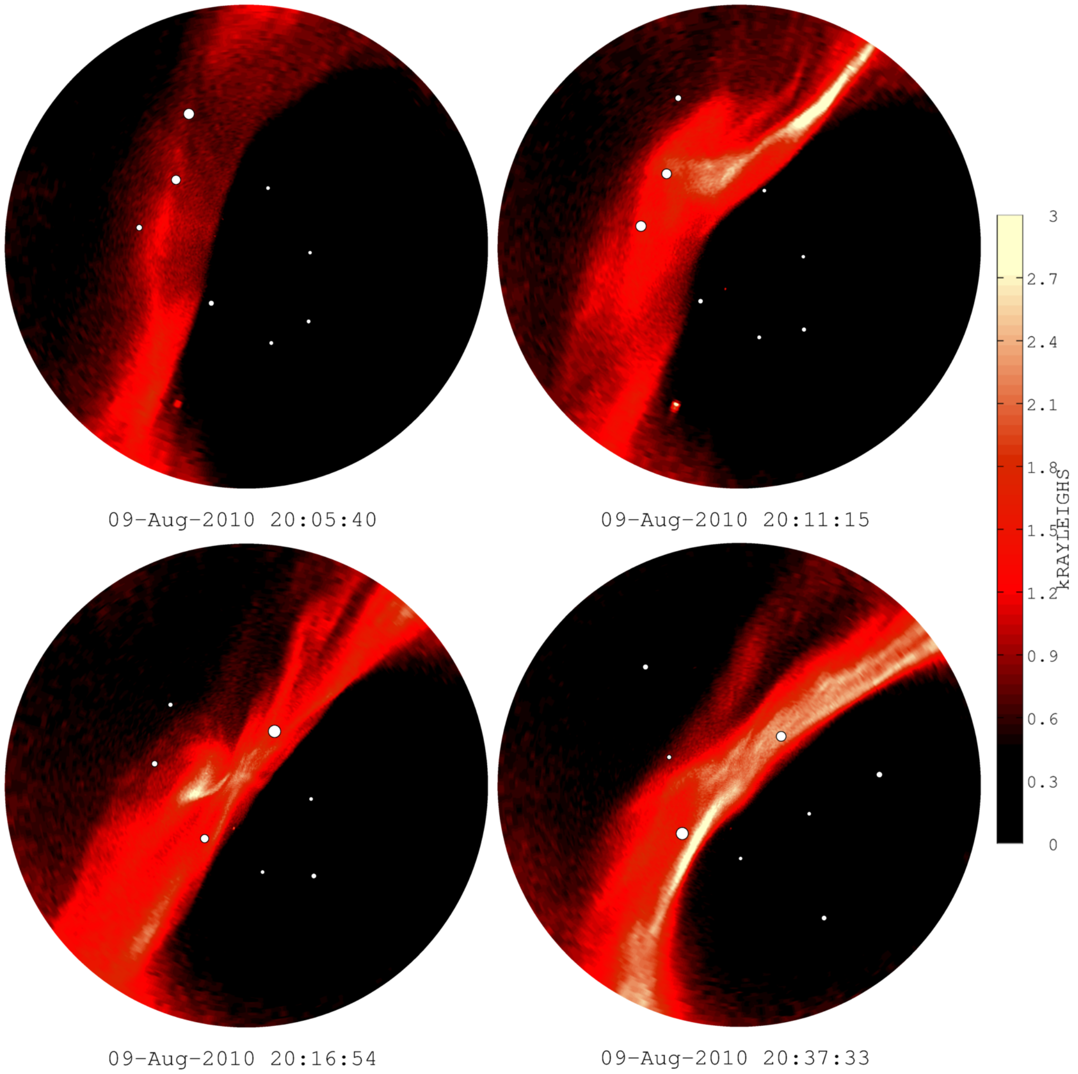

Figure 6.3 – A selection of combined geographic projections of 630.0 nm emission intensity (kR) and GPS L1 phase scintillation indices (60-second σ_φ) at times 6.3a 20:05:40 UT, 6.3b 20:11:15 UT, 6.3c 20:16:54 UT and 6.3d 20:37:33 UT on 9 August 2010 at South Pole. Note the generally lower intensity of the 630.0 nm emissions compared with those at 557.7 nm in Figure 6.2. An altitude shell height of 200 km is assumed (characteristic of peak 630.0 nm atomic oxygen emissions on the nightside). The colour mapping of emission intensity uses a black-red-yellow scale for clarity.

This illustrative case study provides clear evidence that regions of intense auroral optical emissions can be associated with GPS phase fluctuations. During the discrete arc event on 9 August 2010, examination of the tracked time series on an individual satellite basis (see Figure 6.6) revealed spatial and temporal 557.7 nm correlations of between 62-89% at 120 km altitude over the three-hour period 1900-2200 UT (see Table 6.1). During the same period emissions at 630.0 nm also correlated between 24-75% on an individual satellite basis at 200 km (Table 6.1). The collective satellite correlation during this period was 69% for 557.7 nm emissions at 120 km and 57% for 630.0 nm emissions at 200 km (see Tables 6.2 & 6.3). Additionally, statistical p-values indicated that the probability of these correlation levels occurring through random chance was practically zero. The proxy relationship between the auroral emissions and GPS phase fluctuations was therefore statistically significant.

Table 6.1. Selected 557.7 nm and 630.0 nm correlation statistics during 1900-2200 UT on 9 August 2010[a]

PRN[b]	No. data points	R_{558}	R_{LO}	R_{UP}
32	180	0.8875	0.8518	0.9150
20	251	0.8723	0.8391	0.8990
31	429	0.8105	0.7754	0.8407
23	340	0.6262	0.5569	0.6868
4	392	0.6260	0.5618	0.6827
30[c]	385	-0.0534	-0.1525	0.0468
		R_{630}		
31	179	0.7530	0.7089	0.7913
32	251	0.7431	0.6693	0.8023
20	429	0.6403	0.5609	0.7080
4	340	0.5747	0.5043	0.6374
23	392	0.5738	0.4978	0.6411
30	384	0.2445	0.1480	0.3363

[a] R_{558} is the linear cross correlation coefficient between mean 557.7 nm emission intensity and σ_φ indices at 120 km altitude. R_{630} is the linear cross correlation coefficient between mean 630.0 nm emission intensity and σ_φ indices at 200 km altitude. R_{LO} and R_{UP} are the lower and upper 95% confidence limits of the correlation coefficient respectively.

[b] Pseudo Random Noise (PRN) satellite code.

[c] PRN 30 displayed little phase variation during the auroral arc event, and its ray paths did not traverse the auroral arc at 120 km; its inclusion serves to show a typical 557.7 nm noise-floor correlation level.

Table 6.2. Collective-satellite 557.7 nm correlation coefficients[a]

Date	Time span (UT)	No. Data Points	R_{558}	R_{LO}	R_{UP}	Max. σ_{φ}	Max. I_{max}
2011-07-31	2202-2359	1842	0.7421	0.7209	0.7620	0.5628	50828
2010-08-09	1901-2200	3337	0.6871	0.6688	0.7046	0.2902	50457
2010-05-21	0001-0300	3266	0.6423	0.6217	0.6620	0.5248	49791
2011-05-26	0002-0115	1362	0.6402	0.6077	0.6705	0.4814	51688
2011-04-30	2031-2130	636	0.6048	0.5531	0.6519	0.5049	49697
2011-05-04	0002-0215	2465	0.6030	0.5773	0.6276	0.5698	3220
2011-05-03	0002-0159	2083	0.5854	0.5565	0.6310	0.4121	46179
2011-05-02	0003-0130	1154	0.5785	0.5388	0.6157	0.5988	46730
2010-08-03	0000-0130	1724	0.5761	0.5437	0.6068	0.4071	20584
2010-06-16	0041-0359	3497	0.5662	0.5432	0.5883	0.4166	36075
2010-05-20	0146-0330	1931	0.5256	0.4926	0.5572	0.4098	49920
2010-08-09	0201-0900	7477	0.4853	0.4678	0.5024	0.2796	40348
2011-07-25	0002-0630	6824	0.4375	0.4181	0.4565	0.3254	17514
2011-05-28	0003-1130	6346	0.4371	0.4170	0.4568	0.4459	10138
2011-05-03	1702-2159	5495	0.4290	0.4072	0.4503	0.2556	40119
2011-05-01	0003-0259	2675	0.3978	0.3654	0.4292	0.3146	35219
2010-08-04	0016-0130	1219	0.3366	0.2858	0.3854	0.6109	18318
2011-05-03	1102-1359	3170	0.1775	0.1436	0.2110	0.6141	43775
2011-05-01	0831-0859	428	0.0578	-0.0372	0.1518	0.2882	46374
2011-05-01	1603-2359	7214	0.0323	0.0093	0.0554	0.5248	36243

[a] Collective-satellite correlation coefficients during notable periods of optical auroral activity, using maximum intensity 557.7 nm emission images. Peak values of σ_{φ} indices and emission intensity, I_{max}, from all observed satellites in the time interval are provided for reference.

Table 6.3. Collective-satellite 630.0 nm correlation coefficients[a]

Date	Time Span (UT)	No. Data Points	R_{630}	R_{LO}	R_{UP}	Max. σ_φ	Max. I_{max}
2011-07-31	2202-2359	1821	0.6253	0.5965	0.6525	0.5628	3646.1
2010-06-16	0041-0400	3498	0.5791	0.5567	0.6007	0.4543	3789.9
2010-05-20	0146-0330	1921	0.5765	0.5458	0.6056	0.3480	5246.8
2010-08-09	1901-2200	3339	0.5745	0.5513	0.5968	0.2780	4350.5
2011-05-03	0002-0159	2072	0.4937	0.4604	0.5256	0.4358	3734.8
2010-08-04	0016-0130	1227	0.4846	0.4406	0.5263	0.6109	5512.9
2011-07-25	0002-0630	6776	0.4809	0.4624	0.4990	0.3410	5134.2
2010-08-09	0201-0900	7470	0.4679	0.4500	0.4854	0.3310	5179.0
2011-05-01	0002-0259	5102	0.4665	0.4448	0.4877	0.3993	4274.7
2011-05-28	0002-1130	6344	0.4642	0.4447	0.4833	0.4459	4861.3
2011-04-30	2031-2130	1270	0.4393	0.3938	0.4826	0.5049	5643.2
2011-05-04	0002-0215	2441	0.4084	0.3748	0.4410	0.5247	2410.9
2011-05-01	1602-2359	13802	0.3966	0.3825	0.4106	0.5512	6286.6
2011-05-03	1102-1359	3179	0.3923	0.3625	0.4213	0.4828	3515.0
2011-05-03	1702-2159	5497	0.3871	0.3643	0.4093	0.2849	4223.7
2010-05-21	0001-0300	3277	0.3600	0.3298	0.3894	0.6034	3505.4
2010-08-04	1031-1645	6630	0.3544	0.3331	0.3752	0.5360	3625.1
2010-08-03	0001-0130	1744	0.3450	0.3030	0.3857	0.4071	1989.7
2011-05-02	0002-0130	2312	0.3118	0.2745	0.3481	0.5988	5197.4
2011-04-30	0831-1630	13634	0.2889	0.2734	0.3042	0.5473	7663.8
2011-05-01	0831-0859	738	0.0799	0.0078	0.1512	0.3101	3519.3

[a] As for Table 6.2, but using maximum intensity 630.0 nm images.

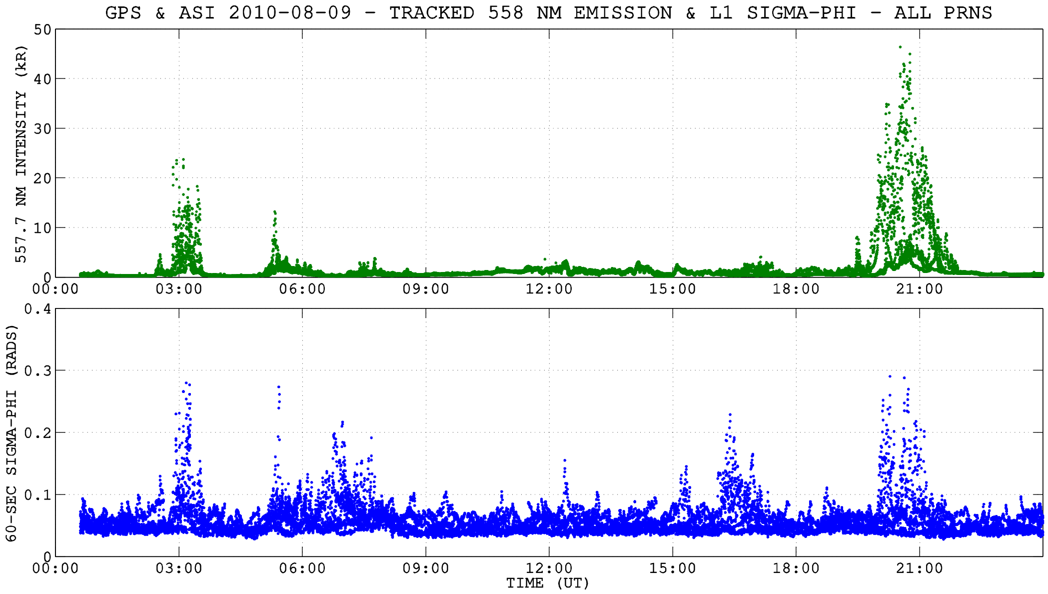

Figure 6.4 – Two time series result from simultaneously tracking the observed satellites 'through' the filtered ASI images; mean 557.7 nm emission intensities (top, green) and GPS L1 60-second σ_φ indices (bottom, blue) at 120 km pierce points coincident in space and time. Periods of auroral brightening can be seen here mainly around 0300 and 2000 UT on 9 August 2010, which matched well with 'burst' periods of phase fluctuation. A smaller peak response was also present around 0500 UT. It is also important to note the occurrence of increased levels of phase fluctuation in the absence of optical emissions, during 1600-1700 UT here for example, when it is likely that a different physical mechanism was responsible for the ionospheric irregularities affecting L1 signal propagation, or that particle precipitation was predominant at a different altitude at that time (see Figure 6.5).

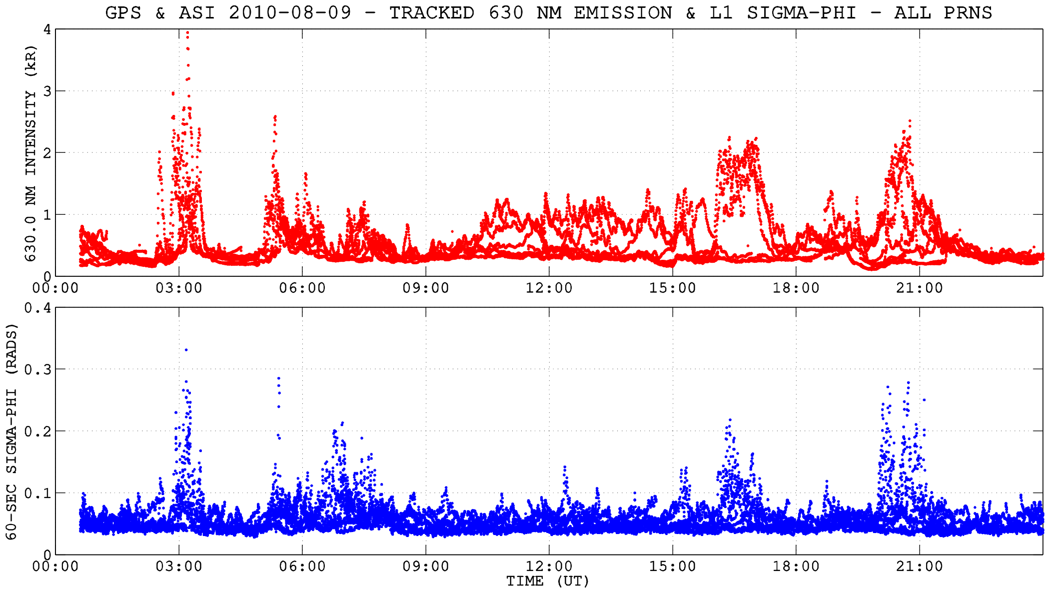

Figure 6.5 – Tracked mean 630.0 nm emission intensities (top, red) and GPS L1 60-second σ_φ indices (bottom, blue) at 200 km pierce points during 9 August 2010. The 630.0 nm emissions are characteristically less intense compared with those at 557.7 nm (see Figure 6.3), however the two time series do display a general visual correspondence between optical and phase fluctuation 'bursts.' In addition to the optical activity imaged around 0300 UT and 2000 UT (also at 557.7 nm in Figure 6.4), other instances of correlation may be inferred at 0500 UT and 1600-1700 UT. Interestingly the phase fluctuations between 1600-1700 UT appear to be associated with 630.0 nm emissions at 200 km, but not 557.7 nm at 120 km (see Figure 6.4), indicating that the ionization structuring existed nearer the F-region during the period.

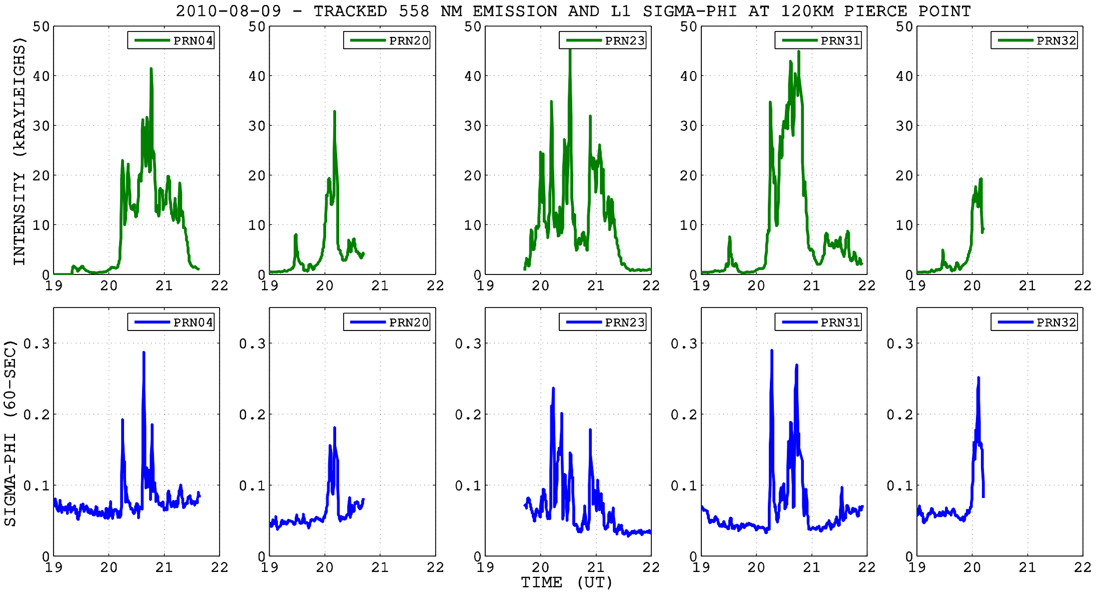

Figure 6.6 – Selected satellite-tracked time-series of GPS L1 phase scintillation indices (bottom row) and mean 557.7 nm emission intensities (top row) at 120 km, during 1900-2200 UT on 9 August 2010. Although only moderate levels of phase scintillation were observed (< 0.3 radians), examining a 'burst' period on a satellite-by-satellite basis reveals that a number of tracked satellites exhibited peak signatures in σ_φ coincident with enhancements in local 557.7 nm emission intensity. Table 6.1 lists the cross correlation coefficients for these satellite tracks.

6.3.2 Other sources of scintillation at high latitudes

It is important to acknowledge that other physical mechanisms causing scintillation can exist at high latitudes, notable during a number of days in this study. Evidence of this is pronounced in Figure 6.7, which compares tracked time series from 557.7 nm and 630.0 nm optical emissions with σ_φ on 28 May 2011. Optical emissions were generally of weak intensity during this day (< 10 kR at 557.7 nm, < 4 kR at 630.0 nm), although peak signatures did correspond spatially and temporally with phase fluctuations up until 1200 UT at both wavelengths (~0200 UT at 557.7 nm for example). After 1200 UT however, a prolonged period of phase fluctuation ensued for ~4 hours across the majority of observed satellites, which was not associated with pronounced optical activity at the wavelengths observed; emission intensity values were minimal and near the image noise floor. It is likely that another physical mechanism was present within the signal propagation environment throughout that time and other similar days in the study. Image reconstructions of Total Electron Content (TEC) indicated the presence of larger scale ionospheric electron density gradients over central Antarctica for a number of hours after 1200 UT on 28 May 2011 (TEC images were produced using MIDAS [created by *Mitchell & Spencer*, 2003, and described in *Chartier et al., 2012*]). In addition to the auroral precipitation processes of interest in this optical study, possible sources of high latitude phase scintillation include electron density irregularities driven by polar cap patch convection [*Buchau et al.*, 1985; *Burston et al.*, 2009; *Mitchell et al.*, 2005].

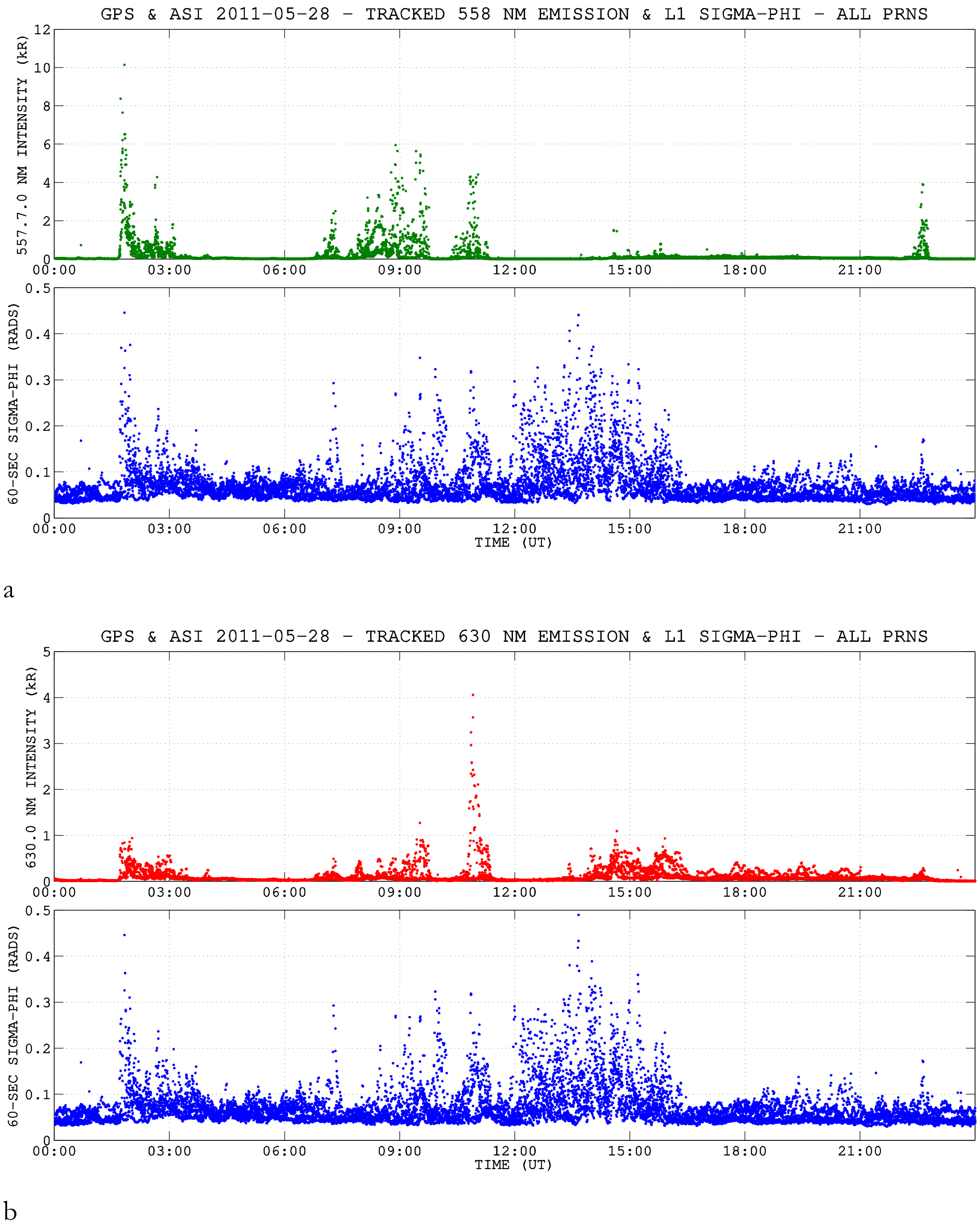

Figure 6.7 – Tracked 557.7 nm (6.7a) and 630.0 nm (6.7b) mean emission intensities and GPS L1 σ_φ indices on 28 May 2011. Although emission intensities were relatively weak throughout the day, peak signatures in emission brightness and moderate phase fluctuation did coincide at both wavelengths until ~1200 UT, more so at 557.7 nm. After 1200 UT however, a prolonged period of phase fluctuation ensued for ~4 hours across the majority of observed satellites, which was not associated with optical activity at the wavelengths observed; emission intensity values were minimal and near the image noise floor. It is likely that another physical mechanism was acting within the signal propagation environment throughout that time to cause the phase fluctuations.

6.3.3 Cross correlation statistics

Collective cross correlation statistics offer a numerical overview of the case studies, important in identifying any proxy relationship between the optical auroral emissions and GPS phase scintillation. The statistics reveal that the proxy relationship between optical auroral emissions and GPS σ_φ was variable over the Antarctic winter days studied. Images at 557.7 nm and 630.0 nm correlated collectively with GPS phase fluctuations to levels ranging 03-74% and 08-63% respectively. Images exhibiting diffuse and finely structured auroral emissions have generally produced lower levels of collective satellite σ_φ correlation. Taking an example, the optical auroral activity throughout the day of 1 May 2011 consisted of a mixture of diffuse brightening and dynamic wisps. A bright and filamentary wisp structure was imaged during 0830-0900 UT (> 40kR intensity), but collective satellite σ_φ correlation was only 6% and 8% at green and red wavelengths respectively (see Tables 6.2 & 6.3). This type of 'fine' structuring has less spatial clarity and longevity than discrete arcs or curtains, and so the numerical outcome of the cross correlation is more sensitive to the simplifications made in the method – namely spatial image filtering, data point time matching and the use of altitude shell heights in pierce point determination. Consider also that the energy and flux of field-guided particle precipitation influence the rate of direct ionization and subsequent intensity of auroral emissions; it follows that discrete and persistent arc structures are likely associated with more pronounced local electron density gradients and therefore GPS scintillation, in comparison with the impulsive and weaker intensity emissions of diffuse or wisp aurorae. Additionally, time series from a number of days in the study exhibited periods of phase fluctuation likely associated with physical processes other than direct auroral ionization, as discussed in Section 6.3.2. Correlation on affected ray paths is therefore likely to have been poor, leading to lower collective correlation values.

Periods of intense and persistent optical activity produced the strongest σ_φ correlation statistics of the study. Discrete auroral arc structures were imaged on several days (notably 9 August 2010 and 31 July 2011) with emission intensities that occasionally saturated the ASI sensor (~44 kR for green 557.7 nm emissions). Over a two-hour period on 31 July 2011, the green and red auroral emissions correlated with collective GPS L1 σ_φ measurements to levels of 74% and 63% respectively. Over a three-hour period on 9 August 2010 the green and red emission correlation levels were 69% and

57% respectively, with individual ray path fluctuations correlating with green emissions at up to 89% (PRN 32, see Table 6.1). Of the selected 557.7 nm image sequences examined, 15 out of 20 cases displayed collective σ_φ correlation above 40% (see Table 6.2). Of the selected 630.0 nm image sequences examined, 12 out of 21 cases displayed collective σ_φ correlation above 40% (see Table 6.3). A correlation level of 40% between observables is an arbitrary reference point here, however the time series and image animations were often more suggestive of a physical relationship than the numerical statistics. As already noted, auroral behavior and GPS phase scintillation are both spatially and temporally dynamic on multiple scales, and so considering the tracking method's limitations and assumptions, the statistics support a proxy relationship between optical emissions and σ_φ in the presence of strong auroral activity. Stronger statistics may be recoverable through the refinement of applied shell heights and spatial image filtering, and an increased focus on individual satellite tracks (additionally high time resolution 50 Hz GPS phase data can help to determine the nature of the physical mechanism causing scintillation, a method to be applied in a future study).

The collective statistics suggest that the 557.7 nm emissions are more closely associated with phase fluctuations than those at 630.0 nm (see Tables 6.2 & 6.3). This is likely due to the relative intensity of the green and red optical aurorae, as the green emissions are characteristically a factor greater than red emissions. The imaged structures are therefore more pronounced from the background image noise and the tracking method is more effective. Note that the 630.0 nm emission lifetimes are characteristically longer than those of the 557.7 nm emissions [*Sandholt*, 2002]; this may also reduce the correlation coefficient of the red time series. Although the use of dual wavelengths facilitates altitude discrimination (see Section 4.6.4), the 557.7 nm images would be the most suitable primary wavelength to examine if the ASI images were to be used to estimate sky-wide GPS scintillation activity.

6.3.4 The σ_φ/I_{558} proxy relationship as a general trend

From an operational perspective, it would be useful to confirm a general relationship between auroral emissions and GPS signal disturbances, and whether there is a particular intensity threshold above which auroral emissions are more likely to be coincident with GPS phase scintillation. This knowledge would aid the systematic analysis of auroral images for determining the likelihood and sky location of scintillation activity. Figure 6.8 summarizes the collective case study (~300,000 data points) probability of the phase scintillation index being above a certain value for a range of 557.7 nm emission intensity (I_{558}) thresholds. This was calculated by summing both the number of occurrences of the optical emission values being above the stated intensity threshold, and the number of occurrences of the σ_φ index being above a threshold given the prior emission intensity condition. The sum of σ_φ occurrences was then divided by the sum of the emission intensity occurrences, yielding the rate of occurrence of scintillation 'events' during auroral emission 'events.' Appendix 10.2.2 provides a mathematical summary of this calculation. There are no universally accepted threshold values for either GPS phase scintillation activity (although a σ_φ value of 0.3 is often used in the literature) or the defining 557.7 nm intensity level of a discrete auroral emission structure, but interpretation of the data set in this way has revealed a general trend – higher values of emission intensity corresponded with more elevated levels of σ_φ index (see Figure 6.8). For example, considering all pierce points in the study that intersected 557.7 nm auroral emissions of intensity 5 kR and over, of those instances ~ 30% of the corresponding σ_φ indices were above the near noise floor of 0.1 radians. Increasing the emission 'event' intensity threshold to 30 kR showed that ~80% of σ_φ values during relatively bright emissions were above 0.1 radians.

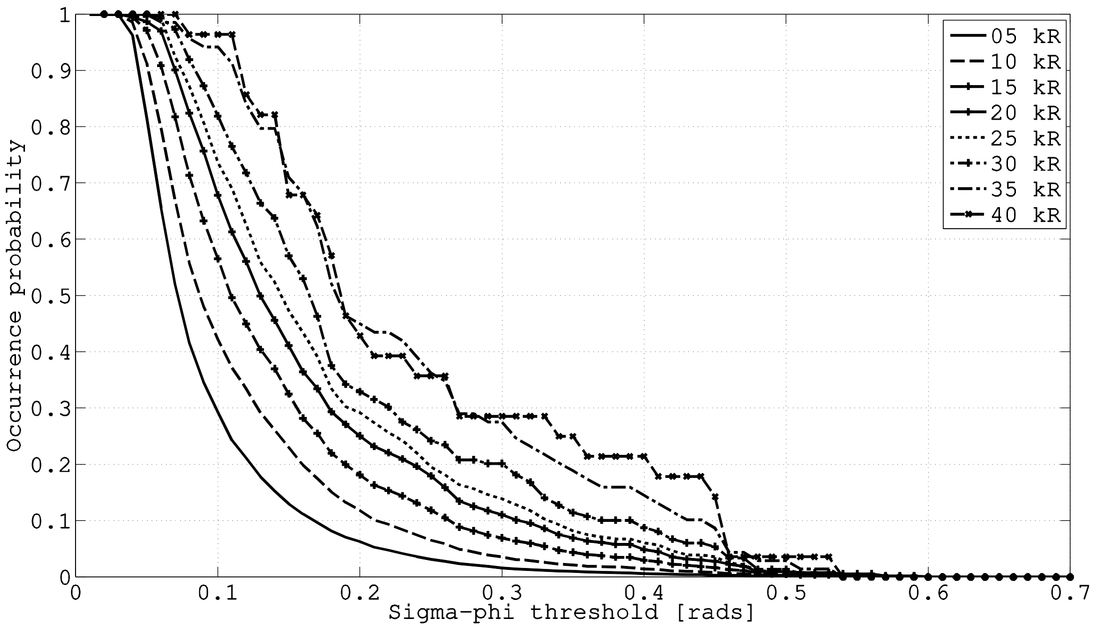

Figure 6.8 – General trend interpretation of the relationship between 557.7 nm emission intensity and GPS phase scintillation indices, incorporating data from all case study days and tracked satellites (~300,000 data points). The plot shows the conditional occurrence probability of the σ_φ index being above a certain value, given a coincident emission intensity threshold at the tracked pierce point; a number of fixed intensity threshold values were used in the calculation, ranging from 5-40 kR, with the σ_φ threshold stepped through values 0.0-0.7 radians for each case. For example, considering all pierce points in the study that intersected 557.7 nm auroral emissions of intensity 40 kR and over, ~30% of the corresponding σ_φ indices were over 0.3 radians. In summary and based on data from this study, the likelihood of σ_φ fluctuation along a ray path increases with higher intensity 557.7 nm emissions around the pierce point.

6.4 Discussion

This study sought to answer the fundamental question: 'when we observe auroral optical emissions overhead, does a GPS receiver experience signal phase fluctuations from ray paths traversing those emissions?' This proxy relationship was found to be variable, and dependent on auroral intensity and structure definition. Spatial and temporal correlation with σ_φ was most defined during intense and persistent optical auroral activity, notably during the presence of discrete auroral arcs; correlation levels of up to 74% and 63% were found at the atomic oxygen 557.7 nm and 630.0 nm wavelengths respectively (with statistical p-values of zero). From Tables 6.2 & 6.3 it may be observed that the majority of optical auroral activity in the study occurred around magnetic midnight and then at magnetic dusk, when it is likely that South Pole station was positioned around the pole-ward boundary of the auroral oval. Correlation was generally lower during periods of diffuse aurorae and dynamic wisp structuring as the statistical outcome became more sensitive to limitations of the tracking method. It is expected that the stronger the emission intensity, the higher the rate of local recombination and therefore likelihood of scintillation-producing irregularities. In general the 557.7 nm emissions correlated more closely with σ_φ than those at 630.0 nm, but this was likely due to the tracking method's effectiveness at two emission wavelengths of different characteristic intensity. Refinement of assumed altitude shells and spatial and temporal image filtering might help to improve the cross correlation statistics in future applications, and increased image exposure times would allow better detection of low level 630.0 nm emissions associated with polar cap patch irregularities. A conditional probability analysis of all data points revealed a general trend, namely those higher values of emission intensity corresponded with more elevated levels of σ_φ index. An increased focus on individual satellite tracks for specific auroral events is a useful development in terms of understanding the physical mechanisms present when a GPS receiver is experiencing scintillation.

Amplitude fading has not been investigated here, as general levels of the S_4 index (based on a normalized average of the signal carrier-to-noise power) appeared low on initial inspection. *Smith et al.* [2008] showed that analysis of the signal sampled at 50 Hz is generally required for observing the short duration signal fading associated with auroral arcs at high latitudes. The moderate levels of phase scintillation observed in this case study (σ_φ up to ~0.6 radians) were not sufficient to cause any significant signal tracking problems for the GPS scintillation receiver. An upcoming study will examine high temporal resolution GPS phase data (50 Hz) to help determine the physical source of the scintillation during optical auroral events. In conclusion, optical images of the aurorae from the South Pole have shown to be a useful spatial and temporal indicator of GPS phase scintillation during intense and persistent auroral activity, most notably in the presence of discrete arcs at the auroral boundary.

6.5 Summary

This chapter has presented the first results from an experimental setup at the geographic South Pole using a collocated all-sky imager (ASI) and GPS scintillation receiver. Its purpose was to investigate the usability of optical emission images as a proxy indicator of ionization structuring due to particle precipitation in the Antarctic. A collection of auroral events during Antarctic winters in 2010 and 2011 has been examined. This is the first time that multi-wavelength optical emission images have been compared with scintillation measurements in this way, including the high altitude red aurora (atomic oxygen 630.0 nm line at 200 km). Importantly the study has yielded the first statistical evidence highlighting the previously assumed relationship between the aurorae and GPS signal propagation. The observation of dual wavelengths facilitates a useful level of height discrimination in determining the altitude of the direct ionization causing phase scintillation. To complement the Antarctic studies of Chapters 5 and 6, Chapter 7 next investigates the current capabilities of tomographic imaging in the Arctic latitudes.

7 Arctic imaging

This chapter switches focus from the Antarctic to the Arctic ionosphere. In recent years the number of ground-based GNSS receivers has increased in and around the Arctic Circle. Historically the sparse and uneven distribution of these sites has been one of the main challenges in producing reliable tomographic images of the high latitude ionosphere. The purpose of this study is to profile the current capabilities of the MIDAS tomography tool in the Arctic, with an emphasis on resolving the auroral oval – an important component of the high latitude ionosphere. The results present the first tomographic images of the auroral oval, which are verified using particle spectrometer measurements and ultra-violet images from a low-Earth orbit satellite. A simultaneous plasma patch break-off event is also captured in both hemispheres for the first time, attributed to a balanced forcing of the magnetosphere during solar wind compression at equinox.

7.1 Introduction

Ionospheric storm studies in the Arctic and, more recently, the Antarctic have successfully used GPS tomography in resolving polar cap plasma patches and Tongues of Ionization (TOI) [*Bust et al.*, 2007; *Bust & Crowley*, 2007; *Pokhotelov et al.*, 2010; *Yin et al.*, 2009; *Spencer & Mitchell*, 2007; *Kinrade et al.*, 2012]. There are, however, few reports of auroral oval TEC being identified by ionospheric tomography routinely, despite the method's potential to do so.

The auroral oval is an important component of the high latitude ionosphere, Above 70% of precipitation power, one of the main sources of energy input at high latitudes, is distributed as diffuse aurora following ionization in the E and F regions [*Newell et al.,* 2009]. It marks the boundary point between closed and open geomagnetic field lines, and its demarcation can indicate the severity of space weather events and provide information to radio communication operators. There are significant efforts to estimate the near-real time auroral oval position in the absence of satellite global imagers (see Section 3.1.2), but these composite and model-based methods could be complemented by the addition of wide area ionospheric electron density maps that GPS tomography can provide. Tomographic images of the pole-ward wall of the mid-latitude trough have been verified on a regional scale using the EISCAT radar in Scandinavia [*Mitchell et al.*, 1995; *Meggs*, 2005; see Section 3.1.2]. At this point, however, there have been no published images of the entire auroral oval using ionospheric tomography, likely for two reasons. Firstly, recovery of auroral TEC in tomographic reconstructions requires ray path geometry from substantial receiver coverage, which has been historically poor around remote longitudes of the Arctic Circle. Secondly, electron density associated with the auroral oval is typically only a small contribution of total ionospheric TEC [*Coker et al.*, 1995], compared with F region plasma convection and dayside enhancement during storms. Auroral TEC levels sit between the ambient dayside maximum and nightside minimum levels (and are present even in the absence of ionospheric storms), and so a midrange treatment of colour scales has been applied in this experiment to pick out the auroral morphology.

7.2 Instruments & method

7.2.1 Geomagnetic indices and IMF parameters

Various indices are used in this study to profile the geomagnetic conditions during an ionospheric storm on 26 September 2011. The A_e and D_{st} indices are based on ground-based magnetometer measurements, and are described in Section 4.6.1. This study also uses a modified ACE data set from the OMNIWeb service, which projects IMF conditions at the ACE satellite position forwards to the magnetopause with verification from Earth-orbiting satellites [*King & Papitashvili*, 2005].

7.2.2 MIDAS TEC mapping

MIDAS is a set of tomographic algorithms to convert GPS Receiver Independent Exchange Format (RINEX) data into 3D time dependent maps of electron density (see Section 4.5). The earlier version of MIDAS [*Spencer & Mitchell*, 2007] used a model of the plasma convection to allow complete imaging of the polar regions [e.g. *Yin et al.*, 2009; *Pokhotelov et al.*, 2010]. In the current solar maximum the density of GPS receivers in the northern polar region is much improved compared to previous years (Figure 7.1a). Greenland and the European and North American sectors are now very well serviced, with only the oceans and Siberian sectors lacking in complete coverage for tomographic purposes. For comparison, the corresponding Antarctic receiver coverage is given in Figure 7.2, where new receiver locations are much more difficult to establish because of the extreme environment and lack of infrastructure. In the adapted version of MIDAS used in this experiment the algorithm uses GPS data and a regularisation procedure over a 2.5-hour window, weighted such that the data closest to the time of the image (at the centre of the window) has a greater importance on the final result. This allows reasonably wide-area coverage at ionospheric heights. Figures 7.1b and 7.2b show the intersection of the satellite to ground ray paths with the ionosphere at a height of 350 km above the surface of the Earth for the full 150-minute window. Details of MIDAS and its workings are given in Section 4.5 and [*Mitchell & Spencer*, 2003; *Chartier et al.*, 2013].

This study uses a custom colour mapping of TEC, which uses an arbitrary mid-point of 20 TECU in a red-white-blue scheme. Inspired initially by maps of ocean temperature changes, its use here provides a simple but visually effective way of differentiating between photo-produced plasma on the dayside (red) and the quieter nightside ionosphere (blue). The TEC levels associated with auroral precipitation and patch convection are expected to lie somewhere between these levels, and so are highlighted in white in this mid-range colour scheme.

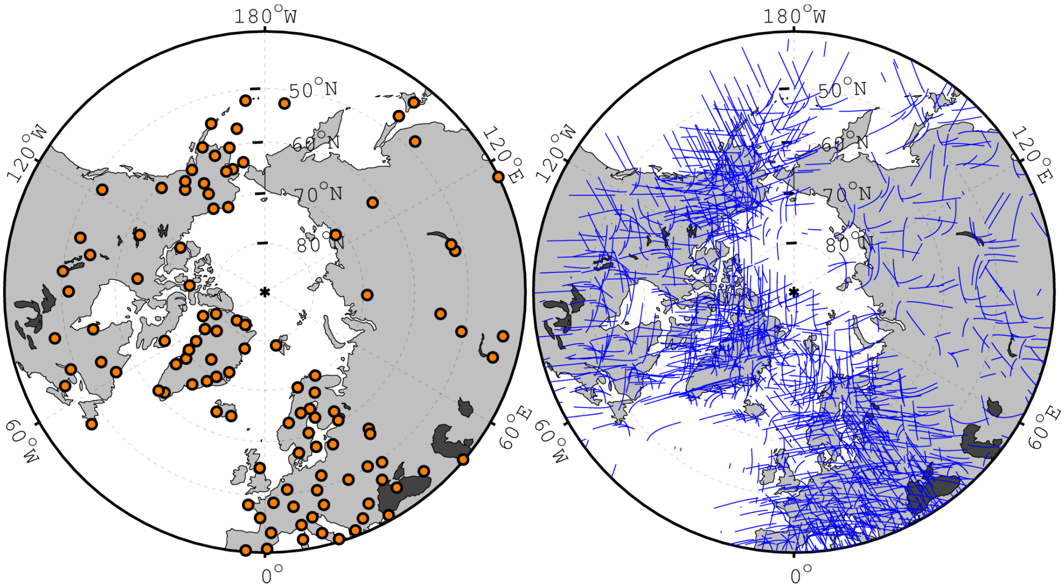

Figure 7.1 – Distribution of 120 optimally spaced Arctic ground-based GPS receivers used in this study during September 2011 (7.1a). 7.1b shows the typical ray path coverage within a 150 minute time window, plotted as pierce points at 350 km altitude (central window time 1600 UT 26 September 2011).

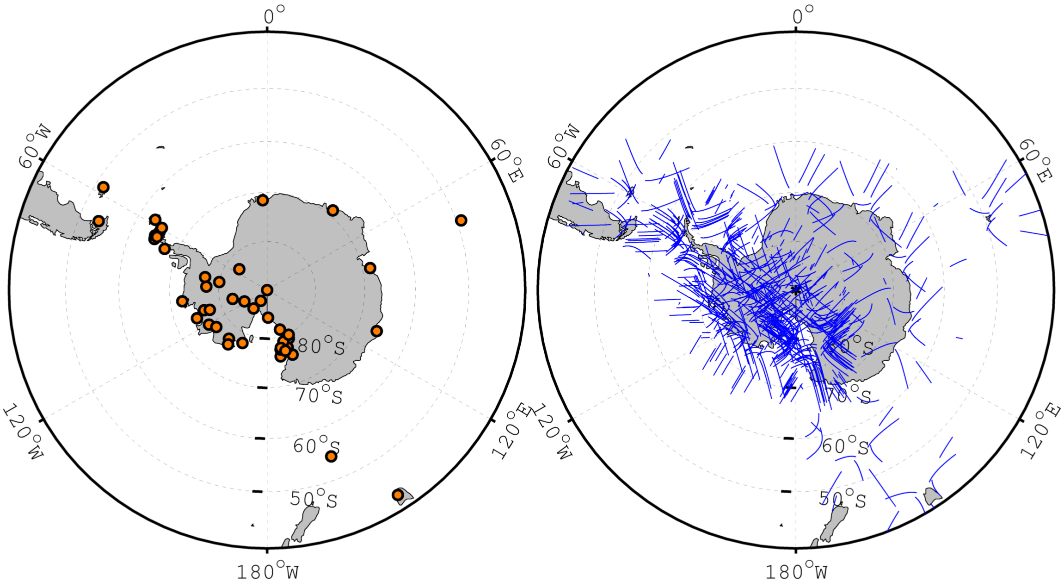

Figure 7.2 – Distribution of 50 Antarctic ground-based GPS receivers used in this study during September 2011 (7.2a). 7.2b shows the typical ray path coverage within a 150 minute time window, plotted as pierce points at 350 km altitude (central window time 1600 UT 26 September 2011).

7.2.3 SSUSI ultraviolet imaging & SSJ/4 particle spectrometer

The polar-orbiting DMSP satellites and their on-board SSJ/4 instruments are described in Section 4.6.3, and measure incoming electron and ion precipitation in the orbital zenith direction (i.e. above the satellite in a radial direction). The DMSP satellites also carry the Special Sensor Ultraviolet Spectrographic Imager (SSUSI), which captures time-integrated 'swath' images of ultraviolet emissions associated with the by-products of collisional ionization [*Huffman*, 1992]. The emissions at 135 mm are convenient because they are not saturated out by sunlight on the dayside. SSUSI looks in an earthward direction (i.e. the satellite footprint), and so the combination of SSUSI and SSJ/4 observations provides a convenient in situ and two-way indication of particle precipitation. The SSUSI data have only recently been publicly released, and provide some of the most complete images of the auroral oval now available from space.

7.2.4 Poker flat Incoherent Scatter Radar (PFISR)

The Poker Flat Incoherent Scatter Radar (PFISR) is located at 65.2° N, 147.5° W, and operates in the frequency band 449-450 MHz. ISR provides accurate altitude profiles of ionospheric electron density. The PFISR's auroral location makes it a useful instrument for validation of E and F region electron content present at times during this study, which uses observations from a vertical beam scan. The principles of incoherent scatter radar are explained in Section 4.6.2.

7.3 Results & analysis

7.3.1 Geomagnetic storm at equinox – 26 September 2011

A moderate geomagnetic storm event occurred on 26 September 2011 (K_p index reached up to 6.5), as evident from the geomagnetic and IMF parameters in Figure 7.3. GPS data availability was consistent in both hemispheres throughout this equinox event, and so the storm provided a useful case study subject for this tomographic imaging experiment. Referring to Figure 7.3, the initial phase of the geomagnetic storm (indicated by positive D_{st} values of up to ~30 nT) occurred between 12-15 UT, during magnetospheric compression from a CME. The main storm phase then persisted until recovery the next day, with D_{st} values dropping to ~100 nT throughout the afternoon and evening (UT). Peaks in the A_e index indicate periods of enhanced auroral electrojet current flows (easterly and westerly), typically associated with particle precipitation and expansion of the auroral boundary. The IMF measurements show that the initial phase of the storm occurred largely during B_z+ orientation with B_y+/- switching (12-14 UT), with the main phase later influenced by periods of pronounced B_z+/- switching.

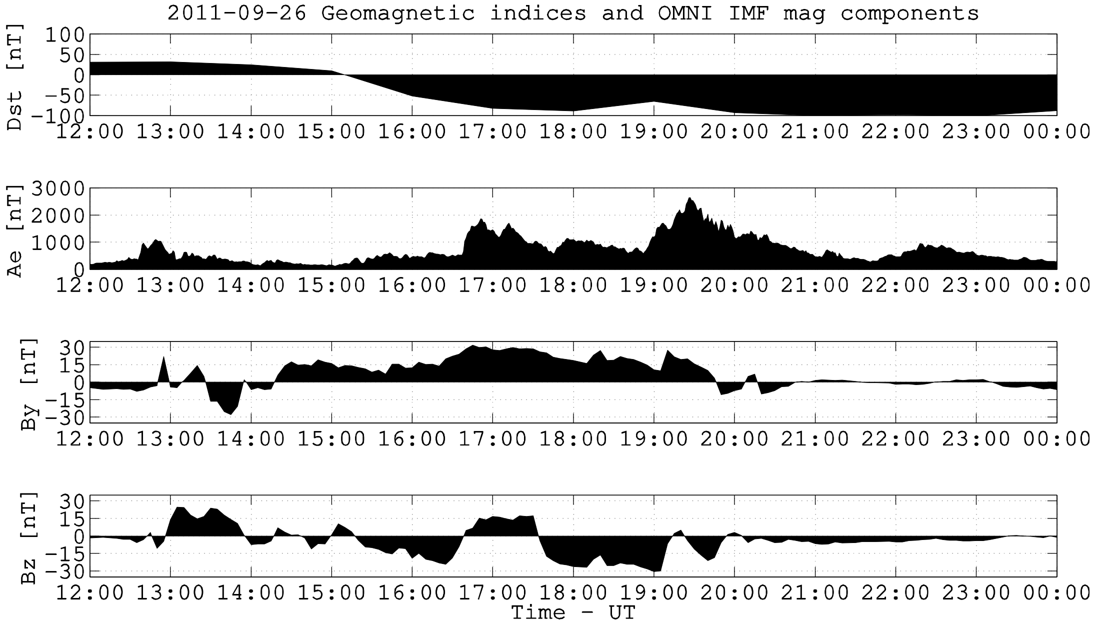

Figure 7.3 – 7.3a and 7.3b show the geomagnetic indices D_{st} (equatorial stations, hourly) and A_e (auroral stations, 1 minute values) respectively, during the afternoon of 26 September 2011. 7.3c and 7.3d show OMNI projections of the IMF B_y and B_z components respectively, which are time-shifted to the near-Earth geospace.

7.3.2 Auroral oval

Figure 7.4 shows the MIDAS electron density maps reintegrated vertically to show TEC across the entire polar region. Images are shown every 10 minutes. It should be noted that the images are not truly independent over that short timescale because the data from the entire window are weighted into the reconstruction. Nevertheless, there are differences in the consecutive images that reveal a sequence of events. Each image is orientated with local noon at the top, and the colour scale is kept constant across the sequence. On the dayside a large-scale enhancement is seen as expected in the sunlit ionosphere (up to 40 TECU). Looking pole-ward, the ionosphere enters darkness and the usual lower densities are found. The striking feature is the consistent ring of plasma shown with TEC values around 20 TECU. This is especially evident in the strong enhancements on the nightside and it is also interesting to note that the ring in not centred on the geographic pole but rather the geomagnetic, as expected for a genuine auroral feature. Furthermore, it is notable that the ring expands in the time sequence, evident with nightside enhancements in the Asian and Russian sectors moving equator-ward by the later images.

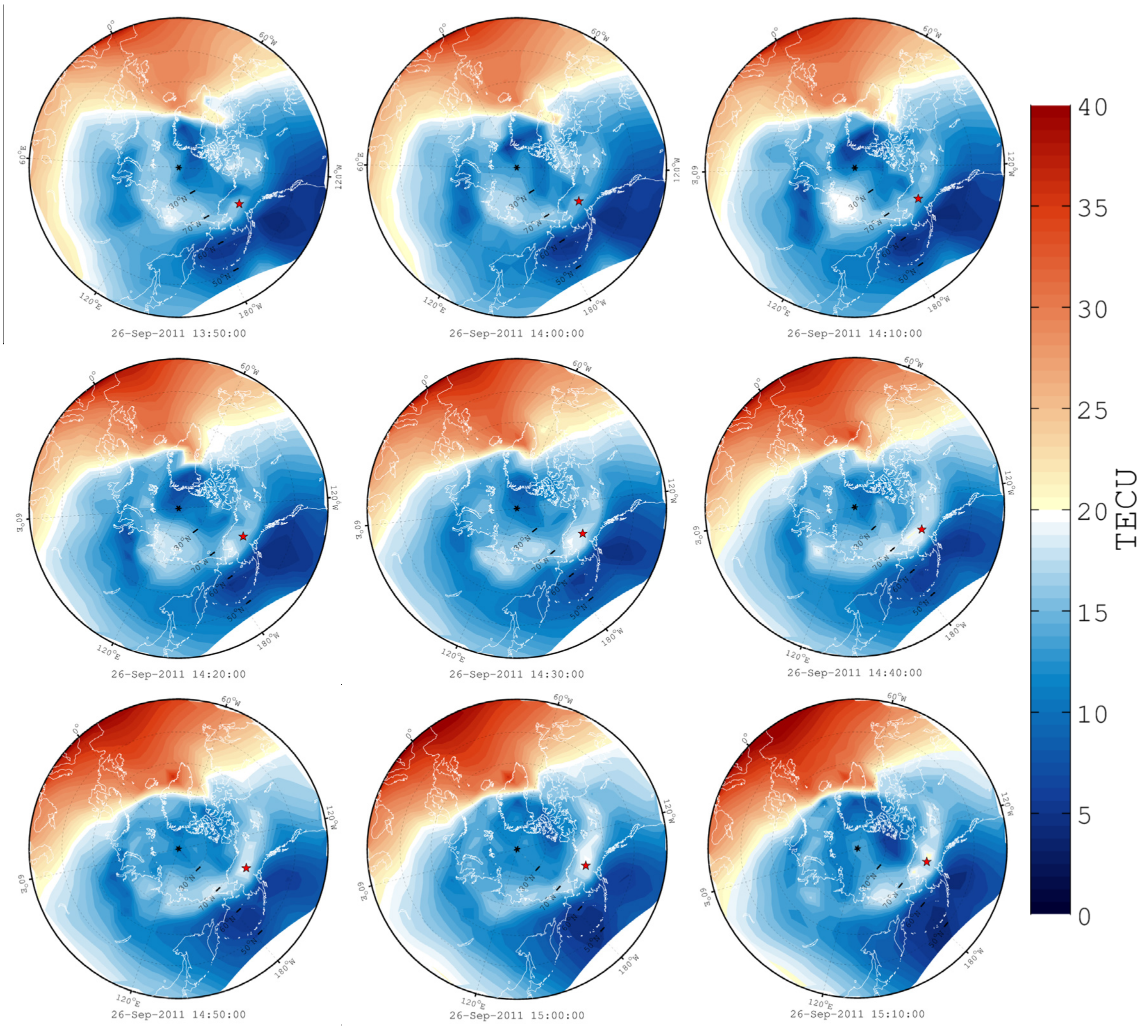

Figure 7.4 - A series of TEC reconstructions during 1350-1510 UT, orientated with local noon at the top of each image. A blue-white-red colour scale has been used to highlight the midrange TEC between dayside and nightside plasma levels. The red star marker indicates the position of the Poker Flat ISR. A ring feature was discernible throughout the period, located around the typical position of the auroral oval. Although not markedly pronounced from the general background TEC levels, the ring was persistent in time once formed, evident between 1330-1510 UT. TEC values associated with the ring ranged from ~15-25 TECU, although the longitudinal distribution of TEC was uneven and variable in time.

The position of the auroral oval imaged in Figure 7.4 can be verified using the SSJ/4 and SSUSI instruments on the Defence Meteorological Satellite Program (DMSP) satellite F18. Figure 7.5 shows the ground track of F18 superimposed on a MIDAS TEC map at 1340 UT, alongside a time plot of the total electron and ion energy fluxes during the dusk-dawn pass. Two main bands of precipitation energy flux correspond with the auroral oval intersected in the TEC map. This form of verification indicates that the auroral latitudes were subject to increased energetic particle flux during the lifetime of the TEC ring feature in the MIDAS images, which corresponded with the initial magnetospheric compression stage of the storm.

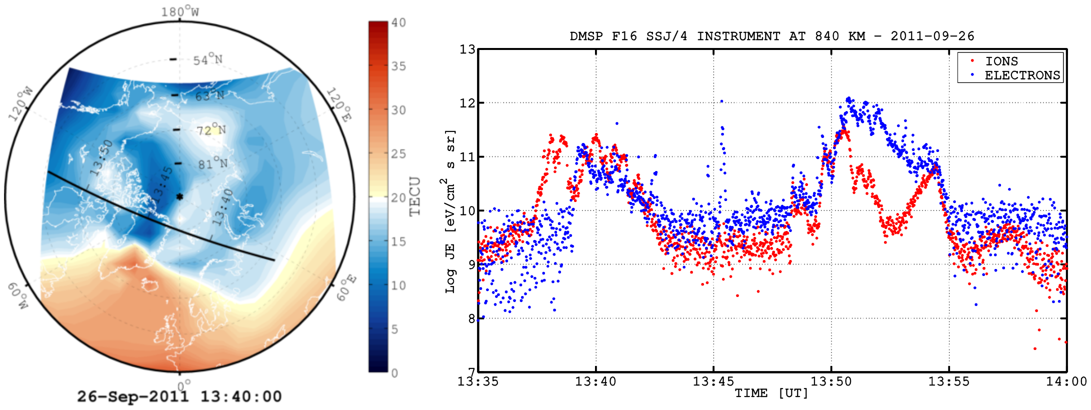

Figure 7.5 - The ground track of polar-orbiting satellite DMSP F16 during a dusk-dawn pass across the auroral oval and polar cap, overlaid on a MIDAS TEC image at 1340 UT (7.6a, orientated with local noon at the bottom of this image). The total electron and ion energy fluxes during the pass are shown in 7.6b, as measured in the zenith direction by the SSJ/4 instrument at ~840 km altitude. Two main bands of precipitation energy flux correspond with the auroral oval sectors imaged in the TEC map.

Figure 7.6 shows an ultraviolet image from SSUSI at 1429-1452 UT, together with the derived mean electron energy and peak E-region electron density images. These images reveal the track of the oval to pass over the North American sector, Greenland, and northern Russia. At this time step the oval can be extrapolated visually to pass over Alaska and the Chukchi Sea into the Siberian sector north of Asia. Appendix 10.3 provides a sequence of further UV images in support of this. Comparing to the image at 1440 UT in Figure 7.3, it would seem that the TEC enhancement is consistent with the region of increased E-region density derived from the UV emissions. The TEC enhanced region is slightly broader but is consistent with the UV image in Figure 7.6a. Over the American sector the UV band is distinct with enhancements right along the northern regions of Canada. Again, this is broadly consistent with the white areas of TEC enhancement on the maps of Figure 7.4.

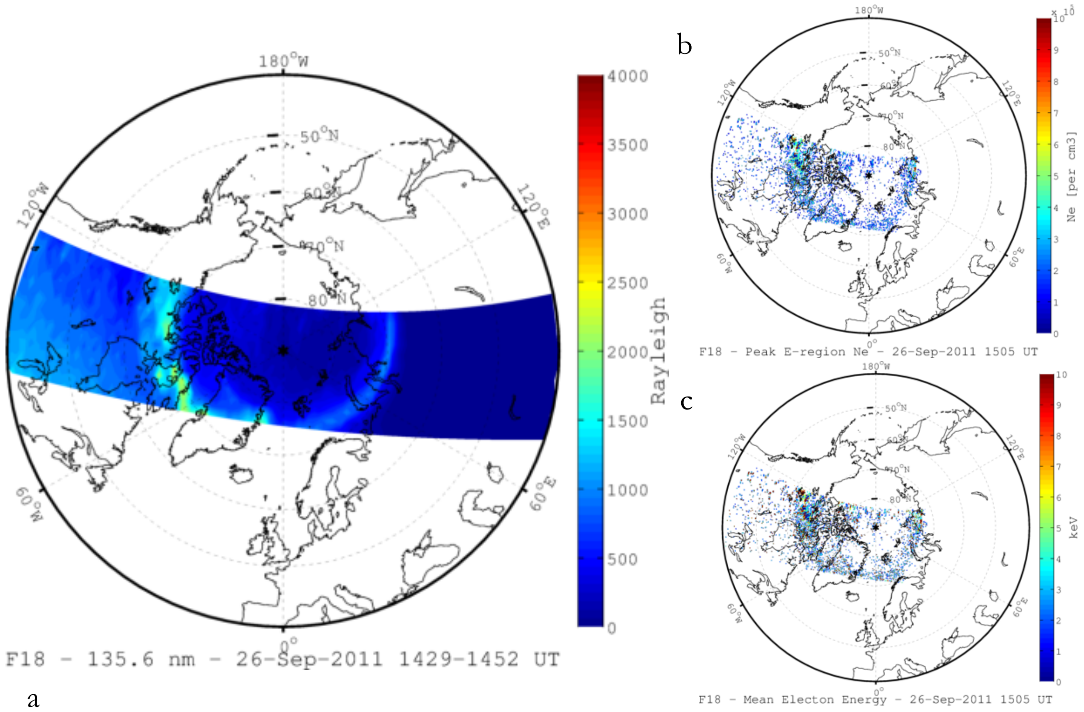

Figure 7.6 – A composite-scan 135.6 nm UV photometer image from the SSUSI instrument on DMSP F18 (7.6a), and the derived mean electron energy (7.6b) and peak E-region electron density (7.6c). The images clearly show the auroral oval position over North America, Greenland and northern Russia.

Having established the position of the oval from the other available instrumentation it is now of interest to investigate the contribution of E and F region electron density to the TEC enhancement. Focussing on the Alaska region, the PFISR was operating and measuring vertically above the radar. Figure 7.7 is an altitude-time plot of the PFISR electron densities throughout the day of interest. This vertical beam scan series clearly shows the onset and early stages of the storm as it impacted the ionosphere above Poker Flat (Alaska), with sudden enhancement of the N_e throughout the E and F region altitude ranges after ~1030 UT (approximately midnight local time in Alaska). High levels of electron density persisted at low altitudes after the initial storm onset. Of particular interest is the significant enhancement of N_e at D and E region altitudes (up to $5x10^{11}$ m^{-3}) during ~1230-1330 UT (local midnight-dawn sector), when the MIDAS images show enhancement of TEC around the entire auroral oval. Taking the maximum E-region (below 200 km) density value of $5x10^{11}$ m^{-3} measured by the radar, and integrating this over an arbitrary altitude range of 50 km equates to ~2.5 TECU. The ionospheric images of Figure 7.4 show the ring enhancement region across Alaska to have TEC values of around 20 TECU higher than the nominal values from the region outside of the oval. This implies that the auroral ring feature imaged by MIDAS during this storm is composed of electron density contributions from both the E and F regions.

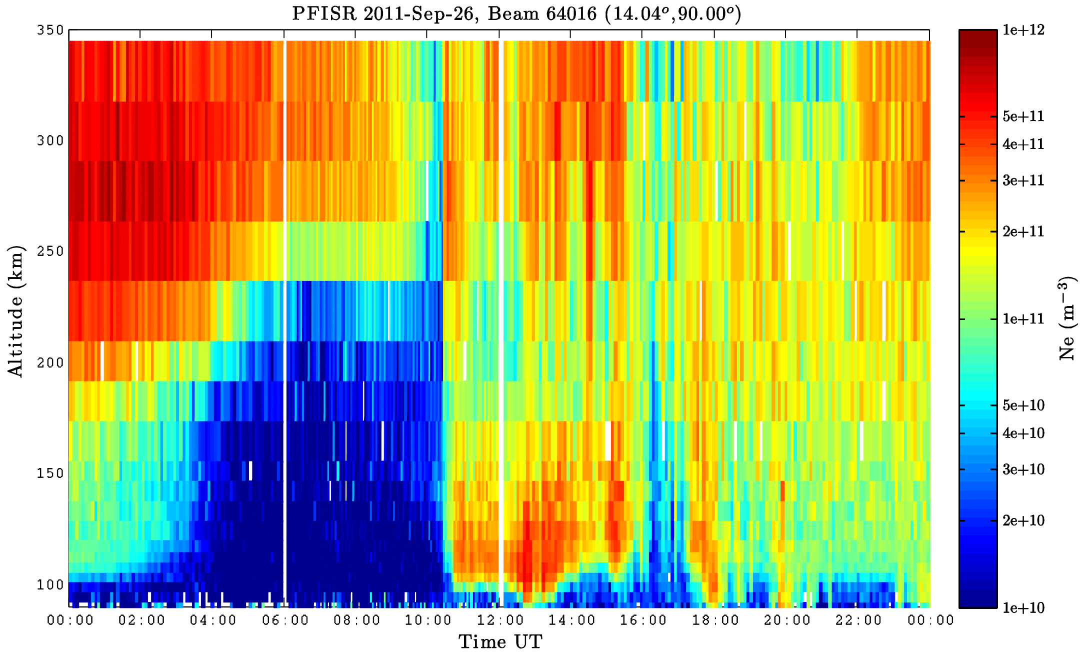

Figure 7.7 – Time-altitude plot of electron density (N_e) from the Poker Flat Incoherent Scatter Radar (PFISR), which is positioned at the auroral boundary (MLAT 65.4°). The position of the radar is also marked with a red star in Figure 7.4. The onset of the storm is clearly visible at ~1030 UT, when E and F region electron densities were suddenly enhanced lasting several hours.

7.3.3 Polar cap patches

Two plasma patch events were revealed in this study, occurring during the main phase of the geomagnetic storm. Figure 7.8 is a sequence of MIDAS images showing the lifetime of the first patch over several hours, which started with the formation of a TOI over North America at ~1550 UT. Each image in these patch sequences is orientated with a fixed geographic frame to emphasise the movement of the patches. The 0° longitude line is at the foot of each image, and time steps vary between 10-40 minutes for conciseness. By 1700 UT, TOI plasma had reached Greenland with TEC levels of up to 40 TECU. The patch structure then separated from the dayside plasma at 1710 UT, and propagated in an anti-sunward direction across Greenland. Interestingly and referring to Figure 7.3, the IMF B_z polarity at the magnetopause switched significantly from negative to positive during this patch event at ~1640 UT.

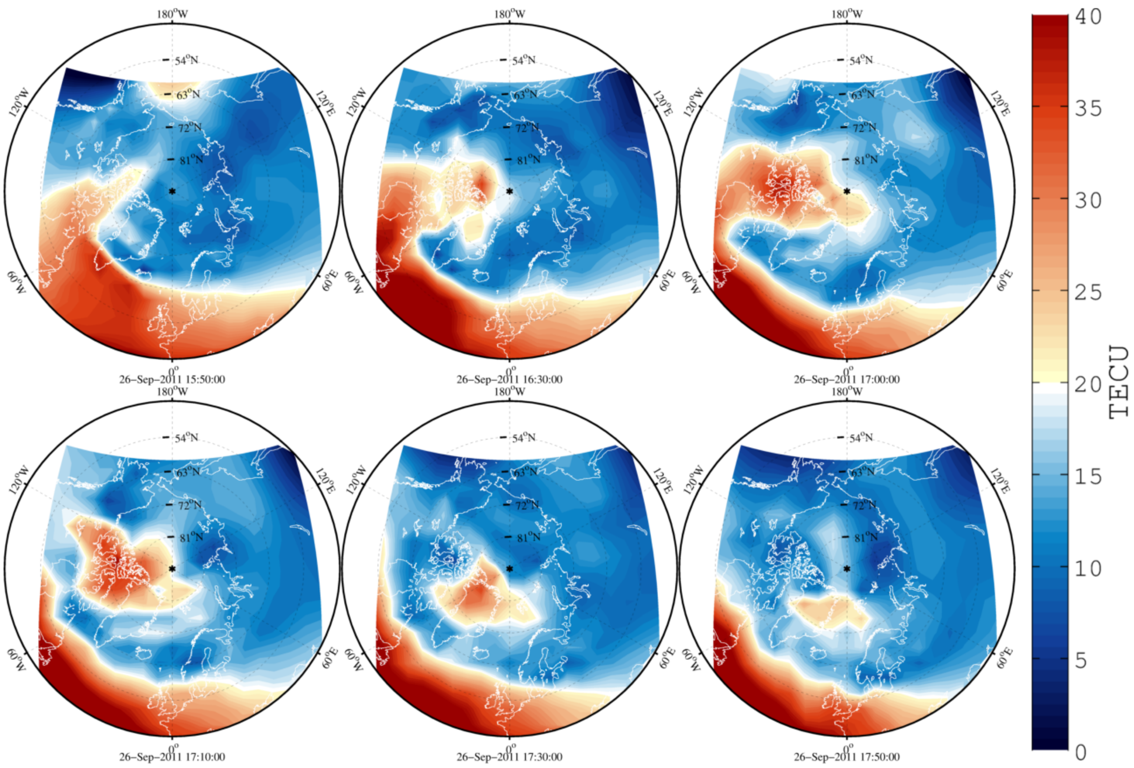

Figure 7.8 – A sequence of MIDAS TEC images spanning the times 1550-1750 UT, showing the formation and convection of a plasma patch during the main phase of the 26 September 2011 storm. These images are orientated in a fixed geographic frame to emphasise the patch movement. Time steps vary between 20-40 minutes.

Figure 7.9 is similar to Figure 7.8, and shows the lifetime of the second patch event during 1830-2000 UT. The breakoff of this patch from the dayside plasma occurred at ~1910 UT, at approximately the same time as a brief positive excursion of IMF B_z polarity from negative to positive (see Figure 7.3). Figures 7.8 and 7.9 indicate that the two patches travelled in a similar convective pattern and with similar speeds, developing over North America and being drawn over the Polar Cap and across Greenland before dissipating north of Europe.

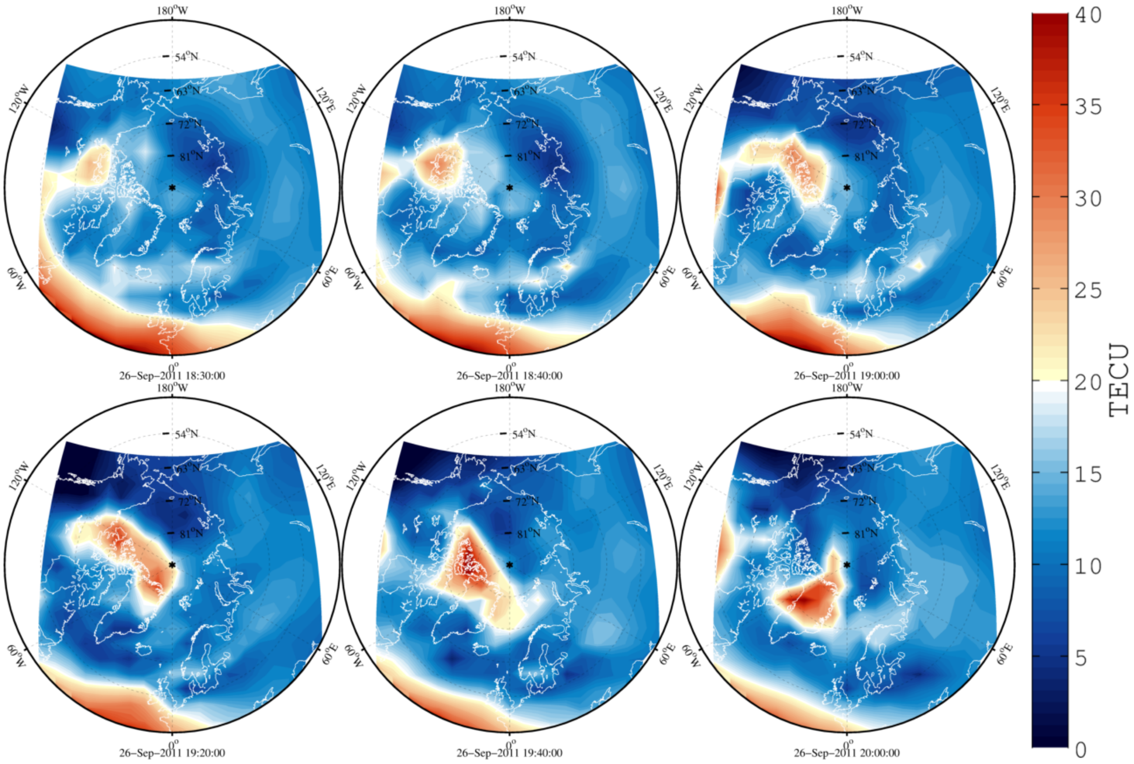

Figure 7.9 – A sequence of MIDAS TEC images spanning the times 1830-2000 UT, showing the formation and convection of a plasma patch during the main phase of the 26 September 2011 storm. These images are orientated in a fixed geographic frame to emphasise the patch movement. Time steps vary between 10-20 minutes.

In complement to the main Arctic focus of the study, MIDAS reconstructions were also performed over the Antarctic during the same geomagnetic event (see data coverage in Figure 7.2). It is useful to contrast the current high-latitude capabilities of MIDAS in both hemispheres, following the Antarctic experiment of Chapter 5. Figure 7.10 shows two simultaneous TEC maps from the Arctic and the Antarctic. Note the reduced grid extent of the Antarctic image due to the limited site distribution. There was no evidence of an auroral oval feature in the Antarctic during the storm. It is likely that the Antarctic site distribution and data coverage remains insufficient for the reconstruction of such subtle TEC structuring. However, at the same time as the second patch break off event in the Arctic (detailed in Figure 7.9), a patch structure also formed in the Antarctic. The symmetrical or asymmetrical response of both hemispheres to specific geomagnetic events is difficult to determine as the magneto-ionospheric linkage is complex, but in this case tomography has revealed an interesting simultaneous response in the form of plasma patch formation. It is plausible that the occurrence of the geomagnetic storm at equinox led to a balanced forcing of the magnetospheric compression and subsequent ionospheric linkage in both hemispheres. This is an interesting development for high-latitude GPS tomography, and demonstrates its value as an observational tool in profiling the ionosphere's behaviour on a global scale.

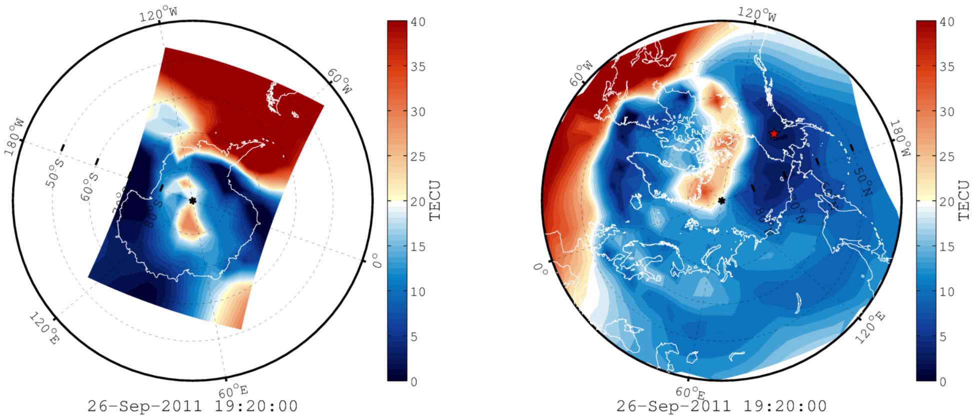

Figure 7.10 –MIDAS TEC maps over Antarctica (7.10a) and the Arctic (7.10b), showing simultaneous plasma patch break-off events at ~1920 UT. Local noon is located at the top of each image. Note the comparably reduced grid extents of the Antarctic image because of the limited ground-receiver coverage in the region.

7.4 Summary

This Chapter has tested the current capability of MIDAS in the Arctic latitudes, during the moderate geomagnetic storm of 26 September 2011. An auroral oval enhancement was identified using maps of the vertical TEC that lasted for several hours during the initial onset of the storm. The maps were verified using the SSJ/4 particle spectrometer and SSUSI UV imager on board the polar-orbiting DMSP F18 satellite. Vertical beam scans from the Poker Flat ISR (PFISR) indicated that the TEC enhancement was formed of electron density contributions in the E and F regions. This is the first time that the auroral oval has been imaged in its completeness using GPS tomography. Two distinct plasma patches were also imaged during the storm, with their break-off from the dayside plasma likely triggered by polarity switching of the IMF B_z component. A simultaneous patch breakoff event was also imaged in the Antarctic ionosphere, revealing evidence of a symmetrical hemispheric response during equinox. The current distribution of GPS receivers in the Arctic allows MIDAS to reconstruct discrete high latitude ionospheric structures, without the use of plasma motion modelling.

8 Conclusions & future work

In this thesis the effects of the high-latitude ionosphere on GNSS signals were investigated. At the start of the project there was little evidence to quantify their severity at high latitudes. The research used a combination of two core techniques, GPS tomography and scintillation monitoring, to investigate the effects of geomagnetic storms and auroral activity in the Antarctic and Arctic ionosphere.

Several experiments were undertaken to quantify the amount of phase scintillation in the Antarctic over an extended period around solar maximum. A case study approach was adopted, using multiple ionospheric instruments to relate individual scintillation events observed by GPS receivers to their ionospheric source. These events were related to the larger Sun-Earth system using geomagnetic indices and solar wind measurements. The work aimed to further the use of GNSS observations as a tool to investigate the ionosphere at high latitudes, by demonstrating new techniques for mapping the polar ionosphere. This section summarizes the findings of the work, and how the research aims have been met.

Ionospheric imaging is less established in the Antarctic than in the Arctic because of a historic lack of ground receivers and their uneven distribution around the continent. It is also difficult to obtain boundary data from sites off the main continental region, and those that are there typically provide only intermittent observations. It is important to obtain verification of TEC images in the Antarctic and as there is little or no ISR data available compared to the Artic in situ measurements from polar orbiting satellites have proven to be effective for this purpose. A multi-instrument approach has been a key theme of the thesis. The last decade has seen an increase in campaign-based and permanent receivers, and online collective database facilities have improved. One aim of the research was to build on the success of recent Antarctic tomographic imaging work (that used a model for plasma motion) with MIDAS, using more receivers and comparison with a second tomographic tool, IDA4D.

Plasma patches are known to be associated with GPS scintillation because of their high drift velocity, TEC gradients and structural breakdown of electron density at their edges.

The breakoff transition from TOI to patch, and their persistence in the nightside ionosphere, are also interesting aspects of patch study, as the responsible processes are currently attributed to a mix of instability mechanisms with little definition of which dominates and under what IMF conditions. The ability to resolve patches in the Antarctic using tomography is based really on a single paper [*Ping et al.*, 2009], following progress in the Artic from *Pokhotelov et al.* [2010], *Mitchell et al.* [1995], and *Smith et al.* [2008], so this research also aimed to build up this knowledge base by studying disturbed times and verifying patch activity using a combination of tomography and scintillation monitoring.

Chapter 5 combined tomographic images and GPS scintillation measurements for the first time in the Antarctic to investigate the ionosphere's response to a geomagnetic storm. On 5 April 2010 a coronal mass ejection produced a travelling solar wind shock front that impacted the Earth's magnetosphere, producing the largest geomagnetic storm of 2010. The storm resulted in a prolonged period of phase scintillation on Global Positioning System (GPS) signals in Antarctica. The scintillation began in the deep polar cap at South Pole just over 40 minutes after the ACE satellite at the first Lagrangian orbit position recorded the shock front impact. Scintillation activity continued there for many hours. On the second day significant phase scintillation was observed from an auroral site (81° S) during the post-midnight sector in association with a substorm. Particle data from polar orbiting DMSP satellites provided indication of electron and ion precipitation into the Antarctic region during the geomagnetic disturbance. TEC maps showed enhanced electron density being drawn into the polar cap in response to southward turning of the interplanetary magnetic field. The plasma enhancement structure then separated from the dayside plasma and drifted southward. Scintillation on the first day was coincident spatially and temporally with both a plasma depletion region in the dayside noon sector, and in the dayside cusp. On the second day scintillation was observed in the nightside auroral region, and appeared to be strongly associated with ionospheric irregularities caused by E-region particle precipitation.

It is a challenge to identify areas of small-scale (a few km) irregularities in the ionosphere, as tomography can only provide large-scale (hundreds of km) resolution of electron density and TEC, and an indication of where breakdown of TEC gradients and patches might occur. A unique experiment with collocated optical and GPS instrumentation at the geographic South Pole allowed the direct comparison of auroral emissions and GPS phase scintillation. The use of optical emissions as a proxy for localised and field-aligned ionization is a reasonable assumption, and one that has been made in Arctic case studies observing GPS scintillation in the presence of auroral arcs. The experiment in Chapter 6 aimed to provide a more definitive set of statistical results in support of this relationship, so that existing and future ASI imaging sites might be used routinely to monitor scintillation activity. There is also the possibility of using auroral images in future selective satellite rejection schemes to improve the robustness of a precise position or timing solution during times of auroral activity.

Chapter 6 examined optical auroral events during 2010-11 and reported spatial and temporal correlations with GPS L1 phase fluctuations using instrumentation located at South Pole Station. An all-sky imager provided a measure of optical emission intensities ([OI] 557.7 nm and 630.0 nm) at auroral latitudes during the winter months. A collocated GPS antenna and scintillation receiver facilitated superimposition of auroral images and GPS signal measurements. Correlation statistics were produced by tracking emission intensities and GPS phase scintillation indices at E and F-region heights. This was the first time that multi-wavelength auroral images have been compared with scintillation measurements in this way. Correlation levels of up to 74% were observed during 2-3 hour periods of discrete arc structuring. Analysis revealed that higher values of emission intensity corresponded with elevated levels of phase scintillation index. The study has yielded the first statistical evidence supporting the previously assumed relationship between the aurorae and GPS signal propagation, and is a particularly strong result of the thesis. The probability of scintillation-induced GPS outages is of interest for commercial and safety-critical operations at high latitudes. The results from Chapter 6 indicate that image databases of optical auroral emissions could be used to assess the likelihood of multiple satellite scintillation activity. The use of multiple wavelength emission images also provided a level of altitude discrimination, as at times the scintillation correlated with only the red 630.0 nm emissions in the F-region, and not the green 557.7 nm emissions in the E-region.

GNSS receiver distribution is now extensive in most sectors of the Arctic Circle, with the exception of the Russian/Siberian continent and oceans. Greenland, Scandinavia, North America and Canada are now populated with approximately 140 permanent and campaign GPS receivers (UNAVCO database holdings above 60° latitude during May 2013). Several receiver stations do exist along the fringes of Russia and Siberia, providing boundary information to tomographic imaging studies in the Arctic. Tomographic imaging in the Northern hemisphere is well developed, and several large storms have been profiled within the last decade that display significant TOI and patch activity. Despite this, it remains difficult to predict the ionosphere's response to disturbed geomagnetic conditions. Storm events in particular are highly dynamic and drive processes that occur over multiple spatial and temporal scales, with tomographic imaging being able to resolve only large-scale electron density structuring (5 km voxels and ten minute time steps at the upper end of its current capability, with typical MIDAS runs at 300 km voxel size). The auroral oval is an important feature of the high latitude ionosphere, being the boundary between open and closed geomagnetic field lines, and a reactive indicator of storm intensity as it expands and contracts. The polar cap and equator-ward trough boundaries are also areas of expected large-scale TEC gradients, and are therefore of interest for scintillation monitoring. Determining the oval's complete morphology is more of a challenge today than it was in the 1980s, when dedicated satellites were looking down on the entire globe with UV imagers to profile the oval and its substorm behaviour. Oval position is now determined on a more assimilative basis, using a combination of polar-orbit satellite particle measurements and statistical shape-fitting based on historical UV images and their boundary information.

Chapter 7 aimed to test the current capabilities of the MIDAS tomography tool at Arctic latitudes during the moderate geomagnetic storm of 26 September 2011. The first images of the complete auroral oval morphology using GPS tomography were presented. The oval enhancement was identified using maps of the TEC, which was present during the initial impact phase of the storm. This experiment presented the case for ionospheric tomography contributing towards a more complete multi-instrument picture of the northern auroral oval and its boundary extents, with verification from the ultraviolet spectrograph and particle spectrometer instruments on board the DMSP satellites. This is the first time that GPS tomography has revealed the effects of particle precipitation so clearly as to reveal the entire auroral oval. Previous studies have shown polar cap patches in TEC and particle precipitation in signatures from GPS scintillation. The importance of this research is that the method may have the potential to be developed into a technique for automatically detecting the oval position. This will require further work on image thresh-holding to reveal small but significant enhancement over the background TEC values that lie in between dayside and nightside plasma levels.

The Arctic imaging study in Chapter 7 also revealed an almost exactly simultaneous patch break-off event in the both Arctic and Antarctic. The question of hemispheric symmetry or asymmetry in ionospheric behaviour is a popular open topic in the literature because of its implications to magneto-ionospheric linkage. The dedicated high-latitude TEC maps provided by tomography here have offered a unique perspective in this respect, as opposed to full global reconstructions that have limited resolution at high latitudes. The simultaneity of the event was attributed to the geomagnetic storm occurring during equinox, when the compression force of the incident solar wind was likely to have been balanced across both hemispheres. It is also important to note that high latitude tomography can now capture the lifetime of plasma patches without the need of plasma motion modelling, particularly with the Arctic data coverage. This is a significant step forwards. The reconstruction grid size in the Antarctic still needs to be limited at times because of the lack of boundary information, but patch movement is still resolved as illustrated in Chapters 5 & 7.

In summary, the key results of the research are:

- Antarctic and Arctic ionospheres have been imaged reliably using MIDAS without the need of plasma motion modelling.
- Ionospheric response features have been identified at different stages of storm development causing phase scintillation in Antarctica.
- Complete auroral oval TEC structure and simultaneous patch break-off events have been imaged for the first time using ionospheric tomography.
- First statistical evidence has been obtained for the proxy spatial and temporal relationship between auroral optical emissions and GPS phase scintillation.
- Images of different optical emission wavelengths can provide altitude discrimination of scintillation source structuring.

In terms of future work, the results of this thesis can form the basis of some potentially very interesting studies. From a physics perspective, a long-term inter-hemispheric comparison study would help to answer the question of polar symmetry during geomagnetic storms. Multiple case studies could be performed during past and future periods of geomagnetic activity, which would help to define the relationships between plasma circulations and patch generation with IMF orientation. It would also be interesting to compare winter and summer hemispheres, and establish the extent of the sunlight coverage effect on the high latitude ionosphere.

Current research efforts at the University of Bath aim to mathematically improve MIDAS electron density resolution in areas of sparse and uneven GPS data coverage. The Antarctic region would be a useful test bed for this research, as the ability to extract weak TEC features such as the auroral oval is currently limited by the receiver distribution. The Antarctic receiver distribution is unlikely to improve significantly in the near future because of the remote nature of its environment, so novel approaches to improving the quality of ionospheric tomography in the region are valuable.

Since the completion of this work, the all-sky imager at South Pole has been upgraded to output images with a time resolution of 1 second, an improvement on the current 24-second interval for respective wavelengths. The new ASI-GPS imaging method presented in Chapter 6 could be improved to output correlation statistics with higher temporal resolution, combining the 1 second images with 50 Hz GPS scintillation data available from the receiver. A more extensive study could also consider using additional emission wavelengths available from the ASI, to investigate whether the scintillation source structuring can be attributed to a more specific altitude range than E or F region.

Automatic detection of the auroral oval using GNSS signals could prove to be a low-cost and routine way to monitor the position and boundaries. The advantage is that GNSS data is generally free to use and widely available. Further research is still required to routinely verify the presence of the auroral oval in MIDAS tomographic images, but an extensive verification study using the SSUSI UV image database and images from the THEMIS array of ASIs would be a significant step.

9 References

AARONS, J. (1982), Global morphology of ionospheric scintillations, *Proceedings of the IEEE*, 70(4), pp. 360-378.

AARONS, J., B. Lin, and M. Mendillo (2000), Global Positioning System phase fluctuations and ultraviolet images from the Polar satellite, *J. Geophys. Res.*, 105(A3), pp. 5201-5213, doi:10.1029/1999JA900409.

AKASOFU, S. –I. (1964), The development of the auroral substorm, *Planetary and Space Science*, 12(4), pp. 273-282, doi:10.1016/0032-0633(64)90151-5.

AKASOFU, S. –I. (1974), A study of auroral displays photographed from the DMSP-2 satellite and from the Alaska meridian chain of stations, *Space Science Reviews*, 16(5-6), pp. 617-725, doi:10.1007/BF00182598.

ALFVÉN, H. (1942), Existence of electromagnetic-hydrodynamic waves, *Nature*, 150, Issue 3805, pp. 405–406.

ALFVÉN, H. (1943), On the existence of electromagnetic-hydrodynamic waves, *Arkiv foer Matematik, Astronomi och Fysik*, 39(2).

ANGER, C. D., A. T. Y. Lui, and S.-I. Akasofu (1973), Observations of the auroral oval and a westward traveling surge from the Isis 2 satellite and the Alaskan meridian all-sky cameras, *J. Geophys. Res.*, 78(16), pp. 3020–3026, doi:10.1029/JA078i016p03020.

AQUINO, M. et al. (2009), Improving the GNSS positioning stochastic model in the presence of ionospheric scintillation, *J. Geodesy*, 83, pp. 953-966, doi:10.1007/s00190-009-0313-6.

AUSTEN, J. R., S. J. Franke, C. H. Liu, and K. C. Yeh (1986), Applications of computerized tomography techniques to ionospheric research, *International Beacon Satellite Symposium*, 9-14 June 1986, Oulu, Finland, Proceedings, Part 1 (A87-50101 22-46), pp. 25-35.

BAKER, D. (1974), Rayleigh, the unit for light radiance, *Applied Optics*, vol. 13, issue 9, pp. 2160-2163, doi: 10.1364/AO.13.002160.

BARCLAY, L. W. (2003), *Propagation of Radio Waves*, 2nd Ed., The Institution of Electrical Engineers, London, UK, ISBN: 0-85296-102-2.

BASU, S., E. J. Weber, T. W. Bullett, M. J. Keskinen, E. MacKenzie, P. Doherty, R. Sheehan, H. Kuenzler, P. Ning, and J. Bongiolatti (1998), Characteristics of plasma structuring in the cusp/cleft region at Svalbard, *Radio Sci.*, 33(6), pp. 1885-1899, doi: 10.1029/98RS01597.

BASU S., K. M. Groves, Su. Basu, P. J Sultan (2002), Specification and forecasting of scintillations in communication/navigation links: current status and future plans, *J. Atmos. Sol-Terr. Phy.*, 64, pp. 1745-1754, doi:10.1016/S1364-6826(02)00124-4.

BENSON, R. F. (1960), Effect of line-of-sight aurora on radio star scintillations, *J. Geophys. Res.*, 65(7), pp. 1981–1985, doi:10.1029/JZ065i007p01981.

BENTON, C. J. and C. N. Mitchell (2011), Isolating the multipath component in GNSS signal-to-noise data and locating reflecting objects, *Radio Sci.*, 46(6), RS6002, doi:10.1029/2011RS004767.

BELCHER, D. P (2008), Theoretical limits on SAR imposed by the ionosphere, *IET Radar, Sonar & Navigation*, 2(6), pp. 435-448, doi: 10.1049/iet-rsn:20070188.

BENIGUEL, Y., J.-P. Adam, A. Bourdillon, and P. Lassudrie-Duchesne (2011), Ionosphere scintillation effects on navigation systems, *Comptes Rendus Physique*, 12(2), pp. 186-191, doi: 10.1016/j.crhy.2011.01.005.

BOOKER, H. G., J. A. Ratcliffe, and D. H. Shinn (1950), Diffraction from an irregular screen with applications to ionospheric problems, *Phil. Trans. R. Soc. London*, *Ser. A*, 856, pp. 579-609.

BRIGGS, B. H. and I. A. Parkin (1963), On the variation of radio star and satellite scintillations with zenith angle, *J. Atmos. Terrest. Phys.*, 25(6), pp. 339-366, doi:10.1016/0021-9169(63)90150-8.

BRINTON, H. C., J. M. Grebowsky, and L. H. Brace (1978), The high-latitude winter F region at 300 km: thermal plasma observations from AE-C, *J. Geophys. Res.*, 83, doi:10.1029/0JGREA000083000A10004767000001.

BRITTNACHER, M., J. Spann, G. Parks, and G. Germany (1997), Auroral observations by the Polar Ultraviolet Imager (UVI), *Adv. Space Res.*, 20(4/5), pp. 1037-1042, doi:10.1016/S0273-1177(97)00558-9.

BUCHAU, J., J. G. Gassmann, C. P. Pike, R. A. Wagner, and J. A. Whalen (1972), Precipitation patterns in the Arctic ionosphere determined from airborne observations, *Annales de Géophysique*, 28(2), pp. 443-453.

BUCHAU, J., E. J. Weber, D. N. Anderson, H. C. Carlson Jr., J. G. Moore, B. W. Reinisch, and R. C. Livingston (1985), Ionospheric structures in the polar cap: Their origin and relation to 250-MHz scintillation, *Radio Sci.*, 20(3), pp. 325–338, doi:10.1029/RS020i003p00325.

BURNS, C. J. and J. K. Hargreaves (1996), The occurrence and properties of large-scale electron-density structures in the auroral F region, *J. Atmos. Terrest. Phys.,* 58(1-4), January-March 1996, pp. 217-232, doi:10.1016/0021-9169(95)00031-3.

BURSTON R., I. Astin, C. N. Mitchell, L. Alfonsi, T. Pedersen and S. Skone (2009), Correlation between scintillation indices and gradient drift wave amplitudes in the northern polar ionosphere, *J. Geophys. Research*, 114, A07309, doi: 10.1029/2009JA014151.

BUST, G. S., T. W. Garner, and T. L. Gaussiran II (2004), Ionospheric Data Assimilation Three Dimensional (IDA4D): A Global, Multi-Sensor, Electron Density Specification Algorithm, *J. Geophys. Research*, 109, A11312, doi: 10.1029/2003JA010234.

BUST, G. S. and G. Crowley (2007), Tracking of polar cap ionospheric patches using data assimilation, *Journal of Geophysical Research*, 112, A05307, pp. 1-17, doi: 10.1029/2005JA011597.

BUST, G. S., G. Crowley, T. W. Garner, T. L. Gaussiran II, R. W. Meggs, C. N. Mitchell, P. S. J. Spencer, P. Yin, and B. Zapfe (2007), Four-dimensional GPS imaging of space weather storms, *Space Weather*, 5, S02003, doi:10.1029/2006SW000237.

CARLSON, H. C., J. Moen, K. Oksavik, C. P. Nielsen, I. W. McCrea, T. R. Pedersen, and P. Gallop (2006), Direct observations of injection events of sub-auroral plasma into the polar cap, *Geophys. Res. Lett.*, 33, L05103, doi: 10.1029/2005GL025230.

CARLSON, H. C. (2012), Sharpening our thinking about polar cap ionospheric patch morphology, research, and mitigation techniques, *Radio Sci.*, 47, RS0L21, doi: 10.1029/2011RS004946.

CHAMBERLAIN, J. W. (1961), Spectral Photometry of the Nightglow, in *Physics of the Aurora and Airglow*, vol. 2, Academic Press Inc., New York & London.

CHARTIER, A. T., C. N. Mitchell and D. R. Jackson (2012), A 12 year comparison of MIDAS and IRI 2007 ionospheric Total Electron Content, *Advances in Space Research*, vol. 49, issue 9, pp. 1348-1355, doi: 10.1016/j.asr.2012.02.014.

CHARTIER, A. T. et al. (2013), Ionospheric imaging in Africa, *Radio Sci.*, 49, doi:10.1002/2013RS005238.

COGGER, L. L., J. S. Murphree, and C. D. Anger (1988), High space and time resolution ultraviolet auroral images from the Viking spacecraft, *Phys. Scr.*, 37(3), pp. 432-436, doi:10.1088/0031-8949/37/3/025.

COKER, C., R. Hunsucker, and G. Lott (1995), Detection of auroral activity using GPS satellites, *Geophys. Res. Lett.*, 22(23), pp. 3259-3262, doi:10.1029/95GL03091.

DAHLGREN, H., A. Aikio, K. Kaila, N. Ivchenko, B. S. Lanchester, D. K. Whiter, and G. T. Marklund (2010), Simultaneous observations of small multi-scale structures in an auroral arc, *J. Atmos. Sol-Terr. Phy.*, 72 (2010), issue 7-8, pp. 663-637, doi: 10.1016/j.jastp.2010.01.014.

DAVIS, T. N. (1978), Observed characteristics of auroral forms, *Space Science Reviews*, 22 (1), pp. 77-113, doi: 10.1016/j.asr.2003.05.037.

DAVIES, K. (1996), 'Characteristics of waves and plasmas,' in *Ionospheric Radio*, pp.15, Peter Peregrinus Ltd., London, United Kingdom, ISBN:0-86341-186-X.

DAVIES, K. (1996), 'Magnetoionic theory,' in *Ionospheric Radio*, pp. 73, Peter Peregrinus Ltd., London, United Kingdom, ISBN:0-86341-186-X.

DEAR, R. M., and C. N. MITCHELL (2006), GPS interfrequency biases and total electron content errors in ionospheric imaging over Europe, *Radio Sci.*, 41, RS6007, doi:10.1029/2005RS003269.

DECKER, D. T., C. E. Valladares, R. Sheehan, S. Basu, D. N. Anderson, and R. A. Heelis (1994), Modeling daytime *F* layer patches over Sondrestrom, *Radio Sci.*, 29(1), pp. 249–268, doi:10.1029/93RS02866.

DE FRANCESCHI, G., L. Alfonsi, V. Romano, M. Aquino, A. Dodson, C. N. Mitchell, P. Spencer, and A. W. Wernik (2008), Dynamics of high-latitude patches and associated small-scale irregularities during the October and November 2003 storms, *J. Atmos. Sol-Terr. Phy.*, 70(6), pp. 879-888, http://dx.doi.org/10.1016/j.jastp.2007.05.018.

DE REZENDE, L. F. C., E. R. de Paula, I. J. Kantor and P. M. Kintner (2007), Mapping and survey of plasma bubbles over Brazilian territory, *Journal of Navigation*, 60, pp. 69-81, doi:10.1017/S0373463307004006.

DESHPANDE, K. B., C. R. Clauer, G. S. Bust, C. N. Mitchell, and J. Kinrade (2011), Investigating polar ionospheric irregularities using GPS scintillation model and observations, presented at the *Fall AGU Meeting*, San Francisco, December 2011.

DONOVAN, E., Mende, S., Jackel, B., Frey, H., Syrjäsuo, M., Voronkov, I., Trondsen, T., Peticolas, L., Angelopoulos, V., Harris, S., Greffen. M., and M. Connors (2006), The THEMIS all-sky imaging array – system design and initial results from the prototype imager, *J. Atmos. Sol-Terr. Phy.*, 68 (2006), pp. 1472-1487, doi: 10.1016/j.asr.2003.05.037.

DUNGEY, J. W. (1961), Interplanetary magnetic field and the auroral zones, *Phys. Rev. Lett.*, 6, 47, doi: 10.1103/PhysRevLett.6.47.

EBIHARA, Y., (2007), *Aurora over South Pole Station* [online]. Japan: Kyoto University. Available from www.southpole-aurora.org/ [last accessed 2012-09-25].

EBIHARA, Y., Y. –M. Tanaka, S. Takasaki, A. T. Weatherwax, and M. Taguchi (2007), Quasi-stationary auroral patches observed at the South Pole station, *J. Geophys. Res*, 112, A01201, doi: 1029/2006JA012087.

EJIRI, M., T. Aso, M. Okada, M. Tsutsumi, M. Taguchi, N. Sato, and S. Okano (1999), Japanese research project on Arctic and Antarctic observations of the middle atmosphere, *Adv. Space Res.*, 24 (12), pp. 1689, doi: 10.1016/S0273-1177(99)00335-X.

FEJER, B. G. and M. C. Kelley (1980), Ionospheric Irregularities, *Reviews of Geophysics*, 18 (2), pp. 401-454, doi: 10.1029/RG018i002p00401.

FELDMAN, U., E. Landi, and N. A. Schwadron (2005), On the sources of fast and slow solar wind, *J. Geophys. Res.*, 110, A07109, doi:10.1029/2004JA010918.

FELDSTEIN, Ya. I., V. G. Vorobjev, and V. L. Zverev (2010), Planetary Features of Aurorae: Results of the IGY (a Review), *Geomagnetism and Aeronomy*, 20(4), pp. 413-435, doi:10.1134/S0016793210040018.

FOSTER, J. C. (1993), Storm time plasma transport at middle and high latitudes, *J. Geophys. Res.*, 98(A2), pp. 1675–1689, doi:10.1029/92JA02032.

FRANK, L. A., J. D. Craven, J. L. Burch, and J. D. Cunningham (1982), Polar views of the Earth's aurora with Dynamic Explorer, *Geophys. Res. Lett.*, 9(9), pp. 1001-1004, doi:10.1029/GL009i009p01001.

FREMOUW, E. J., J. A. Secan, and C. Zhou (1997), Tailoring of EOFs for ionospheric tomography and the weighted, partitioned, least-squares algorithm, *Acta Geod. Geoph. Hung.*, 32(3-4), pp. 365-377,1997.

FREMOUW, E. J. and J. M. Lansinger (1981), Dominant configurations of scintillation-producing irregularities in the auroral zone, *J. Geophys. Res.*, 86(A12), pp. 10087–10093, doi:10.1029/JA086iA12p10087.

FREMOUW, E. J. and J. A. Secan (1984), Modeling and scientific application of scintillation results, *Radio Sci.*, 19(3), pp. 687-694, doi:10.1029/RS019i003p00687.

FREY, H. U., S. Frey, B. S. Lanchester, and M. Kosch (1998), Optical tomography of the aurora and EISCAT, *Ann. Geophys.*, 16, pp. 1332-1342, doi: 10.1007/s00585-998-1332-y.

FREY, H. U., S. B. Mende, T. J. Immel, J. –C. Gérard, B. Hubert, S. Habraken, J. Spann, G. R. Gladstone, D. V. Bisikalo, and V. I. Shematovich (2003), Summary of quantitative interpretation of IMAGE far ultraviolet auroral data, *Space Science Reviews*, 10-2003, 109(1-4), pp. 225-283, doi:10.1023/B:SPAC.0000007521.39348.a5.

GALPERIN, Y. I. (2001), Multiple scales in auroral plasmas, *J. Atmos. Sol-Terr. Phy.*, 64 (2), pp. 211-229, doi: 10.1016/j.asr.2003.05.037.

GARNER, T. W., T. L. Killeen, A. G. Burns, J. D. Winningham, and W. R. Coley (1996), Examination of the oxygen red line signature of a polar cap ionization patch as seen from the Dynamics Explorer 2 satellite, *Radio Sci.*, 31(3), 607-618, doi: 10.1029/96RS00617.

GARNER, T. W. et al. [2008], Total electron content measurements in ionospheric physics, *Advances in Space Research*, 42(4), pp. 720-726, doi:10.1016/j.asr.2008.02.025.

GARNER, T. W., R. B. Harris, J. A. York, C. S. Herbster, C. F. Minter III, and D. L. Hampton (2011), An auroral scintillation observation using precise, collocated GPS receivers, *Radio Sci.*, 46, RS1018, doi: 10.1029/2010RS004412.

GWAL, A. K., S. Dubey, and R. Wahi, (2004), A study of L-band scintillations at equatorial latitudes, *Advances in Space Research*, 34(9), pp. 2092-2095, http://dx.doi.org/10.1016/j.asr.2004.08.005.

HAALAND, S.E., G. Paschmann, M. Förster, J.M. Quinn, R.B. Torbert, C.E. McIlwain, H. Vaith, P.A. Puhl-Quinn, and C.A. Kletzing (2007), High-latitude plasma convection from Cluster EDI measurements: method and IMF-dependence, *Ann. Geophys.*, 25, pp. 239-253.

HAERENDEL, G., B.U. Olipitz, S. Buchert, O.H. Bauer, E. Rieger, C. La Hoz (1996), Optical and radar observations of auroral arcs with emphasis on small-scale structures, *Journal of Atmospheric and Terrestrial Physics*, 58(1-4), pp. 71-83, ISSN 0021-9169.

HALDOUPIS, C., K. Schlegel, and G. Hussey (2000), Auroral E-region electron density gradients measured with EISCAT, *Ann. Geophysicae*, 18(9), pp. 1172-1181, doi: 10.1007/s00585-000-1172-x.

HEGARTY, C. J. (1997), Analytical derivation of maximum tolerable in-band interference levels for aviation applications of GNSS, *Navigation*, *Journal of The Institute of Navigation*, 44(1), pp. 25-34.

HEWISH, A. (1951), The diffraction of radio waves passing through a phase-changing ionosphere, *Proc. R. Soc. London*, *Ser. A*, 209, pp. 81-96.

HILL, T. W. (2004), Auroral structures at Jupiter and Earth, *Advances in Space Research*, 33 (11), 2021-2029, doi: 10.1016/j.asr.2003.05.037.

HOSOKAWA, K., J. I. Moen, K. Shiokawa, and Y. Otsuka (2011), Motion of polar cap arcs, *J. Geophys. Res.*, 116, A01305, doi: 10.1029/2010JA015906.

HUFFMAN, R. E. (1992), 'Global Auroral Imaging', in *Atmospheric Ultraviolet Remote Sensing*, pp. 253, Academic Press Limited, London, ISBN 0-12-360390-0.

HUMPHREYS, T. E., M. L. Psiaki, P. M. Kintner Jr., and B. M. Ledvina (2005), GPS carrier tracking loop performance in the presence of ionospheric scintillations, paper presented at *ION GNSS 2005*, Inst. Of Navig., Long Beach, California.

HUNSUCKER, R.D., C. Coker, J. Cook, and G. Lott (1995), An investigation of the feasibility of utilizing GPS/TEC "signatures" for near-real time forecasting of auroral-E propagation at high-HF and low-VHF frequencies, *Antennas and Propagation, IEEE Transactions on* , 43(11), pp.1313-1318, doi: 10.1109/8.475104.

HUNSUCKER, R. D. and J. K. Hargreaves (2003), The high-latitude F-region and the trough, in *The High-Latitude Ionosphere and its Effects on Radio Propagation*, pp. 227-281, Cambridge University Press, Cambridge, United Kingdom.

IDENDEN, D. W., R. J. Moffett, and S. Quegan (1997), Ionospheric structure produced during a rapid polar cap expansion, *J. Geophys. Res.*, 102, doi:10.1029/97JA01148.

IMBER, S. M., S. E. Milan, and M. Lester (2012), The Heppner-Maynard Boundary measured by SuperDARN as a proxy for the latitude of the auroral oval, *J. Geophys. Res.*, doi:10.1029/2012JA018222, in press.

JONES, D. G., I. K. Walker, and L. Kersley (1997), Structure of the poleward wall of the trough and the inclination of the geomagnetic field above the EISCAT radar, *Annales Geophysicae*, 15(6), pp. 740-746, doi:10.1007/s00585-997-0740-8.

KAMIDE, Y. and A. Chian (2007), 'Chapter 10: Space Plasmas' in *Handbook of the Solar-Terrestrial Environment*, pp. 261, Springer, ISBN: 3540463143.

KAPLAN, E. D. and C. J. Hegarty (2006), *Understanding GPS: principles and applications – 2nd ed.*, Artech House Inc., Norwood, MA, USA, ISBN: 1-58053-894-0.

KELLEY, M. C. (2009), *The Earth's Ionosphere: Plasma Physics and Electrodynamics*, 2nd Ed., Academic Press, Elsevier, ISBN:978-0-12-088425-4.

KELLEY, M. C. (2009), 'High-Latitude Electrodynamics' in *The Earth's Ionosphere: Plasma Physics and Electrodynamics 2nd Ed.*, pp. 392-395, Elsevier, Academic Press, ISBN: 978-0-12-088425-4.

KERSLEY, L., S. E. Pryse, I. K. Walker, J. A. T. Heaton, C. N. Mitchell, M. J. Williams, and C. A. Wilson (1997), Imaging of electron density troughs by tomographic techniques, *Radio Science*, 32(4), pp. 1607-1621, doi:10.1029/97RS00310.

KHOROSHEVA, O. V. (1961), Spatial and temporal distribution of the aurora and their relation with high latitude geomagnetic disturbances, *Geomag. and Aeronomie.*, 1(5), pp. 696-701.

KING, J. H., and N. E. Papitashvili (2005), Solar wind spatial scales in and comparisons of hourly Wind and ACE plasma and magnetic field data, *J. Geophys. Res.*, 110, A02104, doi:10.1029/2004JA010649.

KINRADE, J., C. N. Mitchell, P. Yin, N. Smith, G. S. Bust, M. J. Jarvis, D. J. Maxfield, M. C. Rose, and A. T. Weatherwax (2012), Ionospheric scintillation over Antarctica during the storm of 5-6 April 2010, *J. Geophys. Res.*, 117, A05304, doi: 10.1029/2011JA017073.

KINRADE, J., C. N. Mitchell, N. D. Smith, Y. Ebihara, A. T. Weatherwax, and G. S. Bust (2013), GPS phase scintillation associated with optical auroral emissions: first statistical results from the geographic South Pole, *J. Geophys. Res. Space Physics,* 118, 2490–2502, doi: 0.1002/jgra.50214.

KINTNER, P. M., H. Kil, C. Deehr, and P. Schuck, Simultaneous total electron content and all-sky camera measurements of an auroral arc, *J. Geophys. Res.*, 107(A7), doi:10.1029/2001JA000110, 2002.

KINTNER, P. M., B. M. Ledvina, and E. R. de Paula (2007), GPS and ionospheric scintillations, *Space Weather*, 5, S09003, doi:10.1029/2006SW000260.

KUBOTA, M., H. Fukunishi, and S. Okano (2001), Characteristics of medium- and large-scale TIDs over Japan derived from OI 630-nm nightglow observation, *Earth Planets Space*, 53(7), pp. 741-751.

LAUNDAL, K. M. and N. Østgaard (2009), Asymmetric auroral intensities in the Earth's Northern and Southern hemispheres, *Nature*, vol. 460, issue 7254, pp. 491-493, doi: 10.1038/nature08154.

LEE, C. N., et al. (2010), Spectral observations of FUV auroral arcs and comparison with inverted-V precipitating electrons, *J. Geophys. Res.*, 115, A09223, doi:10.1029/2009JA015071.

LONGDEN, N., G. Chisham, M. P. Freeman, G. A. Abel, and T. Sotirelis (2010), Estimating the location of the open-closed magnetic field line boundary from auroral images, *Ann. Geophys.*, 28, pp. 1659-1678, doi:10.5194/angeo-28-1659-2010.

MACHOL, J. L., J. C. Green, R. J. Redmon, R. A. Viereck, and P. T. Newell (2012), Evaluation of OVATION Prime as a forecast model for visible aurorae, *Space Weather*, 10, S03005, doi:10.1029/2011SW000746.

MEGGS, R. W., C. N. Mitchell, and V. S. C. Howells (2005), Simultaneous observations of the main trough using GPS imaging and the EISCAT radar, *Ann. Geophys.*, 23, pp. 753-757, doi:10.5194/angeo-23-753-2005.

MENDE, S. B., H. U. Frey, T. J. Immel, J. –C. Gerard, B. Hubert, and S. A. Fuselier (2003), Global Imaging of Proton and Electron Aurorae in the far Ultraviolet, *Space Science Reviews*, 109(1-4), pp. 211-254, doi:10.1023/B:SPAC.0000007520.23689.08.

MENDE, S. B., V. Angelopoulos, H. U. Frey, S. Harris, E. Donovan, B. Jackel, M. Syrjaesuo, C. T. Russell, and I. Mann (2007), Determination of substorm onset timing and location using the THEMIS ground based observatories, *Geophys. Res. Lett.*, 34, L17108, doi:10.1029/2007GL030850.

MITCHELL, C. N., D. G. Jones, L. Kersley, S. E. Pryse, and I. K. Walker (1995), Imaging of field-aligned structures in the auroral ionosphere, *Ann. Geophys.*, 13(12), pp. 1311-1319, Copernicus.

MITCHELL, C. N., I. K. Walker, S. E. Pryse, I. Kersley, I. W. McCrea, and T. B. Jones (1998), First complementary observations by ionospheric tomography, the EISCAT Svalbard radar and the CUTLASS HF radar, Ann. Geophysicae 16, pp.1519-1522, doi:10.1007/s00585-998-1519-2

MITCHELL, C. N. and P. S. J. Spencer (2003), A three-dimensional time-dependent algorithm for ionosphere imaging using GPS, *Ann. Geophys.*, 46(4).

MITCHELL, C. N., L. Alfonsi, G De Franceschi, M. Lester, V. Romano and A. W. Wernik (2005), GPS TEC and scintillation measurements from the polar ionosphere during the October 2003 storm, *Geophys. Res. Lett.*, 32, L12S03, doi: 10.1029/2004GL021644.

MOEN, J., S. T. Berry, L. Kersley and B. Lybekk (1998), Probing discrete auroral arcs by ionospheric tomography, *Ann. Geophys.*, 16, 574-582, doi: 10.1007/s00585-998-0574-z.

MOEN, J., H. C. Carlson, K. Oksavik, C. P. Nielsen, S. E. Pryse, H. R. Middleton, I. W. McCrea, and P. Gallop (2006), EISCAT observations of plasma patches at sub-auroral cusp latitudes, *Ann. Geophys.*, 24, pp. 2363-2374, doi:10.5194/angeo-24-2363-2006, 2006.

MÖSTL, C., M. Temmer, T. Rollett, C. J. Farrugia, Y. Liu, A. M. Veronig, M. Leitner, A. B. Galvin, and H. K. Biernat (2010), STEREO and Wind observations of a fast ICME flank triggering a prolonged geomagnetic storm on 5–7 April 2010, *Geophys. Res. Lett.*, 37, L24103, doi: 10.1029/2010GL045175.

NEWELL, P. T., T. Sotirelis, J. M. Ruohoniemi, J. F. Carbary, K. Liou, J. P. Skura, C.-I. Meng, C. Deehr, D. Wilkinson, and F. J. Rich (2002), OVATION: Oval variation, assessment, tracking, intensity, and online nowcasting, *Ann. Geophys.*, 20, pp. 1039-1047, doi:10.5194/angeo-20-1039-2002.

NGWIRA, C. M., L. McKinnell, P. J. Cilliers (2010), GPS phase scintillation observed over a high-latitude Antarctic station during solar minimum, *J. Atmos. Sol-Terr. Phy.*, 72, pp. 718-725, doi: 10.1016/j.jastp.2010.03.014.

OBARA, T. and K. Fukui (1997), Polar auroral arc studies particularly using Akebono satellite and Qaanaaq (Greenland) all-sky imager data, *J. Atmos. Sol-Terr. Phy.*, 59 (96), pp. 1361-1372, doi: 10.1016/S1364-6826(96)00187-3.

ØSTGAARD, N., S. B. Mende, H. U. Frey, J. B. Sigwarth, A. Åsnes, and J. M. Weygand (2007), Auroral conjugacy studies based on global imaging, *Journal of Atmospheric and Solar-Terrestrial Physics*, 69, pp. 249-255, doi:10.1016/j.jastp.2006.05.026.

POKHOTELOV, D., P. T. Jayachandran, C. N. Mitchell and M. H. Denton (2010), High-latitude ionospheric response to co-rotating interaction region- and coronal mass ejection-driven geomagnetic storms revealed by GPS tomography and ionosondes, *Proceedings of the Royal Society of London Series A - Mathematical Physical and Engineering Sciences*, 466 (2123), pp. 3391-3408.

PRIKRYL, P., P. T. Jayachandran, S. C. Mushini, D. Pokhotelov, J. W. MacDougall, E. Donovan, E. Spanswick, and J. –P. St. –Maurice (2010), GPS TEC, scintillation and cycle slips observed at high latitudes during solar minimum, *Ann. Geophys.*, 28, 1307-1316, doi: 10.5194/angeo-28-1307-2010.

PRIKRYL, P., L. Spogli, P. T. Jayachandran, J. Kinrade, C. N. Mitchell, B. Ning, G. Li, P. J. Cilliers, M. Terkildsen, D. W. Danskin, E. Spanswick, E. Donovan, A. T. Weatherwax, W. A. Bristow, L. Alfonsi, G. De Franceschi, V. Romano, C. M. Ngwira, and B. D. L. Opperman (2011), Inter-hemispheric comparison of GPS phase scintillation at high latitudes during the magnetic-cloud-induced geomagnetic storm of 5–7 April 2010, *Ann. Geophys.*, 29, 2287-2304, doi: 10.5194/angeo-29-2287-2011.

PRYSE, S. E., L. Kersley, and I. K. Walker (1996), Blobs and irregularities in the auroral ionosphere, *J. Atmos. Terrest. Phys.*, 58(1-4), pp. 205-215, doi:10.1016/0021-9169(95)00030-5.

REES, M. H. (1989), *Physics and chemistry of the upper atmosphere*, Cambridge University Press, ISBN: 0-521-32305-3.

REES, D., M. Conde, Å. Steen, and U. Brändström (2000), The first daytime ground-based optical image of the aurora, *Geophysical Research Letters*, 27 (3), pp. 313-316, doi: 1029/1999GL003696.

RINO, C. (1976), Ionospheric Scintillation Theory – A Mini-Review, *IEE Transactions on Antennas and Propagation*, 24(6), pp. 912-915, doi:10.1109/TAP.1976.1141439.

RINO, C. (1979), A power law phase screen model for ionospheric scintillation: 1. Weak scatter, *Radio Sci.*, 14(6), pp. 1135-1145, doi: 10.1111/j.1468-1331.2011.03436.x.

ROBINSON, R. M., and R. R. Vondrak (1985), Characteristics and sources of ionization in the continuous aurora, *Radio Sci.*, 20(3), pp. 447–455, doi:10.1029/RS020i003p00447.

RODGER, A. S., R. J. Moffett, and S. Quegan (1992), The role of ion drift in the formation of ionization troughs in the mid- and high-latitude ionosphere – a review, *Journal of Atmospheric and Solar-Terrestrial Physics*, 54(1), pp. 1-30, doi:10.1016/0021-9169(92)90082-V.

SAMADANI, R., D. A. Mihovilovic, C. R. Clauer, G. Wiederhold, J. D. Craven, and L. A. Frank (1990), A computer vision system for automatically finding the auroral oval from satellite images, *Proc. SPIE 1244*, *Image Processing Algorithms and Techniques*, 68 (June 1, 1990), doi:10.1117/12/19496.

SANDAHL, I., U. Brandstrom and T. Sergienko (2011), Fine structure of aurora, *International Journal of Remote Sensing*, vol. 32, issue 11, pp. 2947-2972, doi: 10.1080/01431161.2010.541507.

SANDHOLT, P. E., C. J. Farrugia, J. Moen, Ø. Noraberg, B. Lybekk, T. Sten, and T. Hansen (1998), A classification of dayside auroral forms and activities as a function of interplanetary magnetic field orientation, *J. Geophys. Res.*, 103(A10), pp. 23325–23345, doi:10.1029/98JA02156.

SANDHOLT, P. E., H. C. Carlson and A. Egeland (2002), Optical Aurora, in *Dayside and Polar Cap Aurora*, pp. 33-49, Astrophysics and Space Science Library, vol. 270, Kluwer Academic Publishers, Dordrecht, The Netherlands. ISBN: 1-4020-0447-8.

SANDHOLT, P. E., H. C. Carlson, and A. Egeland (2002), 'Magnetospheric Boundary Layers' in *Dayside and Polar Cap Aurora*, pp. 11-13, Kluwer Academic Publishers, Dordrecht, The Netherlands, ISBN: 1-4020-0447-8.

SANDHOLT, P. E., C. J. Farrugia, and W. F. Denig (2004), Dayside aurora and the role of IMF $|B_y|/|B_z|$: detailed morphology and response to magnetopause reconnection, *Ann. Geophys.*, 22, pp. 613-628.

SEAMAN, C. J. and S. D. Miller (2013), VIIRS Captures Aurora Motions, *Bulletin of the American Meteorological Society 2013*, doi:10.1175/BAMS-D-12-00221.1.

SEARS, R. D., and R. R. Vondrak (1981), Optical emissions and ionization profiles during an intense pulsating aurora, *J. Geophys. Res.*, 86(A8), pp. 6853–6858, doi:10.1029/JA086iA08p06853.

SECAN, J. A., R. M. Bussey, E. J. Fremouw, and S. Basu (1997), High-latitude upgrade to the Wideband ionospheric scintillation model, *Radio Sci.*, 32(4), pp. 1567-1574, doi: 10.1029/97RS00453.

SELLEK, R., G. J. Bailey, R. J. Moffett, R. A. Heelis, and P. C. Anderson (1991), Effects of large zonal plasma drifts on the sub-auroral ionosphere, *Journal of Atmospheric and Terrestrial Physics*, 53(6-7), pp. 557-565.

SEMETER, J., T. Butler, C. Heinselman, and M. Nicolls (2009), Volumetric imaging of the auroral ionosphere: Initial results from PFISR, *Journal of Atmospheric and Solar-Terrestrial Physics*, 71, pp. 738-743, doi:10.1016/j.jastp.2008.08.014.

SKONE, S. H., and M. E. Cannon (1999), Ionospheric effects on differential GPS applications during auroral substorm activity, ISPRS Journal of Photogrammetry and Remote Sensing, 54(4), pp. 279-288, doi:10.1016/S0924-2716(99)00017-9.

SKONE, S. H. (2001), The impact of magnetic storms on GPS receiver performance, *J. Geodesy*, 75(9-10), pp. 457-468, doi:10.1007/s001900100198.

SMITH, A. M., C. N. Mitchell, R. J. Watson, R. W. Meggs, P. M. Kintner, K. Kauristie, and F. Honary (2008), GPS scintillation in the high arctic associated with an auroral arc, *Space Weather*, 6, S03D01, doi: 10.1029/2007SW000349.

SOJKA, J. J. et al. (1993), Modelling polar cap F region patches using time varying convection, *Geophys. Res. Lett.*, 20, pp. 1783.

SOTIRELIS, T., P. T. Newell, and C. –I. Meng (1998), Shape of the open-closed boundary of the polar cap as determined from observations of precipitating particles by up to four DMSP satellites, *J. Geophys. Res.*, 103(A1), pp. 399-406, doi:10.1029/97JA02437.

SOTIRELIS, T. and P. T. Newell (2000), Boundary-orientated electron precipitation model, *J. Geophys. Res.*, 105(A8), pp. 18655-18673, doi:10.1029/1999JA000269.

SPENCER, P. S. J. and C. N. Mitchell (2001). Multi-instrument inversion technique for ionospheric imaging, *International Beacon Satellite Symposium*, 3-6 June 2001, Boston, USA, Proceedings.

SPENCER, P. S. J. and C. N. Mitchell (2007), Imaging of fast moving electron-density structures in the polar cap, *Ann. Geophys*, 50 (3), pp. 427-434.

SPOGLI, L., L. Alfonsi, G. De Franceschi, V. Romano, M. Aquino, and A. Dodson (2009), Climatology of GPS ionospheric scintillations over high and mid-latitude European regions, *Ann. Geophys.*, 27, 3429-3437.

STOKER, P. H., M. J. Mathews, and M. W. J. Scourfield (1996), Coordinated measurements of auroral light intensities and riometric radio-wave absorption, *Geophys. Res. Lett.*, 23(6), pp. 641-644, doi: 10.1029/96GL00377.

STRANGEWAYS, H. J. (2009), Determining scintillation effects on GPS receivers, *Radio Sci.*, 44, RS0A36, doi:10.1029/2008RS004076.

TANAKA, Y. -M., Y. Ebihara, S. Saita, A. Yoshikawa, Y. Obana, and A. T. Weatherwax (2012), Poleward moving auroral arcs observed at the South Pole Station and the interpretation by field line resonances, *J. Geophys. Res.*, doi:10.1029/2012JA017899, in press.

TSAI, H. -F., J. -Y. Liu, C. -H. Lin, and M. -L. Hsu (2010), FORMOSAT-3/COSMIC observations of the ionospheric auroral oval development, *GPS Solutions*, 14, pp. 91-97, doi:10.1007/s10291-009-0137-0.

TSUNODA, R. T. (1988), High-latitude F-region irregularities: a review and synthesis, *Reviews of Geophysics*, 26(4), pp. 719-760.

UMEKI, R., C. H. Liu, and K. C. Yeh (1977), Multifrequency spectra of ionospheric amplitude scintillations, *J. Geophys. Res.*, 82(19), pp. 2752-2760.

VALLADARES, C., S. Basu, J. Buchau, and E. Friis-Christensen (1994), Experimental evidence for the formation and entry of patches into the polar cap, *Radio Sci.*, 29(1), pp. 167-194, doi:10.1029/93RS01579.

VAN DIERENDONCK, A. J. (1993), Ionospheric scintillation monitoring using commercial single frequency C/A code receivers, *Proceedings of ION GPS-93*, 1333, The Institute of Navigation, Arlington, VA, USA.

VAN DIERENDONCK, A. J. (1999), Eye on the Ionosphere: Measuring ionospheric scintillation events from GPS signals, *GPS Solutions*, 2(4), pp. 60-63.

YEH, K. C. and C. -H. Liu (1982), Radio wave scintillations in the ionosphere, *Proceedings of the* IEEE, 70(4), pp. 324-360, doi: 10.1109/PROC.1982.12313.

YIN, P., C. N. Mitchell, P. Spencer, and T. Pedersen (2008), A multi-diagnostic approach to understanding high-latitude plasma transport during the Halloween 2003 storm, *Ann. Geophysicae* 26, pp. 2739-2747, doi: 10.5194/angeo-26-2739-2008.

YIN, P., C. N. Mitchell, L. Alfonsi, M. Pinnock, P. S. J. Spencer, G. De Franceschi, V. Romano, P. Newell, P. Sarti, M. Negusini, A. Capra (2009), Imaging of the Antarctic ionosphere: Experimental results, *J. Atmos. Sol-Terr. Phy.*, 71 (17-18), pp. 1757-1765, doi:10.1016/j.jastp.2009.09.014.

ZHANG, Y., L. J. Paxton, D. Bilitza, and R. Doe (2010), Near real-time assimilation in IRI of auroral peak E-region density and equatorward boundary, *Adv. Space Res.*, 46(8), pp. 1055-1063, doi:10.1016/j.asr.2010.06.029.

10 Appendix

10.1 December 2010-January 2011 Expedition

A significant Antarctic fieldwork stage was undertaken with the British Antarctic Survey during the winter period 2010/11. The primary purpose of the fieldwork was to maintain and service the University of Bath's network of remote GPS scintillation receivers, which has been operating since January 2010. Two remote array sites, 'Eagle' and 'Owl' are situated at 81°S and 89°S respectively, with a further two station-based receivers at the Amundsen-Scott South Pole Research Station (90°S) and at Rothera Research Station (66°S).

Figure 10.1 – A remote Antarctic GPS scintillation monitoring station at Site Eagle (81°S). The power support system can be seen in the background alongside an array of wind turbine generators and an automated weather station mast. The author can be seen digging out the GPS receiver box, which is buried to protect the electronics from harsh surface wind temperature fluctuations. The GPS antenna is out of shot in the foreground, a sufficient distance away from the wind turbine blades – a potential source of multipath interference. This PhD research has relied heavily on remote measurements and sustained operation from the Antarctic receiver network.

10.2 Materials supporting Chapter 6

10.2.1 Additional correlation statistics

Table 10.1 – All available data - Collective-satellite 557.7 nm correlation coefficients[a]

Date	Time Span (UT)	No. Data Points	R_{558}	R_{LO}	R_{UP}	Max. σ_φ	Max. I_{mean}
2010-06-16	0041-0359	3497	0.5525	0.5290	0.5751	0.4166	23482
2010-08-03	0000-0200	2335	0.5487	0.5197	0.5764	0.4071	15805
2011-07-31	0002-2359	25582	0.5323	0.5235	0.5411	0.5628	48416
2010-05-21	0001-0000	25299	0.4933	0.4839	0.5026	0.5248	36883
2010-08-09	0037-0000	25670	0.4358	0.4259	0.4457	0.2902	46384
2010-05-20	0013-0000	25911	0.2986	0.2874	0.3096	0.4098	31246
2011-05-26	0002-2359	25777	0.2912	0.2800	0.3023	0.4814	44720
2011-05-02	0003-0659	5991	0.2474	0.2235	0.2711	0.5988	32484
2011-05-03	0002-2359	25884	0.2382	0.2267	0.2497	0.6141	32765
2011-05-28	0003-2359	13376	0.2332	0.2171	0.2491	0.4459	10138
2011-04-29	1803-1959	1790	0.2208	0.1762	0.2644	0.2773	6651
2011-07-25	0002-2359	25545	0.1763	0.1644	0.1882	0.3584	8394
2011-04-28	1602-2359	4826	0.1536	0.1259	0.1810	0.3110	24021
2011-04-30	0003-2359	20568	0.1351	0.1217	0.1485	0.5201	46117
2010-08-04	0000-1601	17064	0.0686	0.0537	0.0836	0.6109	16579
2011-05-04	0002-2359	26280	0.0058	-0.0063	0.0179	0.5698	18657
2011-05-01	0003-2359	21747	-0.0149	-0.0282	-0.0017	0.6318	23428

[a] Collective-satellite correlation coefficients resulting from the complete ASI datasets for the case study days (all available times), using mean intensity 557.7 nm emission images. R_{LO} and R_{UP} are the lower and upper 95% confidence limits of the correlation coefficient respectively. Peak values of σ_φ indices and emission intensity, I_{mean}, from all observed satellites in the time interval are provided for reference.

Table 10.2 – All available data - Collective-satellite 630.0 nm correlation coefficients[a]

Date	Time Span (UT)	No. Data Points	R_{630}	R_{LO}	R_{UP}	Max. σ_φ	Max. I_{mean}
2010-06-16	0041-0440	4250	0.5947	0.5749	0.6138	0.4543	3002.3
2010-08-09	0037-0000	25673	0.4936	0.4843	0.5028	0.3310	3940.5
2010-05-20	0013-0000	25913	0.4582	0.4485	0.4678	0.3480	5713.1
2011-04-30	0002-2359	41330	0.4336	0.4258	0.4414	0.5473	5646.1
2011-05-03	0002-2359	25883	0.4114	0.4012	0.4215	0.4828	3167.5
2011-05-28	0002-0000	13360	0.3911	0.3766	0.4054	0.4896	4056.6
2010-08-03	0001-0336	4291	0.3873	0.3615	0.4124	0.4071	1737.0
2011-07-25	0002-2359	25357	0.3857	0.3752	0.3962	0.3584	4274.6
2010-08-04	0001-0000	25479	0.3638	0.3531	0.3744	0.7310	5124.9
2011-05-01	0002-2359	41431	0.3576	0.3492	0.3660	0.6318	3826.1
2011-07-31	0002-2359	25406	0.3446	0.3338	0.3554	0.5628	2830.9
2011-05-02	0002-0659	12012	0.3405	0.3246	0.3562	0.5988	3179.7
2011-04-29	0002-2033	35852	0.3243	0.3150	0.3335	0.4770	3720.5
2010-05-21	0001-0000	25309	0.3167	0.3056	0.3278	0.6034	3005.8
2011-05-04	0002-2359	26267	0.2292	0.2177	0.2406	0.5247	2190.0
2011-04-28	0002-2359	14756	0.2261	0.2107	0.2413	0.3466	3050.2
2011-05-26[b]	0002-2359	25594	-0.0030	-0.0152	0.0093	0.3792	53.6

[a] Collective-satellite correlation coefficients resulting from the complete ASI datasets for the case study days (all available times), using mean intensity 630.0 nm emission images. R_{LO} and R_{UP} are the lower and upper 95% confidence limits of the correlation coefficient respectively. Peak values of σ_φ indices and emission intensity, I_{mean}, from all observed satellites in the time interval are provided for reference.

[b] Note that 630.0 nm emission images were at noise level throughout the day of 26 May 2011.

10.2.2 Conditional occurrence probability

Applying threshold values I_{TH} and S_{TH} to optical 557.7 nm emission intensity (I_{558}) measurements and GPS σ_φ indices respectively:

P(S|I) is the conditional probability of a σ_φ event given an I_{558} event, where:

S = an event defined by $\sigma_\varphi \geq S_{TH}$

I = an event defined by $I_{558} \geq I_{TH}$

This was calculated from the entire study dataset by:

P(S|I) = n(S|I)/n(I) , where:

n(S|I) = total number of occurrences of both S *and* I events

n(I) = total number of occurrences of I events

10.3 SSUSI 135 nm UV images – 26 September 2011

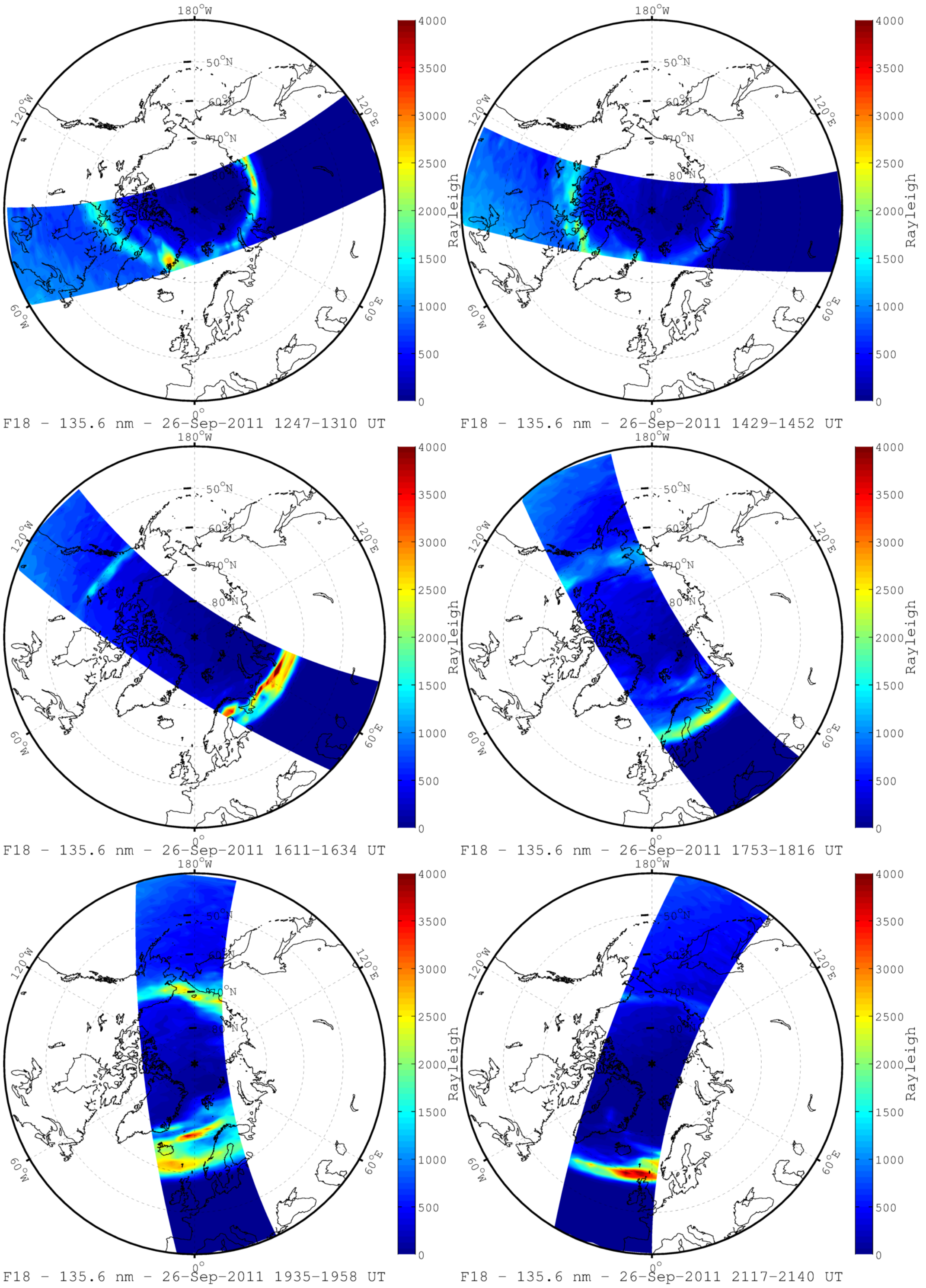

F18 - 135.6 nm - 26-Sep-2011 1247-1310 UT

F18 - 135.6 nm - 26-Sep-2011 1429-1452 UT

F18 - 135.6 nm - 26-Sep-2011 1611-1634 UT

F18 - 135.6 nm - 26-Sep-2011 1753-1816 UT

F18 - 135.6 nm - 26-Sep-2011 1935-1958 UT

F18 - 135.6 nm - 26-Sep-2011 2117-2140 UT

Figure 10.2 – A sequence of composite-scan ultraviolet images from the SSUSI photometer on-board the DMSP satellite F18. The sequence shows the expansion of the auroral oval during the initial stages of a geomagnetic storm on 26 September 2011, followed by intensification and widening of the auroral bands likely related with substorm activity.